Aramco Journal of Technology

SPRING 2021

The *Aramco Journal of Technology* is published quarterly by the Saudi Arabian Oil Company, Dhahran, Saudi Arabia, to provide the company's scientific and engineering communities a forum for the exchange of ideas through the presentation of technical information aimed at advancing knowledge in the hydrocarbon industry.

Editor

William E. Bradshaw
william.bradshaw.1@aramco.com.sa
tel: +966-013-876-0498

The *Aramco Journal of Technology* gratefully acknowledges the assistance, contribution and cooperation of numerous operating organizations throughout the company.

ISSN 1319-2388

Contents

Dynamic Study of Spontaneous Imbibition Test for Fracturing Fluid Uptake Pathways Using Microscale Radiographic Imaging

Dr. Feng Liang, Jilin Zhang, Dr. Hui-Hai Liu and Dr. Shawn Zhang

Abstract /

Hydraulic fracturing has been widely used in stimulating unconventional reservoirs, including tight carbonate formations, to improve oil and gas production. The stimulation process requires massive volumes of fracturing fluid to crack the formation; however, only a small percentage of the fluid is recovered during the fluid flow back process. Where the remaining fluids reside in the formation is still not clear. This work strives to use microscale radiographic imaging to study the fluid uptake pathways.

The spontaneous imbibition of fracturing fluid into organic-rich carbonate source rock was experimentally investigated on the microscopic scale. A thin section sample, with a dimension of 22 × 11 × 3.3 mm (length × width × thickness), was sliced using a trim saw and attached onto a glass slide with epoxy. This sample was composed of two distinguished zones, an organic matter-rich zone (OMZ) and a calcite-rich zone (Cal-Z). Iodide containing aqueous-based fluid was used as the source fluid to treat the thin section rock sample from one end. The spontaneous imbibition test was conducted for 100 minutes with one radiographic image taken per minute to capture the dynamic fluid front.

The iodide containing aqueous-based fluid was used in this study to enhance the contrast in microscale radiographic imaging. Microfractures were observed by radiographic imaging in the thin section sample with 5.48 μm and 2.79 μm resolutions before the fluid treatment, both in the OMZ and the Cal-Z.

Three fluid uptake features have been revealed in this dynamic fluid imbibition study: (1) the fluid moved very fast and reached the other end of the sample in less than 4 minutes in the microfractures within the OMZ; (2) the fluid moved very fast and reached the other end of the sample in less than 4 minutes in microfractures within the Cal-Z; and (3) in a calcite-rich matrix, the waterfront progressed very slowly, to about 120 μm penetration in 100 minutes.

The fast water uptake through microfractures in the OMZ and fracture networks in the Cal-Z correspond to imbibition controlled transport in the strongly water-wet pore space. The slow water uptake through the calcite-rich matrix could be a combination of weakly water-wet imbibition and slow flow process due to large viscous flow resistance (or small permeability) in small-sized pores.

During the slick water fracturing process in unconventional reservoirs, only a small percentage of fracturing fluids is generally recovered. Where the remaining fluids reside in the formation is still an open question in the industry. This study experimentally reveals that the imbibition into the rock matrix is much slower than into microfractures. Therefore, it is very likely that natural and induced microfractures are the major areas where the fluids remain after the flow back.

Introduction

In the Middle East, carbonate fields are dominant with approximately 70% of oil and 90% of gas reserves[1]. Acid fracturing and matrix acidizing are the most common ways for stimulating conventional carbonate reservoirs due to the reactivity with acids[2-5]. Subsequently, acids are not as effective in stimulating carbonate-rich tight gas or shale formations due to the formation's significantly lower permeability (nd to μd range) and their heterogeneous pore structures[6-8].

Hydraulic fracturing is still the most effective stimulation technique to produce natural gas from tight carbonate reservoirs. During hydraulic fracturing, massive amounts of fracturing fluids are pumped to crack open the formation and only a small percentage of the fluids are recovered during the flow back process[9-11]. Questions, such as where the remaining fluid is located after fluid flow back, and what the remaining fluid does to the formation, remain unanswered.

Despite extensive previous studies of the interaction between carbonate rocks and fracturing fluid[12, 13], there have been very few microscopic studies documented, including microfractures, and mineralogic changes of the fluid and rock interaction. Microfractures refer to fractures which have lengths of millimeters or less and apertures that are less than 0.1 mm[14, 15].

Gale et al. (2014)[15] noted that sealed microfractures occur in shales but are uncommon, which might be because the size of the microfractures possibly fell below the resolution of the imaging tools used in past studies, or they were not captured in the small sampling of rocks analyzed. The authors have concluded that the role of microfractures in shale production is poorly understood and should merit further study. Also, during the hydraulic fracturing process, numerous amounts of fractures and microfractures are induced.

Given the complexity of the tight organic-rich carbonate source rocks and their high heterogeneity, microscopic studies on the textual, and the effects of the imbibed fluid on the mechanical, morphological and flow properties of tight organic-rich carbonate rocks are very important.

Most recently, Liang et al. (2018)[16] and (2019)[17] reported that a considerable amount of dissolution and precipitation was observed in imbibition tests of rock samples from an organic-rich, tight carbonate formation in a neutral pH fracturing fluid in laboratory experiments. The dissolution of the sulfate and carbonate minerals, as well as reopening of the filled microfractures, results in a potential increase of the absolute permeability of the reservoir rocks, while mineral precipitation tends to reduce the absolute permeability of the reservoir rocks. The permeability, after 2 wt% of potassium chloride imbibition, was about four times higher than the same rock sample studied prior to the imbibition test under the documented testing conditions.

This observed stress sensitivity is consistent with the fact that the permeability of open/barren microfractures, rather than sealed/cemented microfractures[18], are relatively stress sensitive[18-22]. In these tests, various components were exposed to the fracturing fluid with equal chance of exposure, therefore, it is important to ask whether different laminae are equally exposed to the fracturing fluids in the reservoir conditions and whether the fracturing fluid travels with any preference to certain laminae of the rock formation in situ.

Also, what is the flow path preference when microfractures are presented? If there is a preferred pathway, how much difference will be expected among different flow pathways? It is critical to undertand the dual continuum flow phenomena in tight carbonate rocks to design more accurate simulations for the designs of hydraulic fracturing.

In this study, we designed an experiment for dynamically capturing the fluid pathway through a highly laminated tight organic-rich carbonate thin section sample using X-ray radiographic images. The selected sample was composed of two distinguished zones: (1) an organic matter-rich zone (OMZ), and (2) a calcite-rich zone (Cal-Z). Potassium iodide (KI) was added to the treatment fluid to enhance the contrast of the images.

Microfractures were present in both zones. The spontansous imbibition test was conducted for 100 minutes with one radiograph captured at every one minute interval. The micrographs were analyzed and the fluid front movement in both zones was captured.

Experimental Methods

Materials

Rock Sample. The tight organic-rich carbonate source rock samples used in this study were organic-rich tight carbonate source rocks from a Middle East field. The total organic carbon of this sample was approximately 8.7 wt%. This sample is laminated by Cal-Z layers and steaks of high OMZ layers — appearing in dense deep black color. The mineral content, determined by X-ray diffraction, shows that it is mainly composed of 94.5 wt% calcite, 0.5 wt% dolomite, 2.5 wt% quartz, 0.5 wt% pyrite, 0.6 wt% gypsum, and a minor amount of clay — 0.6 wt% kaolinite and 0.8 wt% illitic clay.

Treatment Fluid. KI was used as the contrast agent in the designed spontaneous imbibition test to enhance the contrast of images. A 5 wt% KI solution was prepared and used as the treatment fluid.

Preparation Procedure of the Thin Section Sample. A thin section of the low permeability organic-rich rock sample with a dimension of 22 × 11 × 3.3 mm (length × width × thickness) was used in this study, Fig. 1. The rock sample cube was first treated with liquid resins to ensure the integrity during sample slicing. After the resin solidified, the rock sample was sliced using a trim saw, and glued to a glass slide. The rock surface was then fine trimmed using a Target surfacing trimmer and polished using a broad triple ion beam mill.

Fig. 1 Pictures of the prepared thin section sample. (a) Front view (22 × 11 mm). The area between the two yellow dash lines contains the OMZ layer. The lamination of the sample is in a horizontal direction. (b) The side view (a thickness of 3.3 mm).

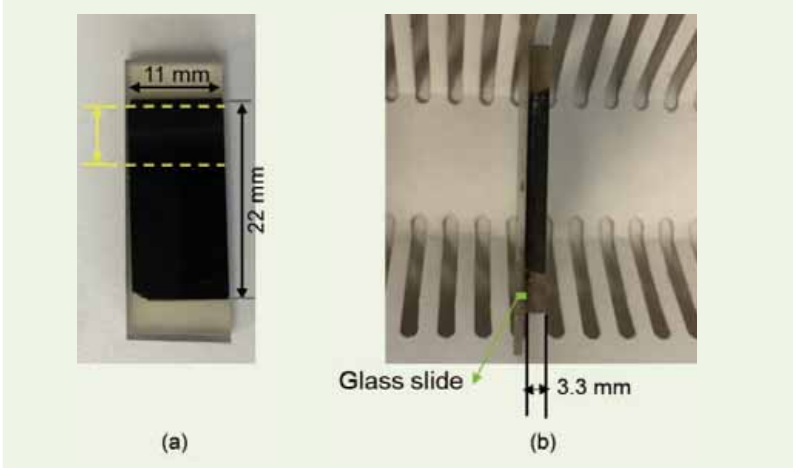

3D Microscale Visualization of Thin Section Rock Sample at As-Received State Using X-ray Micro-Computed Tomography (Micro-CT)

A Nikon HMXST225 micro-CT system was used to image the tight carbonate source rock thin section sample at 5.48 µm and 2.79 µm resolutions, respectively, using 180 kV X-ray and a 2200 × 2200 pixel detector. High resolution is made possible with the tungsten target, the large detector, and optimized positioning of the sample relative to the source and detector. In total, 3,000 projections were collected and reconstructed with 16-bit precision.

Dynamic Study of Spontaneous Imbibition Test Using Microscale Radiographic Imaging

An earlier study has shown that liquid imbibition and ion diffusion rates parallel to the lamination are higher than those in the perpendicular direction[23]. Our imbibition study was conducted using a 5 wt% KI solution along the maximum fluid imbibition rate direction, which is parallel to the lamination. To minimize the gravity effects on the fluid movement rate along the lamination direction, the experiment was designed in the way by placing the thin section sample with lamination in a horizontal direction and the treatment fluid (5 wt% KI solution) soaked sponge on the left side of the sample.

In this way, the fluid imbibition direction is in the horizontal direction, Fig. 2. Then the sample setup was immediately transferred to an X-ray chamber and set up for radiographic imaging — within three minutes. The entire spontaneous imbibition test was conducted for 100 minutes with one X-ray radiograph image taken at one minute intervals. During the acquisition of the images, the sample remained stationary. In other words, the sample was not rotated while the radiographs were taken.

The fluid front of the collected radiographic images was identified by importing them into an in-house Matlab program to spot and measure the sudden change of attenuation along the fluid imbibition direction. Then the distance of fluid front movement was measured/calculated between the sample edge and the fluid front.

Quantification of Treatment Fluid Penetration in Different Regions of the Thin Section Sample

At the end of the spontaneous imbibition test, to further validate the presence of the treatment fluid present in different regions of the thin section sample, scanning electron microscopy (SEM) and energy dispersive spectroscopy (EDS) were used to investigate the elemental concentration in the identified areas.

To do this, the thin section sample was air-dried and mounted onto an aluminum stub with copper tape and imaged. Proper energy (~15 kV) for the electron beam was selected so that the commonly occurring elements could be detected. The working distance is chosen to maximize the signal given the geometry of the EDS probe and the sample surface.

EDS was performed for relatively larger areas to gain the general chemical data in certain areas and also for selected spots with selected elemental concentrations, such as potassium (K) and iodide (I), which were the elements present in the treatment fluid.

Results and Discussion

Surface Characterization

X-ray microscale radiographs of the prepared thin section sample prior to the imbibition test were acquired using 5.48 µm and 2.79 µm resolution, respectively, and the 3D image for each resolution was reconstructed. Figure 3 shows one micro-CT image of the area between the two yellow dash lines in Fig. 1a (11 × 7.9 mm) with the thin section sample prepared from the as-received tight carbonate rock at a resolution of 5.48 µm. It was observed that this area was composed of two distinguished zones; an OMZ layer, shown as a dark-gray band in the middle of the image, and a Cal-Z layer, shown as a light-gray color presented above and below the OMZ layer in Fig. 3.

The OMZ layer in this particular sample was determined to be approximately 1.2 mm in thickness. As documented in our earlier studies[16, 17] with tight carbonate rock samples from the similar field, the Cal-Z zones contains mainly calcite, while the OMZ zones contain more organic matter, less calcite, and more alumino-silicate minerals, such as quartz, feldspar, and

Fig. 3 *Micro-CT image at a resolution of 5.48 µm for the highlighted area in Fig. 1a in the as-received sample. The OMZ layer in this sample is averaged around 1.2 mm.*

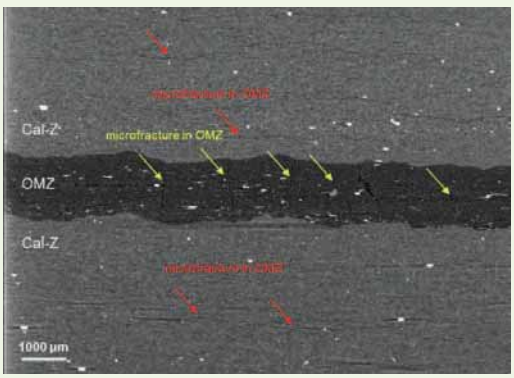

Fig. 2 *Schematic of spontaneous imbibition setup for a thin section sample.*

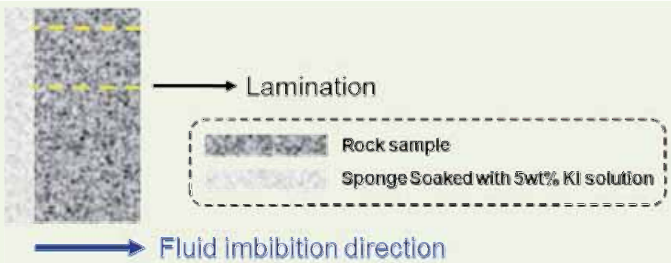

clay minerals in comparison to the Cal-Z zones. Also, minor amounts of dolomite crystals were observed more often in the OMZ zones than in the Cal-Z zones in samples from this particular field. Microfractures were present in both the Cal-Z and OMZ zones on slices of the reconstructed image. Hairlines of microfractures are occasionally seen in the Cal-Z zones and they appear to be parallel to the lamination direction. The length of the microfractures can be up to a few millimeters.

On the other hand, the presence of a higher density of microfractures was observed in the OMZ zones. Figure 4 is a micro-CT image — at a resolution of 2.79 µm. The orientation of these microfractures varies in different directions; some were parallel to the lamination direction while some were perpendicular to the lamination direction. For those perpendicular to the lamination, the microfractures tend to stop at the boundaries between the OMZ and Cal-Z zones.

Large irregular shaped microfractures were also abundant within the OMZ zone. Given what was observed in the high-resolution micro-CT image, it is very difficult to distinguish whether these microfractures were naturally occurring, or induced by the coring, sampling, and thin section sample preparation processes. Extra cautionary steps were considered/taken during the sample preparation steps to minimize the damage. Consequently, there is no guarantee that there was no induced damge to the prepared sample. Due to the fact that large numbers of microfractures will be generated during the hydraulic fracturing process, especially during slick water treatment, this sample could be treated as the original state of the formation sample during the hydraulic fracturing process for the fluid uptake pathway study.

Further image processing was conducted on the reconstructed micro-CT images at a resolution of 2.79 µm. Artificial intelligence (AI) was adopted during the micrograph analysis for fracture segmentation to overcome the challenges with large data set size and the microstructure complexity[24, 25]. Supervised AI can recognize features and patterns within a large set of data that conventional algorithms fail to find. The recognized features, once validated on a smaller scale, can be deployed to automatically process massive amounts of similar data.

In this study, identified data sets for fractures and the matrix were used in the training data sets and the automation for recognizing fractures and the matrix was conducted for the rest of the data sets. The analysis data suggested that there were connected microfracture networks in the OMZ zone.

Figure 5 shows the volume of 3.5 × 1.3 × 2.4 mm (red box in Fig. 5a) where detailed analysis was performed in the OMZ. For the data analysis results shown in Fig. 5b, the green color represents the connected fractures and porosity network while the blue color represents the disconnected porosity at the 2.79 µm image resolution.

Dynamic Study of Spontaneous Imbibition Test Using Microscale Radiographic Imaging

As previously mentioned, the imbibition study was conducted using a 5 wt% KI solution along the maximum fluid imbibition rate direction, i.e., the direction of sample lamination was parallel to the fluid imbibition direction. The entire spontaneous imbibition test was conducted for 100 minutes with one X-ray radiograph image taken at 1 minute intervals. The fluid imbibition direction was from the left to right. Since it took a couple of minutes to set up the experiment and start the imaging process, the first image was taken 4 minutes

Fig. 4 *Micro-CT image at a resolution of 2.79 µm, showing large microfractures within the OMZ layer and vertical fractures terminating at the boundaries.*

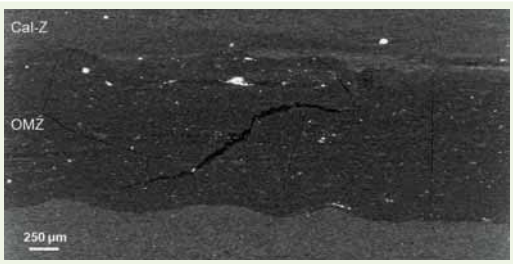

Fig. 5 *(a) A volume of 3.5 × 1.3 × 2.4 mm in the OMZ. (b) A color mapped fracture and porosity network. The green color represents the connected fractures in and porosity network; while the blue color represents the disconnected porosity.*

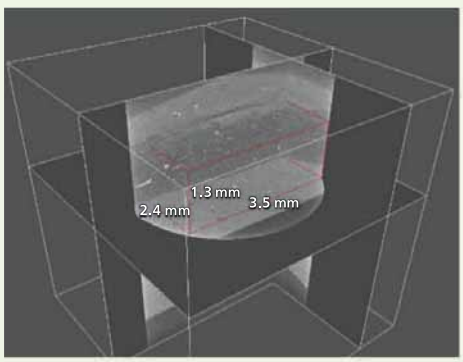

(a)

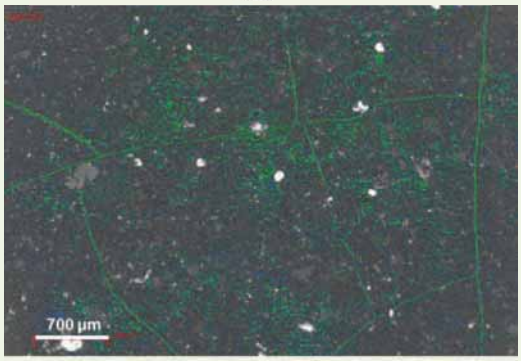

(b)

into the imbibition test, Fig. 6a.

The selected images in Figs. 6b to 6i were the radiographs of the fluid imbibed conditions at different experimental times: 5, 6, 7, 10, 15, 30, 60, and 100 minutes. Due to the high attenuation of the KI fluid, the zones which contain KI fluid appear bright on the radiographs.

The first observation to note from Fig. 6a is that the contrast in the OMZ relative to the Cal-Z was quite different from the original state shown in Fig. 3. The OMZ was much brighter than the Cal-Z in Fig. 6a, which indicates that KI fluid transported very fast in the microfracture abundant OMZ and even at the 4 minute mark of the imbibition test, the fluid front has already moved from one end of the sample to the other side. Throughout the entire experiment, the brightness of the OMZ remains unchanged.

The second phenomena observed in Fig. 6a was that the microfracture abundant areas in the Cal-Z zone are shown as bright strings. This also indicates that the fluid moved very fast in microfractures containing a Cal-Z and the fluid front reached the other end of the sample in less than 4 minutes. While in the calcite-rich matrix, the waterfront progressed very slowly. As can be seen in Fig. 6a, the KI soaked sponge shows up as a vertical bright zone on the left side of the image. At 100 minutes, the KI soaked sponge (very bright) and a KI fluid invasion zone in the Cal-Zs (less bright) are shown on the left side of Fig. 6i. The fluid front is marked in Fig. 6i.

To accurately capture the fluid front movement in the matrix of the Cal-Z, radiograph images at different testing times are zoomed in on the left side, Fig. 7.

To quantify the distance of the fluid front movement in the matrix of the Cal-Zs, a Matlab code was used to automatically pick the brightness change in the images in Fig. 7 in the OMZ. Figure 8a is the radiograph at 100 minutes with the x- and y-axis units both set as pixels. Each pixel in Fig. 8a was 5.5 μm. The fluid invasion depth in the matrix of the Cal-Z was measured by automatic identification of the brightness change in the Cal-Zs. The average brightness in row 0 to 200 (Cal-Z above OMZ) and 400 to 600 (Cal-Z below OMZ) was averaged across Fig. 8a and the derivative of the average brightness was calculated to identify the imbibition zone in the matrix, Fig. 8b.

Fig. 6 *Dynamic study of microscale imaging at different imbibition times: full field of view. (a) t = 4 min, (b) t = 5 min, (c) t = 6 min, (d) t = 7 min, (e) t = 10 min, (f) t = 15 min, (g) t = 30 min, (h) t = 60 min, and (i) t = 100 min.*

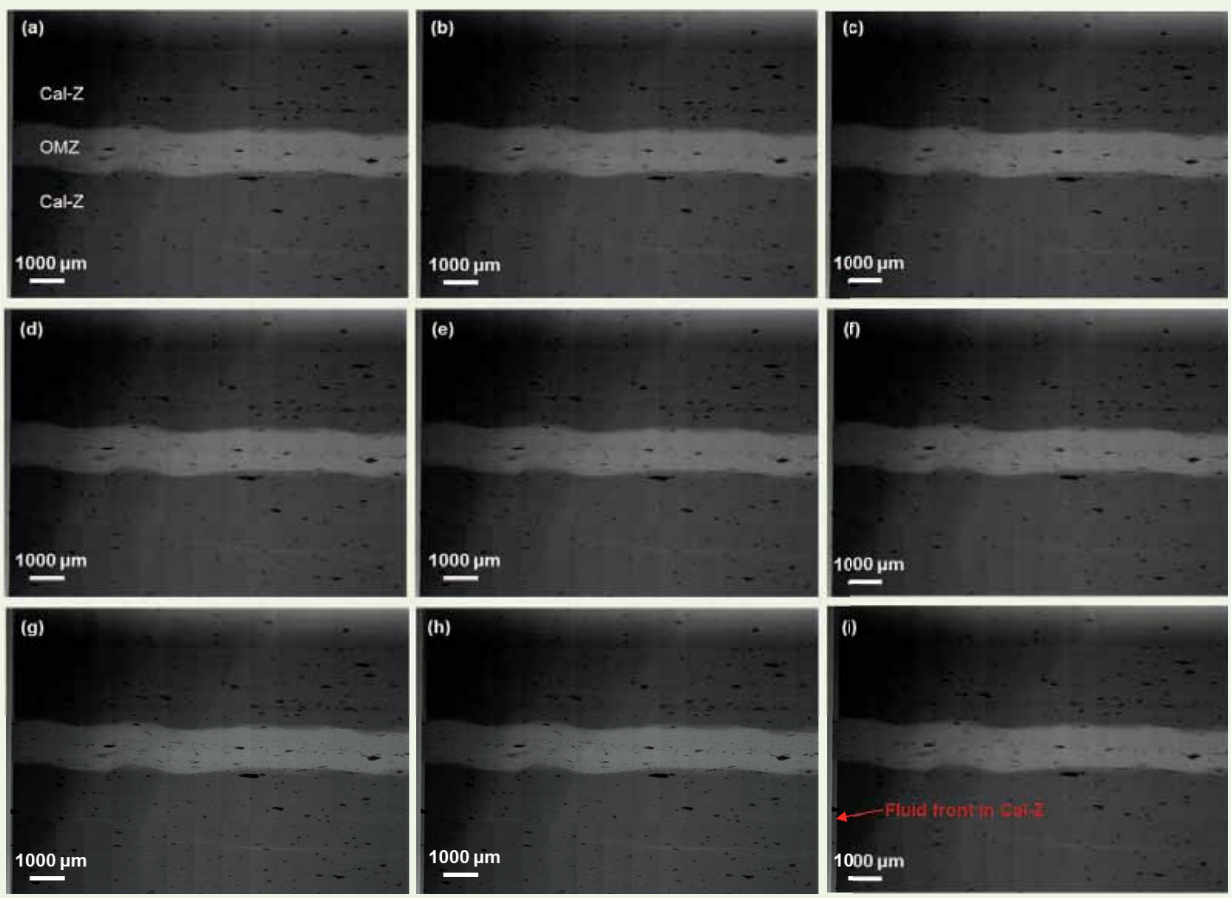

Fig. 7 *Dynamic study of the microscale imaging at different imbibition times: zoomed in section in the fluid contact side. (a) t = 4 min, (b) t = 5 min, (c) t = 6 min, (d) t = 7 min, (e) t = 10 min, (f) t = 15 min, (g) t = 30 min, (h) t = 60 min, and (i) t = 100 min.*

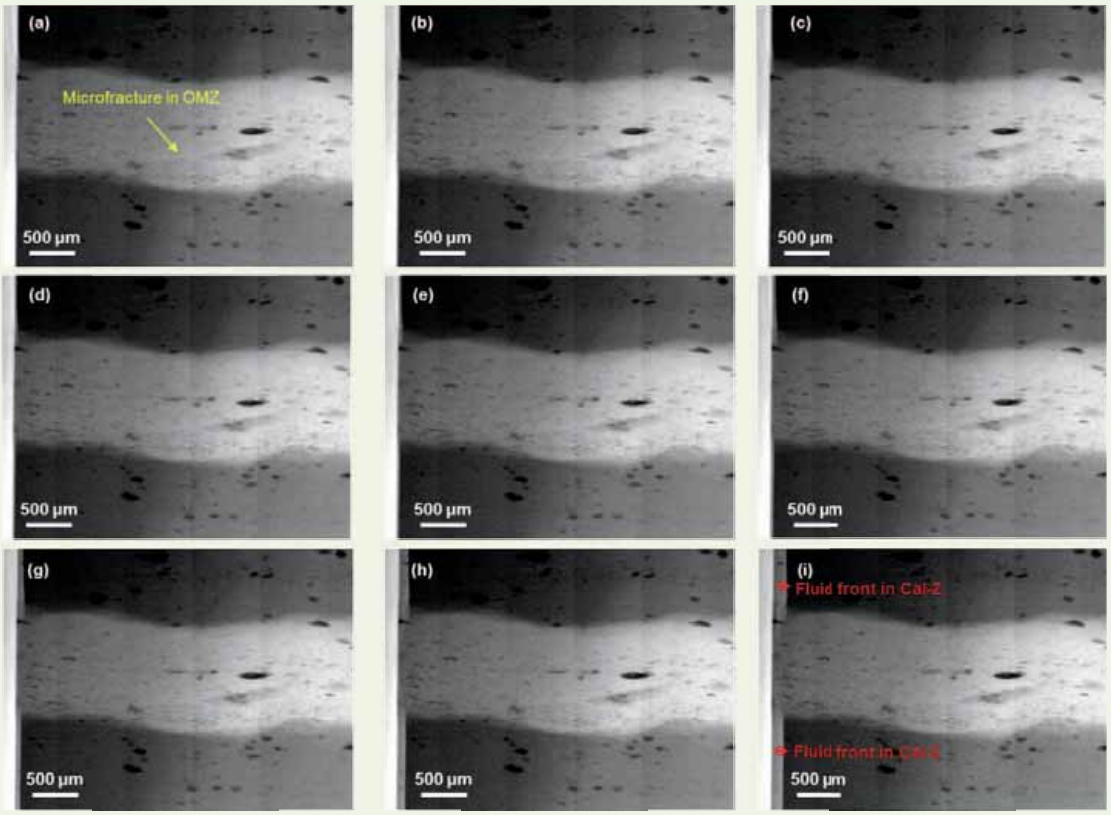

Fig. 8 *(a) An image of the radiograph at a testing time of 100 minutes with the x- and y-axis units both set as pixels. (b) The image process in Matlab showing the plot of change in brightness vs. distance from left edge (pix).*

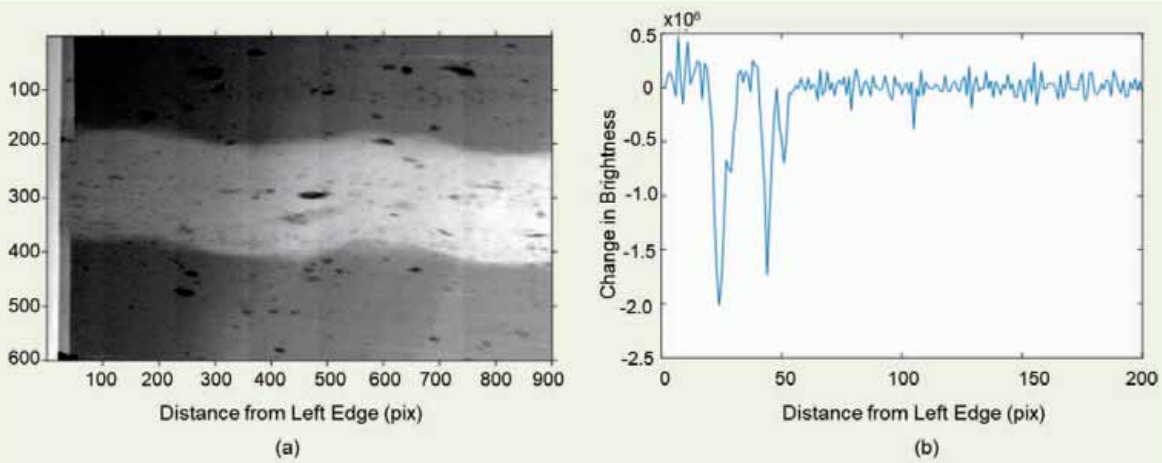

Different from the microfracture dominated areas, the waterfront progressed very slowly in the Cal-Z matrix, to a penetration of about 120 µm in 100 minutes. The same process was carried out for all radiographs collected during the imbibition test. Then the distance of the fluid front movement vs. time was plotted in Fig. 9. Except at the very beginning of the imbibition test, the fluid front movement rate in the matrix of the Cal-Z was calculated to be at about 72 µm/hour.

From this study, we can see that the fluid flow

Fig. 9 *Distance of fluid front movement in the matrix of Cal-Z during spontaneous imbibition determined from dynamic radiograph images.*

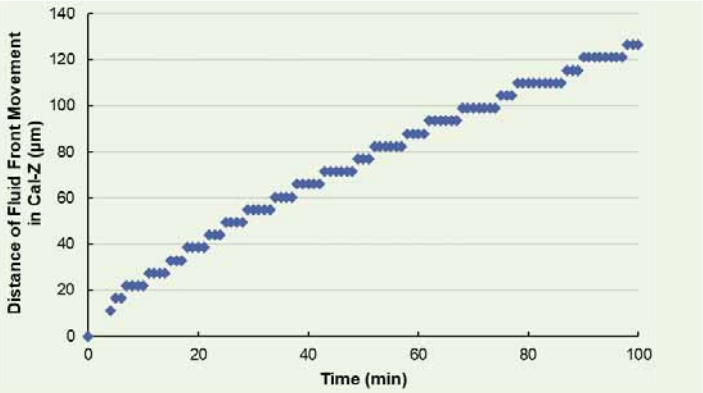

pathways are dominated in the connected fracture networks. The fluid flow in the matrix is much slower than in connected fractures.

Quantification of Treatment Fluid Penetration in Different Regions of the Thin Section Sample

Figure 10a is a second electron SEM image of the OMZ region; Fig. 10b is the backscatter SEM image for the enlarged area shown in the yellow box of Fig. 10a; Figs. 10c and 10d show the elemental maps of silicon (Si) and aluminum (Al) in the yellow framed area in Fig. 10b. In Fig. 10c, the bright yellow spots show the high concentrations of Si, suggesting that they might be quartz gains; the intermediate color shows where the clay minerals. Similar to what we reported earlier[16, 17], the OMZ have other minerals such as aluminosilicate minerals, likely of terrigenous origin, in addition to the carbonate minerals and pyrite. Whereas the Cal-Zs are mainly composed of carbonate minerals and pyrite. It seems that the complexity of mineralogy and the orientation of clay minerals in the OMZ might make the zones easy to cleave, i.e., more fractures tend to occur in the OMZs.

Besides the direct observation from the radiograph images for fluid front movement in different regions, additional EDS analysis was also used to further quantify the elemental concentration of the treatment fluids at the identified areas after the imbibition test. Figure 11 shows the location of the selected points where EDS analysis was done in detail on the concentration of iodide, from the treatment fluid. Points 1, 4, and 5 were inside the microfracture dominated OMZ, with point 1 closer to the treatment fluid and point 5 farthest away from the treatment fluid; points 2 and 3 were inside of the Cal-Zs, where point 2 was inside the invaded zone by the imbibition fluid, whereas point 3

Fig. 10 *(a) A secondary electron SEM overview image of an area in the OMZ. (b) The backscatter SEM image of the yellow framed area in Fig. 10a, showing the bright colored pyrite grains and large irregular shaped pores. (c) An elemental map of Si in the yellow framed area in Fig. 10b. (d) An elemental map of Al in the yellow framed area in Fig. 10b.*

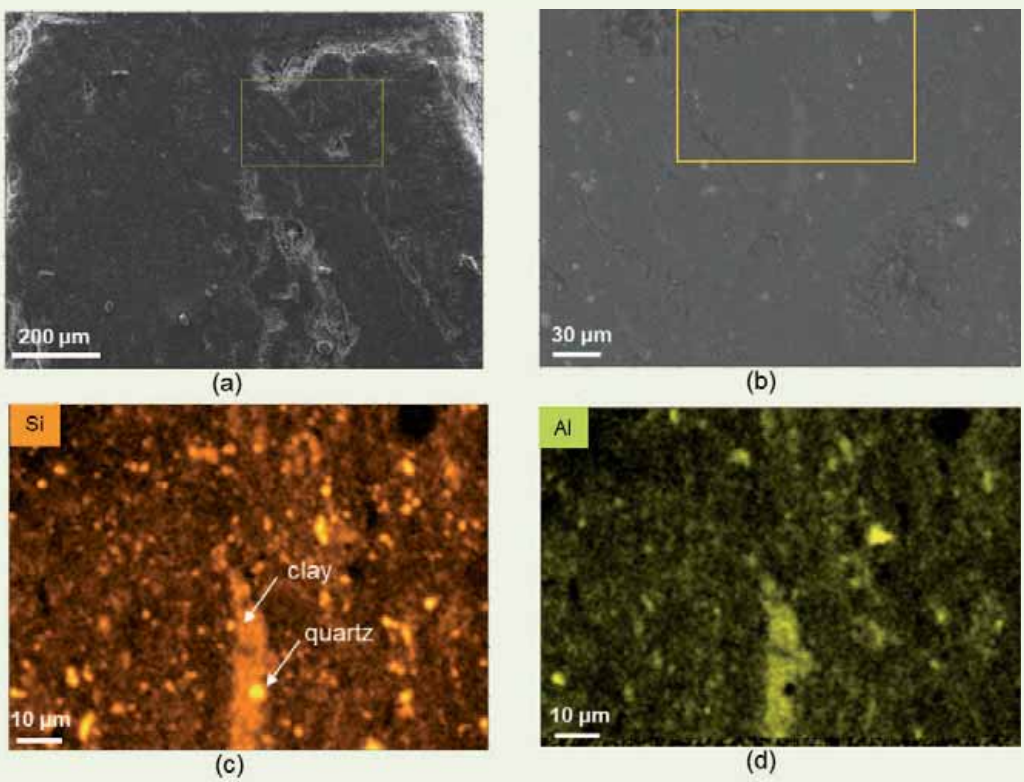

Fig. 11 *EDS mapping for selected sites (points 1 to 5). (a) A zoomed in section of microscale radiographic image at t = 100 min (same as Fig. 7i); (b) A full-field of view for microscale radiographic image at t = 100 min (same as Fig. 6i).*

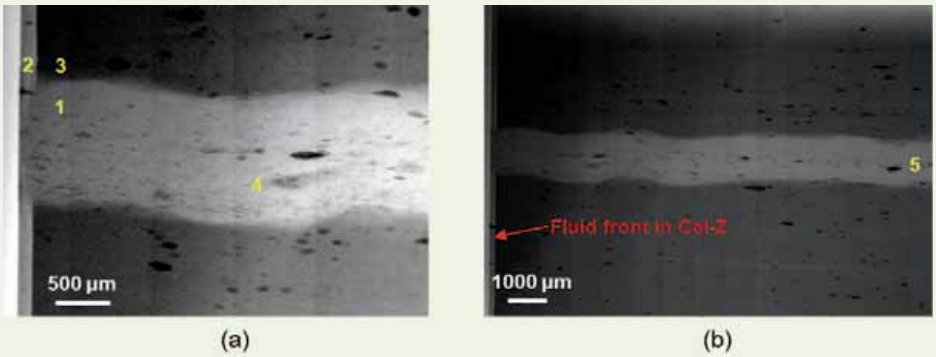

Table 1 *The EDS analysis for the percentage of iodide at points 1 to 5.*

Element	Site 1	Site 2	Site 3	Site 4	Site 5
Iodide (%)	3.54	1.86	1.13	3.23	3.01

was outside the zone.

The iodide concentrations from the EDS analysis at selected points are listed in Table 1. This shows that the iodide concentrations at points 1, 4, and 5 (3.54%, 3.23%, and 3.01%, respectively) are higher than points 2 and 3. The high imbibition rate inside the microfracture abundant OMZ suggests that connected fractures were the main fluid flow path. Also, iodide concentration at point 2 was higher than point 3 since point 2 was within the fluid invaded Cal-Z matrix zone.

The iodine concentration at point 2 was 1.86%, showing the presence of the treatment fluid. The relatively lower concentration from the EDS suggests that not all pores are occupied by the treatment fluid. Point 3 has the lowest iodide concentration as it is outside the invaded zone by the imbibition fluid.

Conclusions

An experiment was conducted to dynamically capture the fluid flow pathways in the spontaneous imbibition test using X-ray imaging for organic-rich tight carbonate rock samples. Microfractures have been observed by radiographic imaging in the thin section sample with 5.48 µm and 2.79 µm resolutions before the fluid treatment, both in the OMZ and the Cal-Z. The imbibition test was performed for 100 minutes with one radiograph image taken per minute.

Different fluid uptake features were revealed in this dynamic fluid imbibition study. The fluid traveled very fast and reached the other end of the sample in less than 4 minutes in microfractures, both within the OMZ and Cal-Z. The waterfront progressed very slowly in the calcite-rich matrix. This indicates that the main fluid flow pathways for fracturing fluid could be within the connected fracture network, instead of the matrix.

Acknowledgments

This article was prepared for presentation at the International Petroleum Technology Conference, Dhahran, Saudi Arabia, January 13-15, 2020.

The authors would like to thank DigiM Solution LLC for the assistance of the microscale radiographic imaging work and Josh Brothers for assisting in the SEM and EDS analysis used in this study. The authors also would like to give special thanks to James Howard from DigiM Solution LLC and Dr. Jinhong Chen from Aramco Services Company for valuable discussions.

References

1. O'Brien, P., Onyia, D. and Astarita, G.: "Middle East Bucking the Trend in Drive for New EOR Technology," *Exploration & Production*, August 2015. *https://www.epmag.com/middle-east-bucking-trend-drive-new-eor-technology-812011.*
2. McLeod, H.O.: "Matrix Acidizing," *Journal of Petroleum Technology*, Vol. 36, Issue 12, December 1984, pp. 2055-2069.
3. Olsen, T.N. and Karr IV, G.K.: "Treatment Optimization of Acid Fracturing in Carbonate Formations," SPE paper 15165, presented at the SPE Rocky Mountain Regional Meeting, Billings, Montana, May 19-21, 1986.
4. McLeod, H.O.: "Significant Factors for Successful Matrix Acidizing," SPE paper 20155, presented at the SPE Centennial Symposium at New Mexico Tech, Socorro, New Mexico, October 16-19, 1989.
5. Bybee, K.: "Acid Fracturing a Carbonate Reservoir," *Journal of Petroleum Technology*, Vol. 56, Issue 7, July 2004, pp. 49-52.
6. Nelson, P.H.: "Pore Throat Sizes in Sandstones, Tight Sandstones, and Shales," *AAPG Bulletin*, Vol. 93, Issue 3, March 2009, pp. 329-340.

7. Sondergeld, C.H., Ambrose, R.J., Rai, C.S. and Moncrieff, J.: "Micro-Structural Studies of Gas Shales," SPE paper 131771, presented at the SPE Unconventional Gas Conference, Pittsburgh, Pennsylvania, February 23-25, 2010.

8. Loucks, R.G., Reed, R.M., Ruppel, S.C. and Hammes, U.: "Spectrum of Pore Types and Networks in Mudrocks and a Descriptive Classification for Matrix-Related Mudrock Pores," *AAPG Bulletin*, Vol. 96, Issue 6, June 2012, pp. 1071-1098.

9. Cheng, Y.: "Impact of Water Dynamics in Fractures on the Performance of Hydraulically Fractured Wells in Gas-Shale Reservoirs," *Journal of Canandian Petroleum Technology*, Vol. 51, Issue 2, March 2012, pp. 143-151.

10. King, G.: "Hydraulic Fracturing 101: What Every Representative, Environmentalist, Regulator, Reporter, Investor, University Researcher, Neighbor, and Engineer Should Know About Estimating Frac Risk," *Journal of Petroleum Technology*, Vol. 64, Issue 4, April 2012, pp. 34-42.

11. Soeder, D.J.: *Unconventional: The Development of Natural Gas from the Marcellus Shale*, Vol. 527, Boulder, Colorado: Geological Society of America, 2017, 143 p.

12. Akrad, O., Miskimins, J. and Prasad, M.: "The Effects of Fracturing Fluids on Shale Rock Mechanical Properties and Proppant Embedment," SPE paper 146658, presented at the SPE Annual Technical Conference and Exhibition, Denver, Colorado, October 30-November 2, 2011.

13. Lai, B., Liang, F., Zhang, J., Li, L., et al.: "Fracturing Fluids Effects on Mechanical Properties of Organic Rich Shale," paper ARMA-2016-180 presented at the 50th US. Rock Mechanics/Geomechanics Symposium, Houston, Texas, June 26-29, 2016.

14. Anders, M.H., Laubach, S.E. and Scholz, C.H.: "Microfractures: A Review," *Journal of Structural Geology*, Vol. 69, Part B, December 2014, pp. 377-394.

15. Gale, J.F.W., Laubach, S.E., Olson, J.E., Eichhubl, P., et al.: "Natural Fractures in Shale: A Review and New Observations," *AAPG Bulletin*, Vol. 98, Issue 11, 2014, pp. 2165-2216.

16. Liang, F., Lai, B., Zhang, J., Liu, H-H., et al.: "An Experimental Study on Interactions between Imbibed Fracturing Fluid and Organic-Rich Tight Carbonate Source Rocks," *SPE Journal*, Vol. 23, Issue 6, December 2018, pp. 2133-2146.

17. Liang, F., Zhang, J., Liu, H-H. and Bartko, K.M.: "Multiscale Experimental Studies on Interactions between Aqueous-Based Fracturing Fluids and Tight Organic-Rich Carbonate Source Rocks," *SPE Reservoir Evaluation & Engineering*, Vol. 22, Issue 2, May 2019, pp. 402-417.

18. Laubach, S.E., Olson, J.E. and Gale, J.F.W.: "Are Open Fractures Necessarily Aligned with Maximum Horizontal Stress?" *Earth and Planetary Science Letters*, Vol. 222, Issue 1, May 2004, pp. 191-195.

19. Khan, M. and Teufel, L.W.: "The Effect of Geological and Geomechanical Parameters on Reservoir Stress Path and Its Importance in Studying Permeability Anisotropy," *SPE Reservoir Evaluation & Engineering*, Vol. 3, Issue 5, October 2000, pp. 394-400.

20. Muralidharan, V., Putra, E. and Schechter, D.S.: "Experimental and Simulation Analysis of Fractured Reservoir Experiencing Different Stress Conditions," paper PETSOC-2004-229, presented at the Canadian International Petroleum Conference, Calgary, Alberta, Canada, June 8-10, 2004.

21. Abass, H.H., Ortiz, I., Khan, M.R., Beresky, J.K., et al.: "Understanding Stress Dependant Permeability of Matrix, Natural Fractures, and Hydraulic Fractures in Carbonate Formations," SPE paper 110973, presented at the SPE Saudi Arabia Section Technical Symposium, Dhahran, Saudi Arabia, May 7-8, 2007.

22. Lavrov, A.: "Fracture Permeability under Normal Stress: A Fully Computational Approach," *Journal of Petroleum Exploration and Production Technology*, Vol. 7, 2017, pp. 181-194.

23. Ghanbari, E. and Dehghanpour, H.: "Impact of Rock Fabric on Water Imbibition and Salt Diffusion in Gas Shales," *International Journal of Coal Geology*, Vol. 138, January 2015, pp. 55-67.

24. Howard, J., Lin, S. and Zhang, S.: "Uncertainty Quantification in Image Segmentation for Image-Based Rock Physics in a Shaly Sandstone," *Petrophysics*, Vol. 60, Issue 2, April 2019, pp. 240-254.

25. Zhang, S., Byrnes, A.P., Jankovic, J. and Neilly, J.: "Management, Analysis, and Simulation of Micrographs with Cloud Computing," *Microscopy Today*, Vol. 29, Issue 2, March 2019, pp. 26-33.

About the Authors

Dr. Feng Liang

Ph.D. in Organic Chemistry, Rice University

Dr. Feng Liang is currently a Research Science Specialist at the Aramco Americas (formally Aramco Services Company), Aramco Research Center-Houston. She has now been with the company for over seven years.

Prior to joining the Aramco Research Center, Feng was a Principal Scientist at Halliburton for nearly eight years. Her research interests are the new materials and product development in fracturing fluid, advanced fluid additives, waterless fracturing technologies, biodegradable diversion materials, sand control products, cement additives, and nanomaterial reinforced elastomers.

Feng is a contributor to many patents and technical papers. She holds over 60 issued U.S. patents and 30 additional published patent applications. Feng is the author and coauthor of more than 80 technical papers, with a few in very high impact factor journals such as the *Journal of the American Chemical Society* and *Nano Letters*. She has also coauthored two book chapters as well. Feng's publications have received over 3,800 citations.

She is a member of the Society of Petroleum Engineers (SPE) and the American Chemical Society (ACS). Feng received the 2017 SPE Production and Operations Award for the Gulf Coast North American Region. She also received the 2017 Effective Publication Award from Saudi Aramco's Exploration and Petroleum Engineering Center – Advanced Research Center (EXPEC ARC).

Feng received her Ph.D. degree in Organic Chemistry from Rice University, Houston, TX.

Jilin Zhang

M.S. in Geology, University of Houston

Jilin Zhang joined the Aramco Services Company, Aramco Research Center-Houston, in 2013 as a Petroleum Engineer.

Prior to this, he was a Petrophysical Consultant at Formation and Reservoir Services of Halliburton; a Petrophysicist/Senior Geoscientist at Baker Hughes, a Manager of Geology with Ellington & Associates, an X-ray Powder Diffraction Petrographer with OMNI Labs, and also held several positions in China from 1985 to 1994.

Jilin received his M.S. degree in Geology from the University of Houston, Houston, TX, majoring in carbonate petrography and diagenesis. He also received an M.S. degree in Marine Geology from the Ocean University of China, Qingdao, China, focusing on modern sedimentation of clastic rocks.

Jilin's expertise is in mineralogy in general, and petrophysics in shale and carbonate rocks.

Dr. Hui-Hai Liu

Ph.D. in Soil Physics, Auburn University

Dr. Hui-Hai Liu is a Senior Petroleum Engineering Consultant at the Aramco Research Center in Houston. Before joining Aramco in 2014, he was a Staff Scientist and the Head of the Hydrogeology and Reservoir Dynamics Department at Lawrence Berkeley National Laboratory (LBNL) and an Adjunct Distinguished Professor at the China University of Mining and Technology in Beijing.

Hui-Hai has more than 25 years of experience in developing models for subsurface fluid flow and coupled hydromechanical processes, and in applying them to shale gas recovery, carbon dioxide geological sequestration, and enhanced coalbed methane recovery, geological disposal of high-level nuclear waste, and groundwater flow and transport. Since joining Aramco, he has focused on research activities related to reservoir property measurement and production prediction for unconventional reservoirs.

Hui-Hai's work has been documented in one book, more than 130 peer-reviewed journal articles, and numerous patents. He has received several awards for his research and achievements, including the Society of Petroleum Engineers (SPE) Distinguished Membership, the LBNL Director's Award for Exceptional Achievement, Fellowship of the Geological Society of America, and the Emil Truog Research Award from the Soil Science Society of America.

Hui-Hai received his B.S. in Mechanical Engineering from Beijing Agricultural Engineering University, Beijing, China, his M.S. degree in Applied Fluid Mechanics from Huazhong University of Science and Technology, Wuhan, China, and a Ph.D. degree in Soil Physics (Multiphase Flow in Porous Media) from Auburn University, Auburn, AL.

Dr. Shawn Zhang

Ph.D. in Computational Physics, Rutgers University

Dr. Shawn Zhang is the founder and Managing Director of DigiM Solution LLC. Before starting the Boston-based company, Shawn held senior positions at Fluent (now Ansys) and FEI (now ThermoFisher), where he played instrumental roles in software design, development and the management of sales and application teams. Shawn and his team developed commercially successful computational fluid dynamics software Fluent, image processing software Avizo, and 3D visualization software Open Inventor.

Shawn is passionate about the combined power of imaging and numerical simulation, with over 100 related publications and multiple pending patents. He and his DigiM team lead the oil and gas industry in micro-imaging and digital rock physics with cloud-based DigiM I2S software platform.

Shawn received his Ph.D. degree in Computational Physics and a minor in Computer Engineering from Rutgers University, New Brunswick, NJ.

Extending Squeeze Life through Improved Interaction between Inhibitor and Rock for Iron Sulfide Inhibition

Lena Petrozziello, Dr. Christoph Kayser, Dr. Cyril Okocha, Dr. Tao Chen and Dr. Qiwei Wang

Abstract /

Iron sulfide (FeS) deposition is a ubiquitous phenomenon in sour oil and gas wells and presents unique challenges for its control and management downhole. The majority of current FeS anti-scale chemical technologies tend to be "reactive" rather than "proactive" for downhole scale mitigation, and currently there are few FeS scale inhibitor squeeze options available.

This article details work performed to modify an existing novel and unique sulfide scale inhibitor to further enhance its efficacy and to reconfigure the polymer molecule structure for improved adsorption/desorption behavior sufficient to allow the squeeze application for control and mitigation of FeS scale downhole.

All new polymeric inhibitor chemistries were tailored for high total dissolved solid (TDS) and high downhole temperature chalk sour gas well application. Further ranking was performed via automated static adsorption tests, FeS efficacy tests, and high calcium brine compatibility jar tests to identify the best squeeze applicable candidates for final formation damage coreflood testing.

Introduction of a new anchor group functionality into the polymer resulted in improved adsorption behavior (identified via the static adsorption test), while having minimal impact on the inhibitor's high TDS calcium brine tolerance and also on its FeS scale inhibitor performance. The kinetic adsorption study showed > 2 mg inhibitor/g rock adsorption on field analogous chalk rock, which is markedly higher compared to the original parent sulfide inhibitor molecule or other new polymeric variants synthesized without the new anchor groups. FeS scale inhibitor adsorption was further improved by optimizing the ratio of monomer and functional groups on the polymer. Simulated field squeeze coreflood testing revealed no appreciable formation damage to the outcrop core analogue under simulated field application conditions, and the new variant inhibitor chemicals also showed useful adsorption/desorption behavior.

The new polymeric scale inhibitors are suitable for both continuous injection and squeeze application for control of the FeS scale in high temperature and high calcium ion sour gas chalk wells. For the squeeze application, testing revealed a low formation damage potential combined with significant chemical retention for potentially extended squeeze lifetime in the field. Ultimately, this technology heralds a new era in downhole scale management for sour producer wells plagued by FeS scale via reduction of treatment frequency for assured well integrity.

Introduction

Chemical squeeze treatment is currently the oil industry's preferred mineral scale control technique for prevention of downhole scale deposition from the producer well's near wellbore formation to the wellhead and topside process. The bulk of scale inhibitor squeeze treatments performed historically have targeted the sparingly soluble metal carbonates and sulfates, and more recently halites, and have employed increasingly sophisticated water-soluble phosphonate and polymeric chemistries and application technologies to achieve this task[1-5].

The sulfide salts of iron, lead, and zinc are also important mineral scales and are typified by their intensly water insoluble nature. Metal sulfide scales occur across the globe and are becoming of increasing importance as older oil fields mature and sour, and newer sour oil field developments are brought into production[6-8]. Unlike carbonate and sulfate scales, the scale squeeze options available for control and mitigation of metal sulfide scales downhole are limited, and this is due to the poor sulfide scale control performance shown by the greater majority of conventional commercially available squeeze chemistries.

Recent studies have shown that novel polymeric scale inhibitors offer a highly effective solution for inhibition control and management of metal sulfide scales[9]. Following commercial introduction, the new polymeric sulfide scale inhibitor has been deployed in multifunctional chemical formulations to treat topside flow lines and is regularly included as a key additive in multiple fracking treatments in sour well completions. To date,

the active polymeric has not yet been deployed as a stand-alone sulfide squeeze scale inhibitor due to its: (1) modest retention and release behavior, observed in coreflood experiments using field analogous chalk and sandstone cores, and (2) its low loading capacity for squeeze treatment maintreatment pills.

The distribution of functional groups along the inhibitor backbone was believed responsible for the suboptimal retention and release behavior, while its high molecular weight is implicated in its low main treatment pill loading potential. The disadvantage of many polymeric squeeze scale inhibitors historically has been the lower adsorption/desorption performances of polymerics compared to phosphonates[4, 10-12]; however, the gap is rapidly narrowing with the introduction of new and novel polymer/phosphonate hybrid chemistries into the scale squeeze market[13-15].

The focus of this article is to present the chemical synthesis pathway and detail laboratory performance testing performed to engineer a second generation polymeric sulfide scale inhibitor capable of effective scale squeeze application for control and management of sulfide scale downhole in affected producer wells. More specifically, the new sulfide scale inhibitor was configured for enhanced iron sulfide (FeS) scale control and for squeeze application in high temperature and high TDS brines in sour chalk gas condensate wells.

The scale inhibitor is suitable for all metal sulfide scale control issues and can be deployed either as a stand-alone squeeze inhibitor, or as a component in multifunctional formulations, or as an additive for well interventions in sour gas systems.

Experimental Methods and Analysis

The scale inhibitor FeS efficacy laboratory tests used in this article are either standard or slightly modified accepted industry test procedures.

Scale Inhibitor Performance Jar Testing

The FeS scale inhibitor performance was assessed via static jar testing. The iron ion, bisulfide ion, and polymer test brines were prepared in a deoxygenated synthetic formation water solvent, Table 1, and contained: (1) 100 parts per million (ppm) $FeCl_2.4H_2O$ pH 1.5 for the cation brine, (2) 750 ppm $Na_2S{\cdot}_9H_2O$ for the anion brine, and (3) 10 g/L polymer stock solution, respectively. The tests were performed under low oxygen conditions (< 20 ppm) and the test brine mixtures were prepared at room temperature.

The test "blank" was prepared by adding 5 mL of the cation solution (1) into a tube followed by 5 mL of the anion solution (2). The test "control" was prepared by adding 5 mL of the cation solution (1) into a tube followed by 5 mL of synthetic formation water. Inhibitor performance test solutions were prepared by adding the inhibitor solution (100 or 150 µL of polymer solution (3)) to the test tube followed by 5 mL of cation solution (1) and then 5 mL of anion solution (2). The final solution pH for all test mixtures was approximately pH 6 to 7. All solutions were thoroughly agitated before storing at 2 and 24 hours at 95 °C. FeS scale formation was identified by the development of black solid FeS precipitate. The scale inhibitor performance was evaluated by analyzing the quantity of dispersed FeS in solution via inductively coupled plasma atomic emission spectrophotometry (ICP-OES).

Scale Inhibitor Brine Compatibility Test

The brine compatibility test was performed using 10% polymer solutions prepared in a high calcium test brine. Table 2 lists the brine composition used for compatibility and static adsorption tests. The test samples were heated for 24 hours at 130 °C, and then evaluated for visual indications of brine incompatibility, i.e., hazing or precipitation.

Scale Inhibitor Static Adsorption Test

The scale inhibitor adsorption behavior was assessed via automated static adsorption jar testing. The 500 ppm solutions of the FeS inhibitor was prepared using the static adsorption test bine. The 150 mesh field

Table 1 *The synthetic formation of the test brines prepared in a deoxygenated synthetic formation water solvent.*

Salt	Cation (g/L)	Anion (g/L)
NaCl	49.12	49.12
KCl	1.59	—
$MgCl_2.6H_2O$	15.65	—
$CaCl_2$	8.96	—
$SrCl_2.6H_2O$	1.77	—
$BaCl_2.2H_2O$	0.45	—
$FeCl_2.4H_2O$	0.71 (= 100 ppm Fe^{2+})	—
$Na_2S.9H_2O$	—	11.2 (= 750 ppm S^{2-})

Table 2 *A list of brines used for the compatibility and static adsorption tests.*

Species	Composition (mg/L)
Na^+	21,500
K^+	3,513
Mg^{2+}	525
Ca^{2+}	19,200
Sr^{2+}	1,200
Ba^{2+}	4.7
Fe^{2+}	0
Cl^-	51,700

analogous chalk core particles were added in the solution in a 1:10 solution ratio. The test mixtures were thoroughly agitated prior to heating to 95 °C. Each test brine was subsampled at 0 hour, 1 hour, 4 hours, and 20 hours, and filtered prior to the polymer assay via ICP-OES.

FeS Scale Inhibior Chemical Development

The goal of the molecular synthesis was to develop a squeezable polymeric scale inhibitor for FeS mitigation downhole in high temperature chalk wells. The inhibitor was engineered for improved interaction with the formed FeS particle and its stabilization in high calcium, high TDS produced water. Additionally, the polymer would incorporate a new anchor group functionality to promote adsorption/desorption behavior for the squeeze application.

The squeezable FeS scale inhibitor polymer contained three monomer types: (1) "A" anionic, hydrophilic monomer for dispersion and stabilization in the formation water, (2) "B" amine functionalized monomer for interaction with sulfide scale, and (3) "C" monomer containing anchoring functionality for adsorption retention onto the formation rock.

FeS Particle Interaction

A series of lower molecular weight copolymers were prepared containing different Type B amine functionalised monomers. The new polymers were then tested via static jar testing to assess their scale inhibition potential for FeS with a polymer concentration of 50 ppm, 100 ppm, and 150 ppm after 2 hours and 24 hours.

Figure 1 presents a selection of FeS scale inhibition test results for copolymers containing different amine functionalized monomers and are numbered polymers, P-1 to P-12. Also featured are the results for the reference sulfide scale inhibitor. In this example, polymers P-1, P-2, and P-7 were the only three polymers of the test series that showed appreciable FeS scale inhibitor performance. The performance of polymers P-1 and P-2 were comparable to the reference inhibitor, and both copolymers featured monomers containing 2° amino groups. Polymer P-7 featured a 4° amine.

Those copolymer variants featuring 1° and 3° amino and amide group functionalities showed less or even no interaction and dispersion of the FeS scale particles. The interaction efficency of the amino group-based monomers was ranked as: 2° amino group > 4° amino group > 3° amino group > 1° amido group.

Enhancing Polymer Adsorption

Polymers P-1, P-2, and P-7 provided backbone structures for the following synthesis stage designed to identify: (1) the most effective Type C monomer, (2) its proportion, and (3) distribution for imparting useful adsorption/desorption behavior to the FeS scale inhibitor.

Figure 2 presents the static adsorption test results for the top six best ranked inhibitors: A6, A10, B7, B9, C5, and C8. All showed > 90% FeS inhibition after 2 hours at 150 ppm, and > 70% inhibition after 24 hours — apart from A10 and B9, which showed < 30% after 24 hours. Besides the new polymer species, an industry standard "good adsorber" scale inhibitor and a "poor adsorber" (reference sulfide scale inhibitor) were tested. All new variant polymers showed adsorption behavior profiles between the reference inhibitor profiles.

Copolymers A6, B7, C5, and C8 showed > 2 mg scale

Fig. 1 *An example of the evaluation of the copolymer FeS scale inhibition efficacy.*

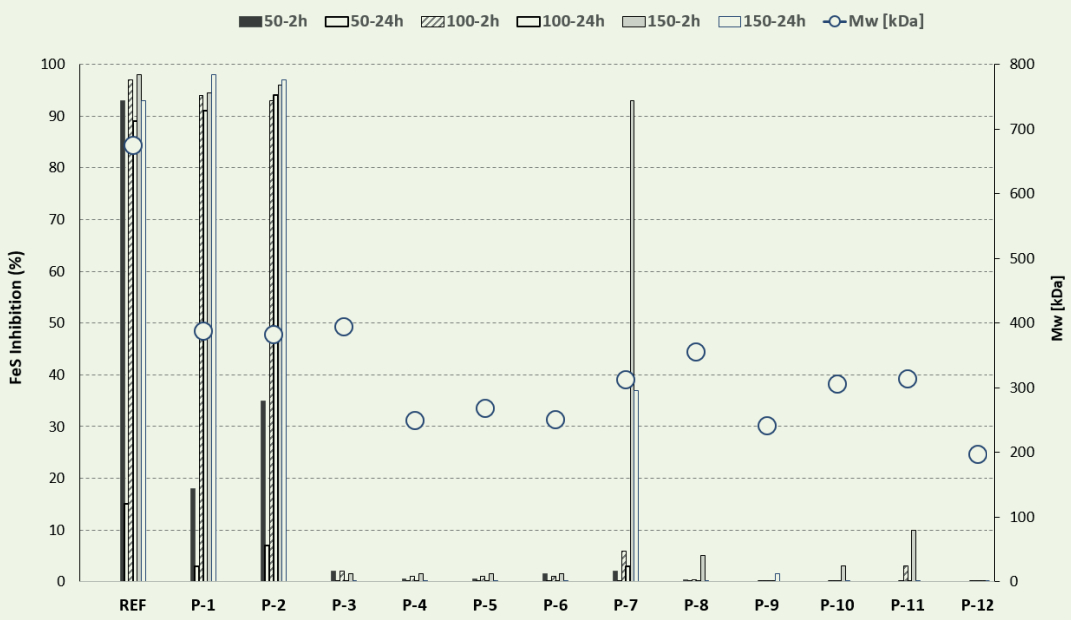

Fig. 2 *The FeS scale inhibitor adsorption performances on the chalk core analogue.*

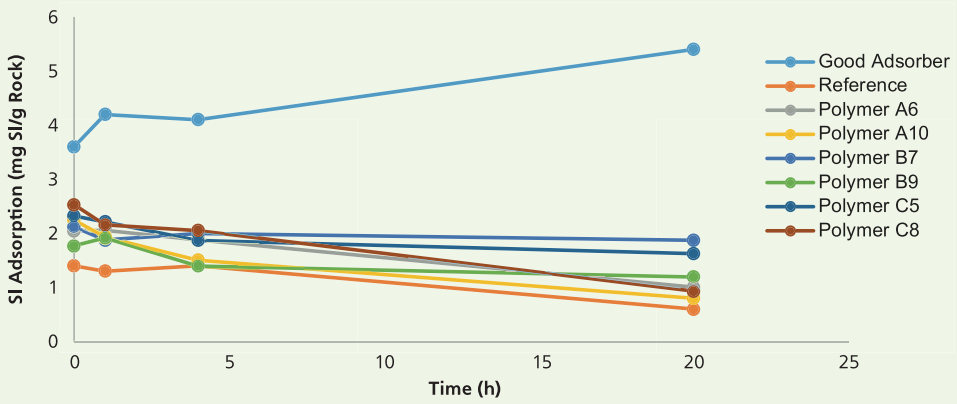

inhibitor/g rock after 0 hour, 1 hour, and 4 hours. At 20 hours, all test inhibitors showed reduced adsorption, but were still higher than the reference. Variants A6, A10, B7, C5, and C8 were therefore considered suitable for further testing for their squeeze application potential.

Brine Compatibility

The new polymeric scale inhibitors for FeS were generated for the squeeze application in high temperature, high calcium, and high TDS environments. Therefore, all of the new ranked polymer variants from each synthesis stage were assessed with respect to their compatibility in synthetic high calcium/high TDS brine, which is comparable to the formation brine, at 130 °C and 10% concentration, see Table 2 for the brine compatibility test.

Figure 3 provides a good example of brine compatibility tests for five selected polymers identified as A6-A10. All polymers successfully passed the 10% brine compatibility test and were then tested under the same conditions at 20% application concentration. After 24 hours and 130 °C, only variants A6 and A10 were compatible at a 20% concentration.

Chemical Development Summary

Using the existing polymeric sulfide scale inhibitor molecule as a basis, the synthesis program identified three key monomer types, which were optimized with respect to: (1) the most effective monomer type, (2) the monomer proportions, and (3) the monomer distributions for imparting FeS inhibition, adsorption/desorption behavior and high temperature and high calcium brine stability. The FeS scale inhibition performance showed comparable results to the reference sulfide scale inhibitor polymer, even after introduction of the third monomer unit for squeeze adsorption functionality.

From the top six inhibitors previously identified and presented in Fig. 2, new variant polymer products A6, B7, and C5 were considered best ranked overall. These polymers showed the best scale inhibition performance with good adsorption behavior on the chalk core analogue and were compatible with high calcium brine at high temperature.

Polymers A6, B7, and C5 were therefore recommended for final stage selection via formation damage coreflood testing under simulated field application conditions.

Formation Damage Coreflood Tests

The goal of the formation damage coreflood test was to: (1) assess the impact of the application of the FeS squeeze scale inhibitor variants A6, B7, and C5 on the chalk field core analogue porosity, permeability, and matrix integrity, and (2) to provide data on their retention and release characteristics when the squeeze scale inhibitor is deployed into a field chalk core analogue under simulated field application conditions.

Fig. 3 *The compatibility test of 10% polymers in high calcium brine before (top) and after heating (bottom).*

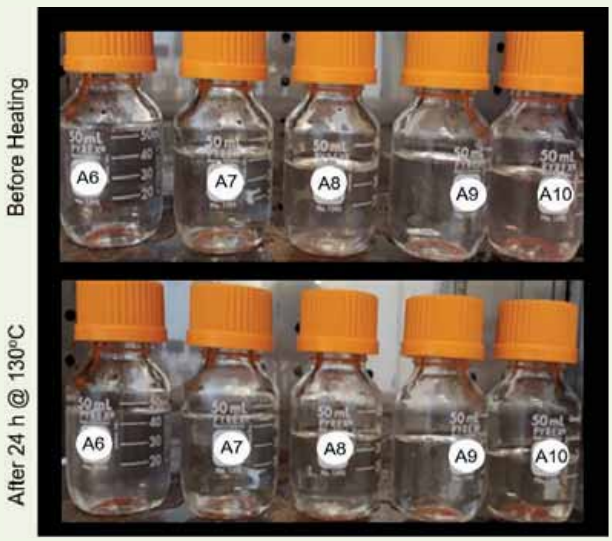

To be considered for field application, the deployed polymeric FeS scale inhibitor was required to show minimal deleterious fluid transmissibility impact on the field analogous chalk substrate, and also demonstrate useful adsorption/desorption behavior.

Coreflood Plugs

The chalk core analogue outcrop was used in the coreflood tests in lieu of the field core due to its similar permeability and porosity characteristics, Table 3.

Test Parameters

Table 4 details the coreflood experiment test parameters.

Gas

Nitrogen gas was used as the gas analogue. The gas was humidified by flow through a bubble cell at test temperature and pressure. Humidification was included to minimize brine evaporation into the gas phase, as this could result in salt precipitation in the core and impact the formation damage assessment.

Oil

Isopar™ was used as a synthetic oil phase for the formation damage corefloods as it was considered to be a good viscosity analogue for field condensate. Measures were taken to ensure that the Isopar™ viscosity was maintained at the supplied viscosity.

Procedure

Table 5 lists the coreflood treatment sequence.

Table 3 *The chalk core analogue outcrop core characteristics.*

	Chalk Outcrop
Formation	Silurian
Permeability	2 mD to 10 mD
Porosity	9% to 10%
Unconfined Compressive Strength	9,000 psi to 12,000 psi

Table 4 *The coreflood experiment test parameters.*

Parameter	Value
Test Temperature	143 °C
Injection Temperature	143 °C
Pore Pressure	500 psi
Net Overburden Pressure	1,500 psi
Overburden (confining) Pressure	2,000 psi
Fluid Flow Rate	4 mL/min
Shut-in	24 hours

Test Brines

Table 6 lists the coreflood brine composition used. The original formation water brine composition was adjusted and simplified to comprise sodium, calcium, magnesium, and chloride only, with NaCl used to adjust the ion balance for removed cation and anion species. All test brines were filtered (0.45 μm) and degassed prior to use.

The scale inhibitor main treatment slug was prepared in 4% NaCl brine — injection brine solvent equivalent.

Results

Residual Scale Inhibitor (RSI) Profile — Plateau Phase

For speed and convenience, the residual scale inhibitor (RSI) concentration was assessed via inductively coupled plasma (ICP) — sulfur — of the coreflood eluate samples for the FeS inhibitors A6, B7, and C5. Figure 4 shows the RSI decay profile "plateau" or "working" phase.

The RSI profiles for the individual A6, B7, and C5 corefloods are collectively plotted for comparisons purposes. In Fig. 4 the RSI decay profile plateau phases for the A6, B7, and C5 corefloods are long and suggest the potential for significant squeeze lifetime at a high average. For comparison, a typical decay profile for the reference sulfide scale inhibitor is overlaid on the same plot. The reference profile is characterized by a steep decline across the first 200 PV, and the bulk of the injected scale inhibitor is returned during this back flow period.

The inhibitor B7 profile provides the highest residual average plateau phase RSI return concentration at approximately 47 ppm to 57 ppm for 2,000 PV coreflood back flow.

The FeS inhibitor variant A6 provided approximately 30 ppm RSI for 2,000 PV, however, there was a peculiar increase in RSI (or ICP sulfur) across the last 400 PV of the plateau phase profile, suggesting contribution from another sulfur containing source. It is believed that the additional sulfur detected originated from calcium sulfate ($CaSO_4$) stringers within the outcrop core plug, and this was confirmed via ion exchange chromatographic analysis identification of free sulfate ion in selected coreflood eluate samples.

The C5 inhibitor variant provided the lowest RSI across the working/plateau phase of the simulated squeeze treatment at approximately 21 ppm for the 1,000 PV test period (the coreflood experiment was terminated at 1,000 PV). The results suggest that all three scale inhibitors show useful retention and release characteristics under simulated field application conditions.

Initial RSI Profile

Figure 5 presents the RSI decay profiles across the initial 10 PV back flow period for all three candidate FeS squeeze scale inhibitors A6, B7, and C5.

All inhibitors showed significant retention within the chalk test core material as demonstrated by the

Table 5 *The coreflood treatment sequence.*

(RT = room temp, CP = confining pressure, BP = back pressure, FWD = forward (production direction from reservoir to wellbore, REV = reverse (direction of flow/injection from wellbore into the reservoir).

	Action	Medium	Measure	T (°C)	P (psi)	Direction
1	Clean core plug, dry	N_2	K_{N2}/ϕ	RT	1,500	—
2	Evacuate N_2 from plug and brine saturate	FW		RT	1,500	—
3	Load into coreholder and apply CP and BP	— —	— —	RT RT	1,500 CP 500 BP	— —
4	Flow brine through core at 4 mL/min and increase oven from room to test temp	FW	ΔP	143	1,500 CP 500 BP	**FWD**
5	Flow oil through core at 4 mL/min	Isopar™	ΔP K_o at S_{wi}	143	1,500 CP 500 BP	**FWD**
6	Flow brine through core at 4 mL/min	FW	ΔP K_W at S_{or}	143	1,500 CP 500 BP	**FWD**
7	Flow 5 PV (brine + 50 ppm Li tracer) at 4 mL/min	FW + Li	ΔP PV	143	1,500 CP 500 BP	**FWD**
8	Flow 5 PV brine at 4 mL/min	FW	ΔP	143	1,500 CP 500 BP	**FWD**
9	**Maintreatment Slug Application:** 5 PV 1.5% inhibitor in 6% NaCl at 4 mL/min	Scale Inhibitor Pill	ΔP	143	1,500 CP 500 BP	**REV**
10	**Shut-in core:** To soak for 24 hours	—	ΔP	143	1,500 CP 500 BP	—
11	**Back Production Phase:** Flow brine at 4 mL/min (for 1,000 – 2,000 PV)	FW	ΔP	143	1,500 CP 500 BP	**FWD**
12	Flow oil through core at 4 mL/min	Isopar™	ΔP K_o at S_{wi}	143	1,500 CP 500 BP	**FWD**
13	Flow brine through core at 4 mL/min	FW	ΔP K_W at S_{or}	143	1,500 CP 500 BP	**FWD**

Table 6 *The coreflood brine composition used in the test.*

Salt Type	Test Brine (g/L)
NaCl	637.21
$CaCl_2.2H_2O$	322.79
$MgCl_2.6H_2O$	39.48

highest RSI values determined being approximately one-fifth of the input scale inhibitor concentration.

Post-Coreflood Core Analysis

After completion of the coreflood back flow period and final oil and water permeabilities, the coreflood apparatus was cooled slowly to reservoir temperature while brine was passed through the core. After room temperature equilibration, the outcrop core pieces were recovered from the core holder and examined via high frequency computerized tomography (HFCT).

Figures 6, 7, and 8 are the HFCT scans of the A6, B7, and C5 coreflood cores, respectively. These HFCT scans span across the entire core length and captures micro-section images from top to bottom. Viewing the collected micro-section image series clearly shows the internal grain structure of the core plug across its entire length, and the technique can also be used to identify core faults or other internal irregularities or unusual solids developments in the core.

Each image set presents a simple 2D HFCT snapshot of the coreflood core plug top cross-sectional area (left) and a longtitudinal view of the plug (right).

HFCT/Inhibitor A6 Core

Figure 6 presents the HFCT image of the core plug used in the coreflood for inhibitor variant A6. When viewing the entire 3D image set, the micro cross-sectional scans showed very little evidence of any internal core irregularities — fractures, cracks or vugs — or unusual solids development (typified by bright white spotting or streaking on the HRCT image).

This was an unexpected as the A6 RSI coreflood profile showed an unusual increase in the latter stage of the flood flow back from approximately 1,600 PV

Fig. 4 *The RSI decay profile showing the "plateau" or the useful "working" phase.*

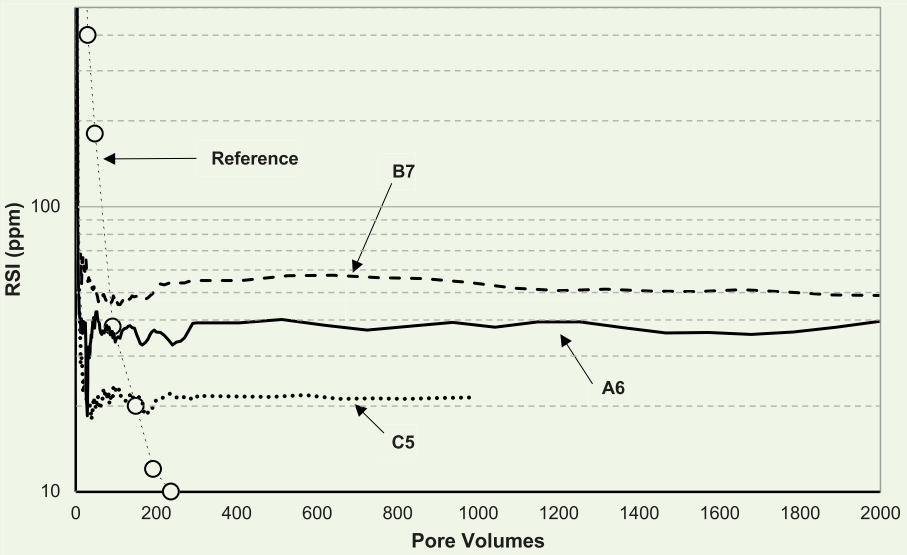

Fig. 5 *The expanded view of the RSI decay profiles across the initial 10 PV back flow period for all three candidate FeS squeeze scale inhibitors.*

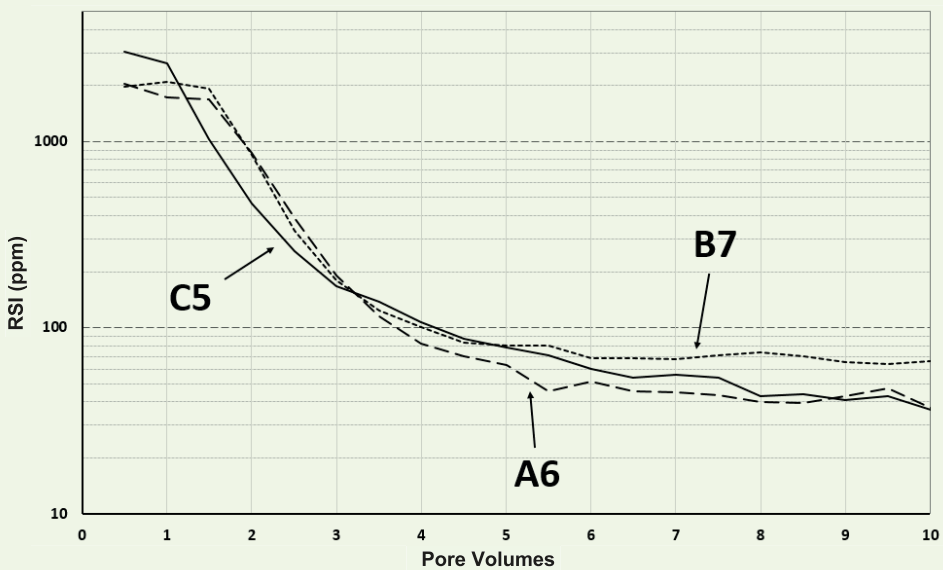

onwards, believed to be due to sulfate ion leaching from $CaSO_4$ deposits within the field analogous chalk outcrop core.

HFCT/Inhibitor B7 Core

Figure 7 presents the HFCT image set taken from the core plug used to coreflood assess inhibitor variant B7. The HFCT identified significant mineral or deposit development across the entire length of the core. The accumulations may be either calcium inhibitor precipitate or $CaSO_4$ minerals within the core. There are additional deposits spotted at other points within the plug.

HFCT/Inhibitor C5 Core

Figure 8 presents the HFCT scan results for the polymeric FeS inhibitor variant C5 coreflood core. The images clearly shows evidence of fracturing within the core body and also the presence of sporadic white deposits located toward one end of the core plug.

It is unknown whether the fracture developed as a result of the coreflood experiment or was there at the

Fig. 6 The HFCT scan of the A6 coreflood core.

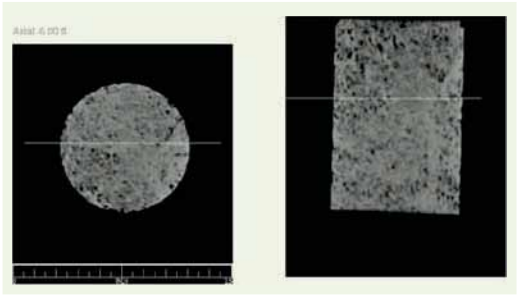

Fig. 7 The HFCT scan of the B7 coreflood core.

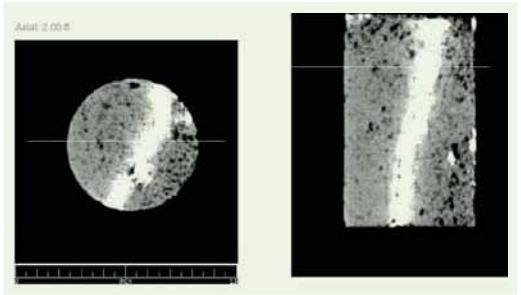

Fig. 8 The HFCT scan of the C5 coreflood core.

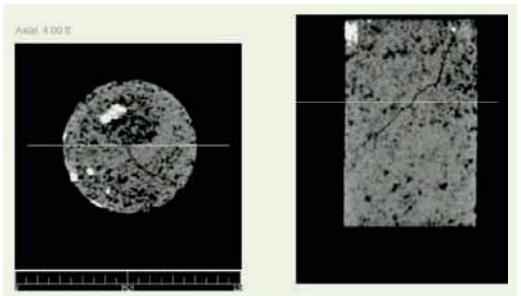

beginning. It is also unclear whether the premature termination of the coreflood experiment was due to the fracture development or some other cause.

Coreflood Summary

All three polymeric squeezable FeS inhibitor variants A6, B7, and C5, generated significant and useful coreflood return profiles under simulated field application conditions of high temperature, high calcium ion, and high TDS brine in chalk outcrop field core analogues. All demonstrated their adsorption and desorption capabilities under simulated field squeeze application conditions.

The formation damage impact assessment performed during the floods provided the necessary performance data allowing discrimination between the three candidate squeeze scale inhibitors. Permeability assessment for both oil and brine transmissibility performed both before and after scale inhibitor application showed that the new variant A6 was the best performing FeS squeeze scale inhibitor, closely followed by variant B7. Both the A6 and B7 coreflood permeability assessments showed very little significant formation damage impact on fluid transmissibility through squeeze application of the chemicals into the chalk outcrop cores.

Inhibitor variant C5 was ranked last in the coreflood series as permeability evaluations performed during the coreflood experiment identified significant impact of chemical application on both oil and brine transmission ability.

Conclusions

The synthesis program achieved its goal in reconstructing an existing polymeric sulfide scale inhibitor and imbuing it with the capability and characteristics sufficient to promote it for FeS scale squeeze application in high temperature, high calcium ion, and high TDS brine chalk well scenarios.

Use of industry standard scale inhibitor compatibility and performance tests assisted in finding the best performing FeS scale inhibitor candidates. Additionally, introduction of state-of-the-art automated high throughput experimentation applied to static adsorption testing assisted in the rapid generation of "ranking" data from the > 100 new polymeric FeS inhibitor chemical variants created and tested.

The coreflood series provided an excellent technique for final discrimination between the top three squeeze scale inhibitor candidates with formation damage assessment providing clear evidence of the suitability of each candidate for squeeze application in simulated field application conditions using field analogous outcrop chalk.

Development product A6 was identified as the best candidate via its minimal impact on the apparent core permeability when deployed in a squeeze treatment into outcrop chalk core under simulated reservoir application conditions.

The polymeric squeezable FeS scale inhibitor A6 is recommended as the best candidate for field deployment.

Acknowledgments

This article was prepared for presentation at the SPE International Oil Field Scale Conference and Exhibition, Aberdeen, Scotland, U.K., June 24-25, 2020.

The authors would like to thank Marjery Dela Cruz of Woodlands Laboratories, Houston, TX, Margarethe Pfahls of GTI Laboratories, Frankfurt, Germany, and robotics engineers Jake Grace and Naveen Allampally of HTE Laboratory Group, GTI Frankfurt, Geermany, for their technical support.

Nomenclature

1°	primary
2°	secondary
3°	tertiary
4°	quaternary
K_o at S_{wi}	Permeability to oil at residual water saturation
K_w at S_{ro}	Permeability to water (brine) at residual oil saturation
K_{N2}	Permeability to nitrogen (gas)

References

1. Lynn, J.D., Nasr-El-Din, H.A. and Hashem, M.K.: "Iron Phosphonate Stabilized Emulsion and Formation Damage during an Adsorption Squeeze Treatment for Scale Mitigation," SPE paper 73718, presented at the International Symposium and Exhibition on Formation Damage Control, Lafayette, Louisiana, February 20-21, 2002.

2. Tomson, M.B., Kan, A.T., Fu, G., Shen, D., et al.: "Mechanistic Understanding of Rock/Phosphonate Interactions and Effect of Metal Ions on Inhibitor Retention," *SPE Journal*, Vol. 13, Issue 3, September 2008, pp. 325-336.

3. Tahir, M.A., Orme, M., Kidd, S., Hoeth, L.W., et al.: "Selection of Non-damaging Phosphonate-Based Scale Inhibitors for Field Application in a Reservoir Containing Reactive Iron Minerals," SPE paper 174222, presented at the SPE European Formation Damage Conference and Exhibition, Budapest, Hungary, June 3-5, 2015.

4. Okocha, C., Kaiser, A., Underwood, S., Samaniego, W., et al.: "New Generation Squeezable Sulfide Inhibitor Successfully Averts Challenging Sulfide Scale Deposition in Permian Basin," SPE paper 190709, presented at the SPE International Oil Field Scale Conference and Exhibition, Aberdeen, Scotland, U.K., June 20-21, 2018.

5. Alharbi, B., Aljeaban, N., Graham, A. and Sorbie, K.S.: "Iron Sulfide and Zinc Sulfide Inhibition and Scale Inhibitor Consumption," SPE paper 197688, presented at the Abu Dhabi International Petroleum Exibition and Conference, Abu Dhabi, UAE, November 11-14, 2019.

6. Wang, Q., Ajwad, H., Shafai, T. and Lynn, J.D.: "Iron Sulfide Scale Dissolvers: How Effective Are They?" SPE paper 168063, presented at the SPE Saudi Arabia Section Technical Symposium and Exhibition, al-Khobar, Saudi Arabia, May 19-22, 2013.

7. Al-Tammar, J.I., Bonis, M., Choi, H.J. and Al-Salim, Y.: "Saudi Aramco Downhole Corrosion/Scaling Operational Experience and Challenges in HP/HT Gas Condensate Producers," SPE paper 169618, presented at the SPE International Oil Field Corrosion Conference and Exhibition, Aberdeen, Scotland, U.K., May 12-13, 2014.

8. Chen, T., Wang, Q. and Chang, F.: "Understanding the Mechanisms of Iron Sulfide Formation in Sour Gas Wells," paper presented at the 16th Middle East Corrosion Conference and Exhibition, Manama, Kingdom of Bahrain, February 8-11, 2016.

9. Wylde, J.J., Okocha, C., Bluth, M., Savin, A., et al.: "Iron Sulfide Inhibition: Field Application of an Innovative Polymeric Chemical," SPE paper 173730, presented at the International Symposium on Oil Field Chemistry, The Woodlands, Texas, April 13-15, 2015.

10. Baraka-Lokmane, S., Hurtevent, C., Rossiter, M., Bryce, F., et al.: "Design and Performance of Novel Sulfide Nanoparticle Scale Inhibitors for North Sea HP/HT Fields," SPE paper 179866, presented at the SPE International Oil Field Scale Conference and Exhibition, Aberdeen, Scotland, U.K., May 11-12, 2016.

11. Chen, T., Wang, Q., Chang, F. and Aljeaban, N.: "Recent Development and Remaining Challenges of Iron Sulfide Scale Mitigation in Sour Gas Wells," IPTC paper 19315, presented at the International Petroleum Technology Conference, Beijing, China, March 26-28, 2019.

12. Rodgers, P., Lundy, B., Ramachandran, S., Ott, J., et al.: "Multifunctional Chemical for Simultaneous Dissolution of Iron Sulfide, Corrosion Inhibition, and Scale Inhibition," SPE paper 193619, presented at the SPE Internatonal Conference on Oil Field Chemistry, Galveston, Texas, April 8-9, 2019.

13. Todd, M.J., Strachan, C.J., Moir, G. and Goulding, J.: "Development of the Next Generation of Phosphorus Tagged Polymeric Scale Inhibitors," SPE paper 130733, presented at the SPE International Conference on Oil Field Scale, Aberdeen, Scotland, U.K., May 26-27, 2010.

14. Todd, M.J., Thornton, A.R., Wylde, J., Strachan, C.J., et al.: "Phosphorus Functionalized Polymeric Scale Inhibitors, Further Developments and Field Deployment," SPE paper 154135, presented at the SPE International Conference on Oil Field Scale, Aberdeen, Scotland, U.K., May 30-31, 2012.

15. Williams, E., Archibald, M., Selle, O.M., Brandal, Ø., et al.: "Introducing Novel Chemistry for Scale Inhibitor Squeeze Treatments on the Heidrun Field — Challenges Faced and Lessons Learned," SPE paper 179909, presented at the SPE International Oil Field Scale Conference and Exhibition, Aberdeen, Scotland, U.K., May 11-12, 2016.

About the Authors

Lena Petrozziello

M.S. in Chemical Engineering, Provadis University

Lena Petrozziello is a Scientist working in the Global Research Center for Polymers at the Clariant Innovation Center in Frankfurt, Germany. She is developing functional polymers for various fields of application such as oil field or personal care chemicals.

Lena focusses on understanding special polymer designs for fluid and surface modification.

She received her M.S. degree in Chemical Engineering from Provadis University, Frankfurt, Germany.

Lena is a Ph.D. student at the Max Planck Institute for Polymer Research, Mainz, Germany. Her main research interest is about multifunctional polymers for surface modification.

Dr. Christoph Kayser

Ph.D. in Polymer Research, Johannes Gutenberg University

Dr. Christoph Kayser is a Senior Scientist working in the Global Research Center for Polymers at the Clariant Innovation Center in Frankfurt, Germany.

His interests are the development and scaling of specialty polymers for various fields of applications in the oil and gas industry, such as flow assurance products, scale inhibitors, drilling and cementing additives, as well as rheology modifiers for personal care applications, and the development of sustainable polymers.

Before joining the Global Research Center for Polymers six years ago, Christoph headed the application development for well service additives, e.g., drilling, cementing and stimulation additives.

He has published over 40 technical publications and patents.

Christoph received his Diploma in Chemistry from the Johannes Gutenberg University and his Ph.D. degree from the Johannes Gutenberg University with the Max Planck Institute for Polymer Research, Mainz, Germany.

Dr. Cyril Okocha

Ph.D. in Petroleum Engineering, Heriot-Watt University

Dr. Cyril Okocha is a Scientist working at the Clariant Global Innovation and Application Development Center in Houston, Texas.

He primarily works as part of the global innovation team that focuses on the development, enhancement and application of novel oil field chemical technologies.

Cyril's research interests include the development and application of novel chemical application technologies, sulfide scale inhibitor development, scale inhibitor squeeze technology, sour gas production, flow assurance, heavy oil production, water treatment technologies, and production enhancement.

He is the author and coauthor of several Society of Petroleum Engineers (SPE) conference papers and patents.

Cyril has a background in Geochemistry from Newcastle University, Newcastle upon Tyne, U.K. He received his Ph.D. degree in Petroleum Engineering from Heriot-Watt University, Edingburgh, Scotland, U.K.

Dr. Tao Chen

Ph.D. in Chemical Engineering, Heriot-Watt University

Dr. Tao Chen is a Petroleum Engineering Specialist working with the Production Technology Team of Saudi Aramco's Exploration and Petroleum Engineering Center – Advanced Research Center (EXPEC ARC). His interests are production chemistry and flow assurance in the oil and gas industry, specializing in oil field scale management.

Prior to joining Saudi Aramco in 2014, Tao spent more than 15 years on oil field scale management and worked at Clariant, Champion Technologies, Nalco Champion, and LR Senergy in Aberdeen, U.K.

He has published over 90 technical publications about scale management in oil fields.

Tao received both his B.S. and M.S. degrees in Chemical Engineering from Dalian University of Technology, China, and his Ph.D. degree in Chemical Engineering from Heriot-Watt University, Edinburgh, U.K. Tao also received an MBA from Warwick University, Coventry, U.K.

Dr. Qiwei Wang

Ph.D. in Oceanography, Texas A&M University

Dr. Qiwei Wang works in Saudi Aramco's Research & Development Center as a Research Science Consultant. Since joining Saudi Aramco in 2011, he has played a key role in all major scale mitigation activities in companywide operations and led the completion of over 80 projects. Before joining Saudi Aramco, Qiwei worked with Nalco Champion as a R&D Coordinator on flow management and as a Senior Specialist on scale management. He has over 25 years of R&D and technical support experience in oil field production chemistry, scale management, and water treatment.

Qiwei is an active member of the Society of Petroleum Engineers (SPE) and National Association of Corrosion Engineers (NACE). He has organized workshops, served on technical committees, and has chaired several conferences for both organizations.

Qiwei is the recipient of the 2021 NACE Technical Achievement Award.

He has authored and coauthored over 180 publications and 20 U.S. patent applications.

Qiwei received his B.Eng. degree in Chemical Engineering from Taiyuan University of Science and Technology, Taiyuan, China; an M.Eng. degree in Material Sciences from Harbin Institute of Technology, Harbin, China; an M.S. degree in Chemistry from the University of Ryukyus, Okinawa, Japan; and a Ph.D. degree in Oceanography from Texas A&M University, College Station, TX.

A New Insight into Friction Reducer Evaluation for Slick Water Unconventional Fracturing

Prasad B. Karadkar, Mohammed I. Alabdrabalnabi and Dr. Mohammed A. Bataweel

Abstract /

Slick water fracturing has increased over the past couple of decades in the development of shale and tight formations. Friction reducer is the main component of slick water, which reduces drag in the tubular. For a successful and economical slick water hybrid fracturing treatment, selection and optimization of friction reducers play a key role. This article presents a new insight into optimizing the friction reducer using a helical coiled flow loop at high-pressure, high temperature (HPHT) conditions.

Usually, friction pressure is estimated by pumping slick water fracturing fluid through a straight tube and measuring differential pressure across the tube. This required pilot-scale laboratory setup and testing at HPHT is a bit challenging. In this article, a small size piece of equipment, a helical coiled flow loop, was utilized to estimate the friction pressure of a slick water fracturing fluid. Friction reducers can be rigorously tested for degradation because secondary flow resulting from centrifugal forces can be caused by the coil curvature. Correlations for a Darcy friction factor, f_D, as a function of the Reynolds number has been developed for the helical coiled fluid loop in both a laminar and turbulent flow regime.

The present study evaluates different friction reducers in a ¼" internal diameter (ID) smooth helical coiled flow loop. The correlations developed for the f_D was well validated for water with data available from literature. Polyacrylamide-based friction reducers with different concentrations were used in this study. The friction pressure, with and without friction reducers, was compared at different flow rates. The percentage of drag reduction at different polymer concentrations was also evaluated using the helical coiled flow loop. Thermal degradation of friction reducers was evaluated by varying the temperature up to 300 °F.

New correlations to measure friction losses using the helical coiled flow regimes are presented in this article. Reduced drag reduction, due to secondary flow resulting from centrifugal forces in the helical coil, can judge friction reducer more thoroughly than a conventionally used straight tube flow loop.

Introduction

In slick water fracturing, a large volume of water is pumped downhole to create an adequate fracture geometry and conductivity to obtain commercial production[1]. The slick water jobs are generally pumped at a high rate, which causes high friction pressure. Poor friction reduction limits the operational pressure window while performing fracturing treatment.

During hydraulic fracturing treatment, to estimate bottom-hole treatment pressure, the friction pressure needs to be precisely computed for the fracturing fluid[2]. Palisch et al. (2008)[1] reviewed the benefits and concerns with slick water fracturing over conventional cross-linked design and published theories related to slick water fracturing, including fracture width and complexity, proppant transport and settling, and conductivity requirements. For successful and economical slick water fracturing treatment, selection and optimization of friction reducers play a key role.

Frictional pressure in pipes can be reduced by adding small quantities of certain long-chain polymers in water; a phenomenon called drag reduction[3]. Different factors can affect the polymer drag reduction performance such as the polymer type, concentration, shear degradation, and flow geometry. Polyacrylamide-based friction reducers are commonly used to reduce fluid friction within the pipe. Shah et al. (2018)[4] tested anionic and cationic friction reducers, concluding that anionic friction reducers provide better drag reduction characteristics, and that both friction reducers degraded when subjected to high shear rates.

Ibrahim et al. (2016)[5] tested different salt tolerant copolymers of acrylamides for drag reduction and different breakers to break these polymers using ammonium persulfate, sodium persulfate, hydrogen peroxide, and sodium bromate. The mechanism of breaking the polyacrylamide-based friction reducers by oxidative and radical degradation is discussed by Ke et al. (2019)[6]. Kamel (2018)[7] studied the effect of ionic strength on drag reduction characteristics of polymer solution where he tested anionic polyacrylamide copolymers in freshwater, potassium chloride brines, and synthetic seawater having 3.4% total dissolved salt.

Table 1 The kinematic viscosity of various fluids measured at different temperatures.

Temperature (°F)	Water	Slick Water (2 gpt Polymer)	Slick Water (4 gpt Polymer)
68	1.11	3.19	6.63
104	0.85	2.08	4.51
140	0.74	1.62	3.23
176	0.67	1.15	2.11

A straight tube flow loop is widely used to evaluate the performance of slick water for drag reduction characteristics[4, 5]. The American Petroleum Institute is in the process of developing a standard testing procedure for evaluating friction reducers[4]. Currently, different organizations and academic institutions use a straight tube, where water with a polymer solution is pumped at different rates and differential pressure across the tube, and then measured to estimate the friction pressure.

Shah et al. (2018)[4] published testing methodology by comparing different straight tube flow loops with data analysis and correlations for turbulent flow of Newtonian fluids in smooth pipes. It was also reported that drag reduction behavior using a single pass and circulating test was similar. Zhou and Shah (2006)[8] developed a new friction factor correlation for both laminar and turbulent flow of non-Newtonian fluids in coiled tubing (CT). The effect of the pipe's roughness on friction pressure studied by Shah (1989)[2] showed a higher friction as compared to a smooth pipe. The pipe roughness correction factor showed a generalized trend, as it increase with the Reynolds number and decreases with the fluid's apparent viscosity.

A CT flow loop is rarely used for friction analysis in the oil and gas industry[8, 9]. A pressure drop characteristic in helical CTs are widely studied for heat exchanger designs[10-12]. New correlations to measure friction losses using helical coiled flow regimes have been developed to study the performance of friction reducers in slick water fracturing. Friction analysis using a straight tube has certain limitations like restricted tube length, temperature, and pressure limit. In a CT flow loop, reduced drag reduction due to secondary flow from centrifugal forces in helical coil can assist in judging the friction reducer more thoroughly.

As described in this article, small-sized equipment — a smooth helical coiled flow loop — was utilized to estimate the friction pressure of slick water fracturing fluid up to 300 °F and at 2,000 psi. The freshwater data was validated using correlations published in the literature. Correlations for the Darcy friction factor, f_D, as a function of the Reynolds number, has been developed for the helical coiled fluid loop in both a laminar and turbulent flow regime. Friction reducers were rigorously tested for degradation over a period of time. The percentage of the drag reduction with an increasing concentration of polymer in the slick water formulation were also compared.

Experimental Methods

Materials

Slick water was prepared by using freshwater, 2 gal/1,000 gal (gpt) surfactant, 2 gpt clay control agent, and 2 gpt and 4 gpt polyacrylamide-based friction reducer, which measures a 3 cP and 6 cP at 511 1/s shear rate using Fann 35 with R1-B1 rotor-bob combination at 80 °F, respectively.

Viscosity Measurement

To perform friction analysis, the absolute viscosity of water and slick water were measured using a Cannon-Fenske capillary viscometer. Table 1 shows the kinematic viscosity of different fluids measured at different temperatures using a 200-size viscometer. The kinematic viscosity at high temperature, 200 °F and 300 °F, was extrapolated using this data. The density measured using a mass flow controller was utilized to calculate absolute viscosity. The absolute viscosity was used to calculate the Reynolds number for friction analysis.

Friction Measurement Using a Coiled Flow Loop

A circulating loop rheometer having a helical coil, with a 0.25" internal diameter (ID) and a 10 ft long tube, was used in this study to analyze friction behavior of water and slick water at 200 °F and 300 °F.

Figure 1 shows a schematic of the circulating loop

Fig. 1 A schematic of the circulating loop rheometer.

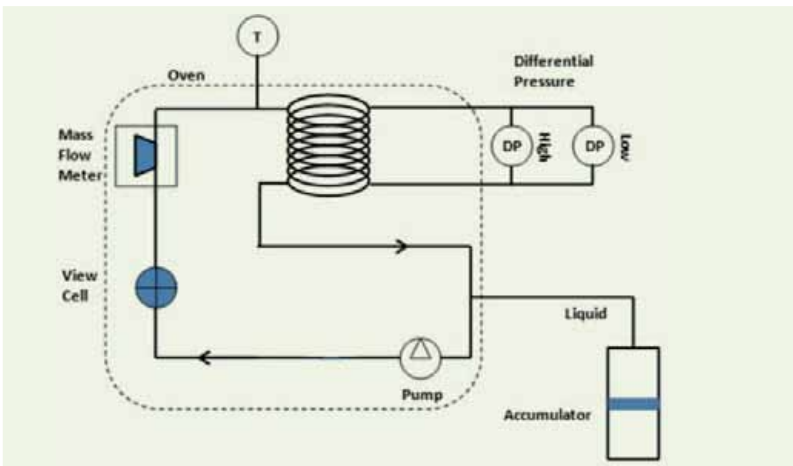

rheometer. The fluid was charged inside the helical coiled flow loop using an accumulator, while the 2,000 psi system pressure was maintained. After temperature equilibration, fluid was circulated at a different rate through the loop and differential pressure across the coil was measured. The differential pressure data was further processed to calculate the friction factor. The apparent viscosity was calculated using a Power-law model to study degradation of slick water under high-pressure, high temperature (HPHT) conditions.

Results and Discussions

Friction Correlations and Validation

Fluid flow in the helical tube has been found in industrial and domestic systems, specifically in the petroleum industry such as well drilling and stimulation operations[13]. A secondary flow of fluid is developed when it flows in a curved structure, resulting in centrifugal forces, creating a significant frictional loss in curved tubes over straight tubes at the same pressure, temperature, and flow rate[11].

The friction factor of a pipe wall can be obtained by measuring the pressure drop along the pipe. The following pressure drop equation is used to measure the friction factor, f_M, which is commonly termed as the Moody friction factor[4]:

$$f_M = \frac{\Delta p\, d_t}{2\,\rho\, U^2 L} \quad (1)$$

where, Δp is friction pressure drop across the tube length, L, dt is the tube diameter, ρ is the density of fluid, and U is the velocity of fluid.

To validate friction analysis correlations using the flow loop described, waterflow tests were conducted at different rates and compared with correlations published in the literature. During our analysis, we found that the f_D fits well with published correlation for water using this experimental setup. The difference between the two friction factors is that the value of the f_D is four times that of the Fanning friction factor[14].

Equation 2 was derived from Eqn. 1 to calculate the f_D, which was utilized throughout this article.

$$f_D = 2\frac{\Delta p\, d_t}{\rho\, U^2 L} \quad (2)$$

Consequently, the flow characteristics in helical coils are considerably different than in straight tubes; while the transition from laminar to turbulent flow happens at higher Reynolds numbers — the transition in straight tubes takes place within a Reynolds numbers of 2,500[10].

The critical Reynolds number in Eqn. 3 was utilized for helical coils to determine the transition of the flow[12].

$$Re_c = 2100\left(1 + 12\sqrt{\delta}\right) \quad (3)$$

In Eqn. 3, δ is the curvature ratio as defined in Eqn. 4:

$$\delta = \frac{d_t}{D_c} \quad (4)$$

where, d_t is the tube's ID and D_c is the helix diameter.

The circulating flow loop used in this study has a d_t of 0.635 cm, a D_c of 32.51 cm, and the L of the tube is 304.8 cm. This estimate curvature ratio, δ, 0.0195, which was utilized to calculate the critical Reynolds number (Re_c), 5,622 for this system. To quantify the magnitude of the secondary flow, a dimensionless number is named as the Dean Number in Eqn. 5 is used specifically to characterize the flow in helical coils:

$$De = \frac{\rho\, U\, dt\sqrt{\delta}}{\mu} \quad (5)$$

where, ρ is the fluid density, U is the fluid velocity, and μ is the absolute viscosity.

The following developed friction factor correlation in Eqn. 6 is a function of the Re and δ, which is the ratio of the tube's ID to the coil's diameter.

$$f_D = C\, Re^m\, \delta^n \quad (6)$$

Since δ in our case is a constant value, we will simplify Eqn. 7 to make it as follows:

$$f_D = C'\, Re^m \quad (7)$$

where $C' = C \times \delta^n$. The friction data generated by using a helical coiled flow loop was well fitted in Eqn. 7 for both the laminar flow and the turbulent flow regime to be discussed next.

Laminar Flow

Manlapaz and Churchill (1980)[15] proposed the following correlation in Eqn. 8 to calculate the friction factor within the laminar flow regime ($Re < Re_c$) in a helical coil:

$$f_{cl} = f_{sl}\left[1 + \left(1 + \frac{\delta}{3}\right)^2 \frac{De}{88.33}\right]^{0.5} \quad (8)$$

where f_{cl} is the friction factor for the helical tube, and f_{sl} is defined in Eqn. 9 as the friction factor for the smooth straight tube, both at laminar flow[16].

$$f_{sl} = \frac{64}{Re} \quad (9)$$

Turbulent Flow

For the smooth tube where $Re > Re_c$, the helical coil friction factor is calculated using the correlation[12] as follows in Eqn. 10:

$$f_{ct} = 4\, x\, 0.084\, Re^{-0.2}\delta^{0.1} \quad (10)$$

where f_{ct} is the friction factor for a helical tube at turbulent flow. We have multiplied the correlation by four to convert it to a f_D.

Figure 2 shows the comparison of the f_D of water calculated from Eqn. 2 with correlations published for both a laminar and turbulent region. We have utilized Microsoft Excel to generate a Power Law fitting curve from the trend line options by plotting the f_D vs. Reynolds number, Re.

Equation 8 was used to calculate the friction factor within the laminar flow regime ($Re < Re_c$) in a helical coiled flow loop. The experimental data fits well with this correlation with an average error of 12%. In a turbulent flow regime, for a smooth tube where $Re > Re_c$, the helical coil friction factor was calculated using the correlation[12] as follows in Eqn. 10. The experimental data fits very well with this correlation with an average error of 2.5%. The friction factor correlations for water developed using Eqn. 7 using a flow loop system are $f = 5.0198\mathrm{Re}^{-0.5779}$ and $f = 0.1231\mathrm{Re}^{-0.1366}$, for a laminar

Fig. 2 The f_D data of water at 200 °F and 2,000 psi.

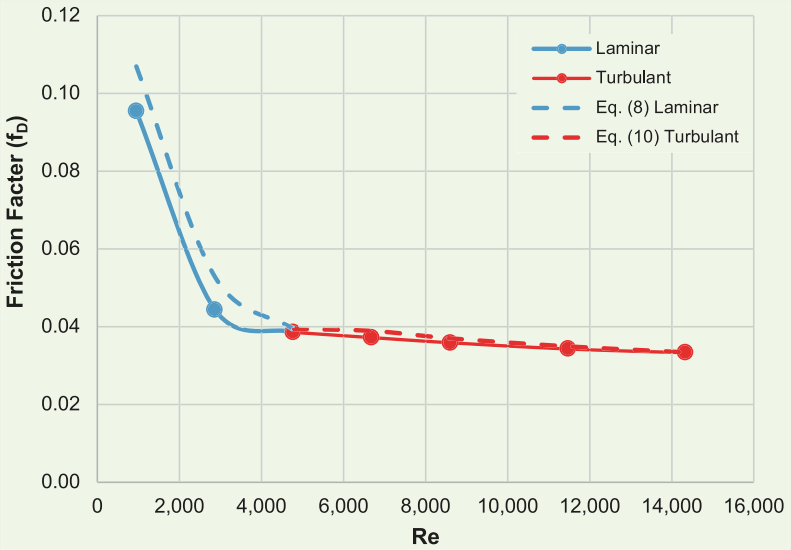

flow regime and turbulent flow regime, respectively. The value of m, -0.5779 and -0.1366, is close to an exponent of Eqn. 8 and Eqn. 10. This validates Eqn. 2 to estimate the f_D for unknown fluids using a helical coiled flow loop.

Friction Analysis of Slick Water

The performance of slick water fluid was rigorously evaluated using a helical coiled flow loop. Two concentrations of a polyacrylamide-based friction reducer, 2 gpt and 4 gpt, was evaluated at 300 °F and 2,000 psi and compared with freshwater.

Figure 3 shows the f_D calculated using Eqn. 2 from differential pressure across a helical coil flow loop at different flow rates. The friction factor of water was decreased with an increase in polymer concentration. At 300 °F and 2,000 psi, HPHT, an accurate viscosity measurement is quite challenging. To measure absolute viscosity of water and slick water at such conditions, viscosity at a lower shear rate was measured using the Power Law Model and then viscosity was extrapolated backward to zero shear rate.

Equations 11 to 13 describe the correlation for the Power Law Model[17]:

$$Apparent\ Viscosity = \frac{Shear\ Stress}{Shear\ Rate} \quad (11)$$

Fig. 3 The f_D data for water and slick water at 300 °F and 2,000 psi.

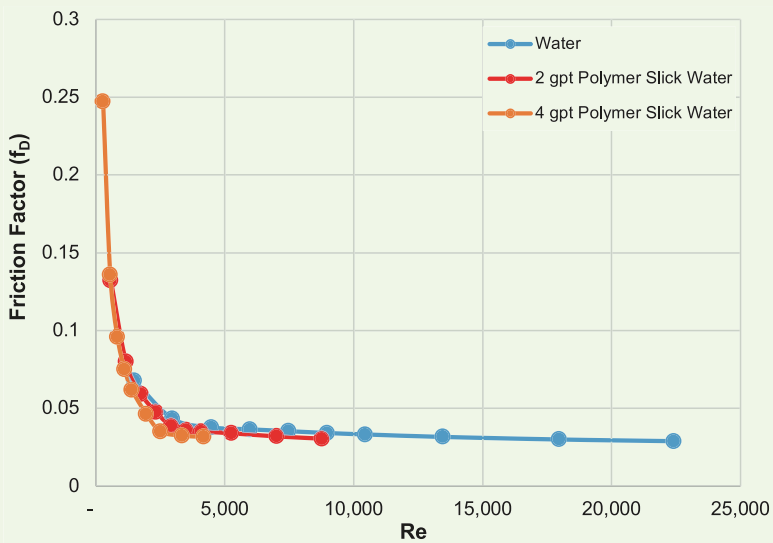

$$Shear\ rate = \frac{8\,U}{d_t} \quad (12)$$

$$Shear\ stress = \frac{d_t\,\Delta P}{4\,L} \quad (13)$$

Table 2 shows the zero shear viscosity of water and 2 gpt and 4 gpt slick water compared with the friction correlation constant derived from Eqn. 7. As expected, an increase in viscosity was noticed after adding 2 gpt and 4 gpt polymer in water in preparing the slick water. Both correlation constants, *C'* and *m*, increased with an increase in viscosity of the fluid in the Laminar regime, while in the turbulent region, these constants varied in a narrow range. With an increase in viscosity, the f_D curves shifted toward the laminar regime, which shows the effectiveness of friction reducers.

Drag Reduction

Shah and Zhou (2003)[3] defined drag reduction using the following correlation:

$$D_R = 1 - \left(\frac{dp}{dl}\right)_p / \left(\frac{dp}{dl}\right)_s \quad (14)$$

where $(dp/dl)p$ and $(dp/dl)s$ are frictional pressure gradients of a polymer solution and the solvent under the same flow conditions. It was further derived in Eqn. 15 by assuming the density of the polymer solution is the same as the density of the solvent:

$$D_R = 1 - f_p/f_s \quad (15)$$

where, f_p is the friction factor of the polymer solution and f_s is the friction factor of water.

Figure 4 shows the percentage of drag reduction by increasing the polymer concentration in a slick water formulation from 2 gpt to 4 gpt at 300 °F and 2,000 psi. The percentage of drag reduction was varied in a narrow range — 10% using a 2 gpt polymer slick water formulation. The percentage of drag reduction with a 4 gpt polymer slick water formulation showed an increased drag reduction with the Reynolds number.

Degradation of Friction Reducer

Friction reducers can be rigorously evaluated at HPHT conditions by using the flow looped presented in this article. The secondary flow resulted by centrifugal forces caused by the coil curvature test friction reducer.

Table 2 *The f_D correlation constants from Eqn. 7 at 300 °F and 2,000 psi.*

	Water		2 gpt Polymer Slick Water		4 gpt Polymer Slick Water	
	Laminar	Turbulent	Laminar	Turbulent	Laminar	Turbulent
C'	3.44800	0.16220	12.036	0.1706	20.678	—
m	-0.5420	-0.1720	-0.711	-0.189	-0.787	—
Viscosity (cP)	0.312		0.802		1.676	

Fig. 4 *The percentage of the drag reduction by increasing the polymer concentration at 300 °F and 2,000 psi.*

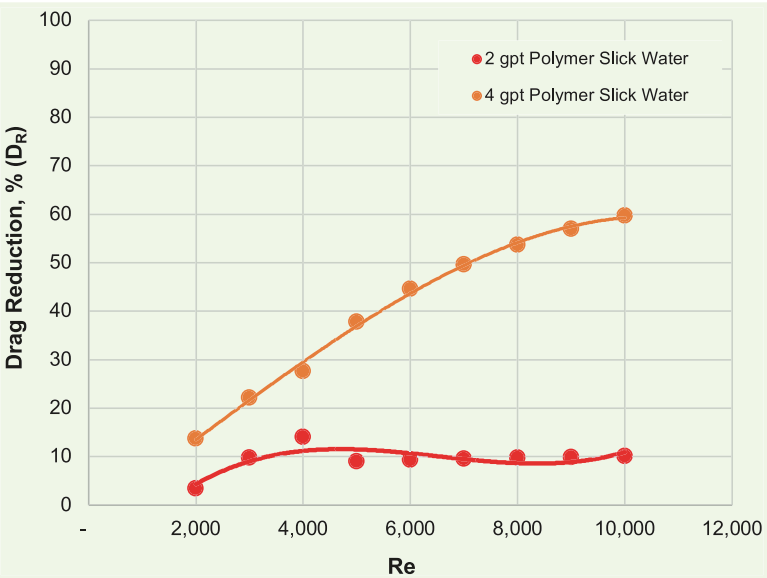

Fig. 5 *The apparent viscosity degradation of 2 gpt and 4 gpt polymer slick water compared with water at 700 1/s, 300 °F, and 2,000 psi.*

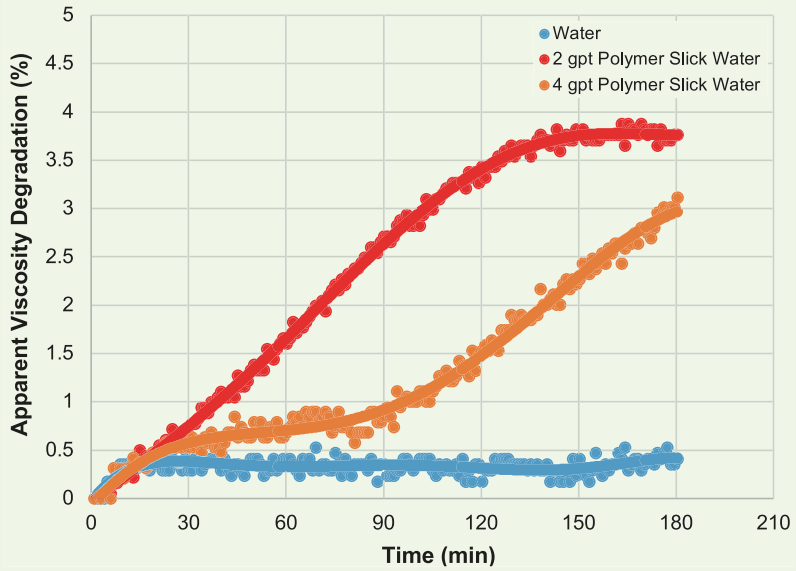

A conventional straight tube limits the length of investigation; while with helical coil geometry, longer lengths can be used for better evaluation. Another limitation of conventional friction loops is HPHT conditions; they limit analysis of the friction reducer under a robust environment.

Figure 5 shows the percentage of viscosity degradation of 2 gpt and 4 gpt polymer slick water compared with water. This shows thermal degradation of the polymer. All three fluids were tested in similar test conditions that were constant, a shear rate of 700 1/s, 300 °F, and 2,000 psi for 3 hours. After temperature equilibration, water as a baseline was almost constant with time. The slick water, having a 2 gpt polymer concentration, degraded up to 3.75% in 3 hours. While increasing the polymer concentration, the 4 gpt polymer slick water showed 1% degradation in 90 minutes and then increased to 3% in 3 hours.

Conclusions

New correlations to measure frictional losses using a smooth helical coiled flow loop was developed to evaluate friction reducer performance in slick water hydraulic fracturing. This flow loop was used at HPHT conditions, 300 °F and 2,000 psi to generate data for drag reduction. Based on these investigations, the following conclusions can be drawn:

- The f_D for freshwater correlated well with equations available from literature for both laminar and turbulent regimes. This validated a helical coiled flow loop for friction analysis.
- The f_D decreases with an increase in polymer concentration in a slick water formulation. The percentage of drag reduction increased with an increase in polymer concentration.
- The secondary flow resulted by centrifugal forces caused by the coil curvature showed more degradation in viscosity of the 2 gpt polymer slick water as compared to the 4 gpt polymer slick water under HPHT conditions.

Acknowledgments

This article was presented at the Offshore Technology Conference Asia, Kuala Lumpur, Malaysia, November 3, 2020.

References

1. Palisch, T.T., Vincent, M.C. and Handren, P.J.: "Slickwater Fracturing: Food for Thought," SPE paper 115766, presented at the SPE Annual Technical Conference and Exhibition, Denver, Colorado, September 21-24, 2008.
2. Shah, S.N.: "Effects of Pipe Roughness on Friction Pressures of Fracturing Fluids," SPE paper 18821, presented at the SPE Production Operations Symposium, Oklahoma City, Oklahoma, March 13-14, 1989.
3. Shah, S.N. and Zhou, Y.: "An Experimental Study of Drag Reduction of Polymer Solutions in Coiled Tubing," *SPE Production and Facilities*, Vol. 18, Issue 4, November 2003, pp. 280-287.
4. Shah, S.N., Asadi, M., Wheeler, R., Brannon, H., et al.: "Methodology for Evaluating Drag Reduction Characteristics of Friction Reducer," SPE paper 189537, presented at the SPE International Conference and Exhibition on Formation Damage Control, Lafayette, Louisiana, February 7-9, 2018.
5. Ibrahim, A.F., Nasr-El-Din, H.A., Rabie, A., Lin, G., et al.: "A New Friction Reducing Agent for Slickwater Fracturing Treatments," SPE paper 180245, presented at the SPE Low Perm Symposium, Denver, Colorado, May 5-6, 2016.
6. Ke, L., Sun, H., Weston, M., Wallbaum, J., et al.: "Understanding the Mechanism of Breaking Polyacrylamide Friction Reducers," SPE paper 196107, presented at the SPE

Annual Technical Conference and Exhibition, Calgary, Alberta, Canada, September 30-October 2, 2019.

7. Kamel, A.H.: "Experimental Investigation of the Ionic Strength Effects on Drag Reduction Characteristics of Polymer Solutions — Part I: Straight Tubing," OTC paper 28636, presented at the Offshore Technology Conference, Houston, Texas, April 30-May 3, 2018.

8. Zhou, Y. and Shah, S.N.: "New Friction Factor Correlations of Non-Newtonian Fluid Flow in Coiled Tubing," *SPE Drilling and Completion*, Vol. 21, Issue 1, March 2006, pp. 68-76.

9. Ahmed Kamel, A.H. and Shaqlaih, A.S.: "Friction Pressure Losses of Fluids Flowing in Circular Conduits," OTC paper 22884, presented at the Offshore Technology Conference, Houston, Texas, April 30-May 3, 2012.

10. Fsadni, A.M., Whitty, J.P.M. and Stables, M.A.: "A Brief Review on Frictional Pressure Drop Reduction Studies for Laminar and Turbulent Flow in Helically Coiled Tubes," *Applied Thermal Engineering*, Vol. 109, Part A, October 2016, pp. 334-343.

11. Krishna, B.: "Prediction of Pressure Drop in Helical Coil with Single Phase Flow of Non-Newtonian Fluid," *International Journal of Applied Research in Mechanical Engineering*, Vol. 2, Issue 1, 2012, pp. 31-36.

12. Srinivasan, P.S., Nandapurkar, S.S. and Holland, F.A.: "Friction Factor for Coils," *Transactions of the Institution of Chemical Engineers*, Vol. 48, 1970, pp. 156-161.

13. Shatat, M.M.E., Yanase, S., Takami, T. and Hyakutake, T.: "Drag Reduction Effects of Micro-Bubbles in Straight and Helical Pipes," *Journal of Fluid Science and Technology*, Vol. 4, Issue 1, January 2009, pp. 156-167.

14. Manning, F.S. and Thompson, R.E.: *Oilfield Processing of Petroleum. Vol. 1: Natural Gas*, PennWell Books, 1991, 408 p.

15. Manlapaz, R.L. and Churchill, S.W.: "Fully Developed Laminar Flow in a Helically Coiled Tube of Finite Pitch," *Chemical Engineering Communications*, Vol. 7, Issues 1-3, 1980, pp. 57-78.

16. Mishra, P. and Gupta, S.N.: "Momentum Transfer in Curved Pipes. 1. Newtonian Fluids," *Industrial and Engineering Chemistry Process Design and Development*, Vol. 18, Issue 1, 1979, pp. 130-137.

17. Keck, R.G.: "The Effects of Viscoelasticity on Friction Pressure of Fracturing Fluids," SPE paper 21860, presented at the Rocky Mountain Regional Meeting and Low Permeability Reservoirs Symposium, Denver, Colorado, April 15-17, 1991.

About the Authors

Prasad B. Karadkar

M.S. in Chemical Engineering, Nagpur University

Prasad B. Karadkar is a Petroleum Engineer with the Production Technology Team of Saudi Aramco's Exploration and Petroleum Engineering Center – Advanced Research Center (EXPEC ARC). Prior to joining Saudi Aramco in April 2016, he worked as a Senior Technical Professional for Halliburton for 9 years. Prasad's areas of expertise include developing new fluid systems in the area of hydraulic fracturing, acidizing, diversion, and water shutoff.

He has authored and coauthored 16 papers, published one patent, and has several patent applications in process.

In 2003, Prasad received his B.S. degree in Chemical Engineering from Shivaji University, Kolhapur, India, and in 2007, he received his M.S. degree in Chemical Engineering from Nagpur University, Nagpur, India.

Mohammed I. Alabdrabalnabi

B.S. in Chemical Engineering, King Fahd University of Petroleum and Minerals

Mohammed I. Alabdrabalnabi joined Saudi Aramco in August 2015 as a Petroleum Engineer with the Production Technology Division of Saudi Aramco's Exploration and Petroleum Engineering Center – Advanced Research Center (EXPEC ARC).

His research interests include fracturing fluids, water shutoff fluid systems, sand control, and condensate banking.

Mohammed received his B.S. degree in Chemical Engineering from King Fahd University of Petroleum and Minerals (KFUPM), Dhahran, Saudi Arabia.

Dr. Mohammed A. Bataweel

Ph.D. in Petroleum Engineering, Texas A&M University

Dr. Mohammed A. Bataweel is a Champion for the Smart Fluid focus area in the Production Technology Division of Saudi Aramco's Exploration and Petroleum Engineering Center – Advanced Research Center (EXPEC ARC). Mohammed has led his team in the development and deployment of several in-house technologies in Saudi Aramco fields. Throughout his career, he has represented his department on several field development, asset, and multidisciplinary teams.

Mohammed's research interests include formation damage due to drilling and completion fluids, investigation and mitigation of injectivity decline, conformance control, sand production prediction, special core analysis, chemical enhanced oil recovery, productivity enhancement technologies, visualization of fluid flow in porous media, and oil field chemicals.

He is an active member of the Society of Petroleum Engineers (SPE) where he has served on several conferences. Mohammed initiated and co-chaired several SPE advanced technical workshop series in the region. He has published more than 40 SPE papers in local and international conferences and refereed journals.

Mohammed received his B.S. degree in Mechanical Engineering from King Fahd University of Petroleum and Minerals (KFUPM), Dhahran, Saudi Arabia, and his M.S. degree in Petroleum Engineering from Harriot-Watt University, Edinburgh, U.K. Mohammed received his Ph.D. degree in Petroleum Engineering from Texas A&M University, College Station, TX.

Improving the Operation of Split Flow Sulfur Recovery Plants with Membrane Technology

Dr. Milind M. Vaidya, Dr. Sebastien A. Duval, Dr. Feras Hamad, John P. O'Connell, Ghulam Shabbir, Ahmed J. Al-Talib, Dr. Ahmad A. Bahamdan and Dr. Faisal D. Al-Otaibi

Abstract /

Sulfur recovery units (SRUs) are used in gas plants and refineries to convert hydrogen sulfide (H_2S) to elemental sulfur. H_2S occurs naturally in natural gas or is formed as a byproduct in refinery and/or petrochemical processing systems, e.g., hydro-treatment. H_2S is highly toxic, thereby requiring removal from the gas stream. Efficient processing of H_2S and other sulfur containing compounds is vital in reducing emissions to meet increasingly stringent environmental regulations. In a SRU, an acid gas feed stream containing H_2S and a source of oxygen, such as air, are fed to a free-flame furnace, followed by multiple catalytic stages to convert most of the H_2S into elemental sulfur.

This article introduces a new approach for the operation of split flow sulfur recovery plants. For lean acid gas, i.e., low H_2S content gas, only a fraction of the acid gas is sent to the reaction furnace of the modified claus SRU. The remaining acid gas, or bypassed feed, is merged with the outlet of the reaction furnace stream, downstream of the waste heat recovery unit and upstream of the first sulfur condenser.

One benefit of bypassing the reaction furnace is the reduction of the formation of carbonyl sulfide and carbon disulfide within the furnace, due to the high concentration of carbon dioxide (CO_2) and kinetic limitation. A shortcoming, however, is that a fraction of the heavy hydrocarbons, i.e., benzene, toluene, and xylene (BTX), are not destroyed in the furnace reactor as a result of the bypass. BTX can deposit and rapidly deactivate the catalytic beds. To mitigate this risk, an activated carbon bed is installed to trap these hydrocarbons upstream of the catalyst bed. The cyclical nature of the operation of the activated carbon bed (adsorption, regeneration) as well as the risk inherent to the replacement of the contaminated beds call for an alternative approach.

In this article, the improvements discussed relate to the use of membranes that separate BTX along with H_2S. The H_2S-rich and BTEX-rich stream is routed to the reaction furnace, unloading the activated carbon bed and thereby improving the operation of the sulfur recovery plant. An associated benefit is the possibility to route a larger fraction of the feed H_2S within the reaction furnace such that the risk of O_2 breakthrough to the catalyst bed is reduced while operating at a large bypass fraction.

A series of process simulations with different acid gas compositions and different membrane properties were evaluated to determine the impact of membrane selectivity on the acid gas composition sent to the reaction furnace.

The results show a significant reduction of BTX and other hydrocarbons sent to catalytic converters and an acid gas enrichment with a significant increase in H_2S content in the acid gas feeding the reaction furnace. The ability of the membrane to concentrate BTX along with H_2S can lead to a new operating philosophy for lean acid gas sulfur recovery plants.

Introduction

The focus of this article is to share new options offered by membrane technology to improve the operation of a split flow sulfur recovery plant affected by the presence of benzene, toluene, and xylene (BTX) in the acid gas.

General Overview of Gas Plant

Raw natural gas is subjected to several processes before sales gas quality is met[1-3]. Figure 1 displays the most frequent processes found in a gas plant, which may include steps to remove condensate and liquid water that originated from the reservoir or upstream facilities, to remove acid gases (hydrogen sulfide (H_2S) and/or carbon dioxide (CO_2)), to reduce water content, to recover heavy hydrocarbons and finally to reduce the inert nitrogen content in the treated gas if required.

Acid Gas Removal

The acid gas removal step, or gas sweetening, is traditionally performed by contacting the raw natural gas

Fig. 1 *A schematic of the different processes found in a typical gas plant.*

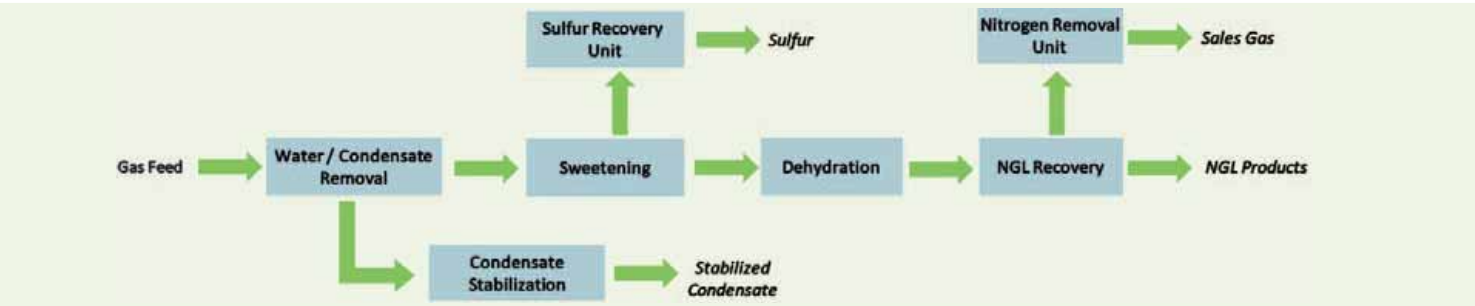

with an aqueous alkanolamine (referred to as amine) solution. In a gas-liquid contactor, H_2S and CO_2 are absorbed by the amine, and depending on the process, partially or completely removed from the gas. The amine is regenerated at a high temperature, approximately 120 °C, by releasing the acid gases.

The design of the gas sweetening unit and the selection of the type of amine for a given application can be found in many references[4]. It should be noted that, along with the acid gases, some hydrocarbons are co-absorbed since the amine also acts as a physical solvent for hydrocarbons. Before the regeneration step, the amine is sent to a flash vessel to remove the bulk of the dissolved hydrocarbons; however, a fraction of heavy hydrocarbons, such as BTX, are difficult to flash out. Consequently, the remaining hydrocarbons are stripped along with acid gases during the amine regeneration and sent to the sulfur recovery unit (SRU)[5].

SRU

A SRU converts H_2S into elemental sulfur. The most prevalent sulfur recovery process is based on the Claus reaction[6], where H_2S undergoes a partial oxidation, the oxidant being dioxygen from air:

$$3H_2S + \frac{3}{2}O_2 \rightarrow \frac{3}{x}S_x + 3H_2O \qquad \text{(Claus reaction)}$$

Originally, the reaction was conducted in one step over a catalyst bed, but the reaction rate was low, and recovery lower than 90%. In the late 1930s, a major modification took place to improve the sulfur recovery by adding a thermal reaction, which is a free-flame oxidation of one-third of the H_2S into sulfur dioxide (SO_2). Downstream, the reaction furnace produced sulfur is collected, and in the subsequent catalytic stages, residual SO_2 and H_2S react to form elemental sulfur.

$$3H_2S + \frac{3}{2}O_2 \rightarrow SO_2 + 2H_2S + H_2O$$
(Modified Claus: reaction furnace)

$$SO_2 + 2H_2S \rightarrow \frac{3}{x}S_x + 2H_2O$$
(Modified Claus: catalytic stages)

In addition to an improvement of the conversion rate, a large amount of heat can be recovered during the cooling of the gas exiting the reaction furnace. Several converters in a series, along with elemental sulfur condensers between each converter can lead to sulfur recovery above 97%. Depending of the local regulatory emission requirement, tail gas treatment is often also implemented to achieve a 99.9+% recovery.

There are different configurations for sulfur recovery plants. The selection for the most appropriate configuration/mode of operation for SRUs can be found in numerous references[6]. Two different designs are shown in Figs. 2a and 2b. In both designs, the sulfur recovery plant is equipped with a reaction furnace and catalytic stages, however:

- In the straight through configuration, the whole acid gas stream is routed to the reaction furnace and then enters the catalytic stages.
- In split flow configuration, only a part of the acid gas is routed to the reaction furnace and the balance is injected upstream the first catalytic stage.

A rule of thumb is that for a H_2S concentration above 55% in the acid gas, a straight through configuration is normally selected, because the temperature reached in the reaction furnace is high enough to destroy contaminants. For a lower H_2S concentration — between 20% and 55% — the large amount of inert gas would prevent the reaction furnace from reaching the desired temperature, and therefore, a split flow configuration is preferable.

Alternatives to the split flow are oxygen enrichment, acid gas enrichment and/or fuel gas co-firing. All options are commercially available, but are either expensive or have an excessive CO_2 footprint. For a H_2S concentration between 10% and 20%, a split flow configuration with a preheating of the streams is normally designed. The overall sulfur recovery process, including reaction furnace, condensers and catalytic stages, can be modeled with commercial simulators, e.g., Sulsim®, that can predict the heat and mass balance expected throughout the sulfur recovery process.

This article endeavors to illustrate the potential improvement with membrane technology for the split flow configuration operation of a sulfur recovery plant, e.g., for lean acid gas or when the H_2S content is between 20% and 55% in the acid gas.

Fig. 2 *(a) Straight through sulfur recovery plant configuration, and (b) split flow sulfur recovery plant configuration.*

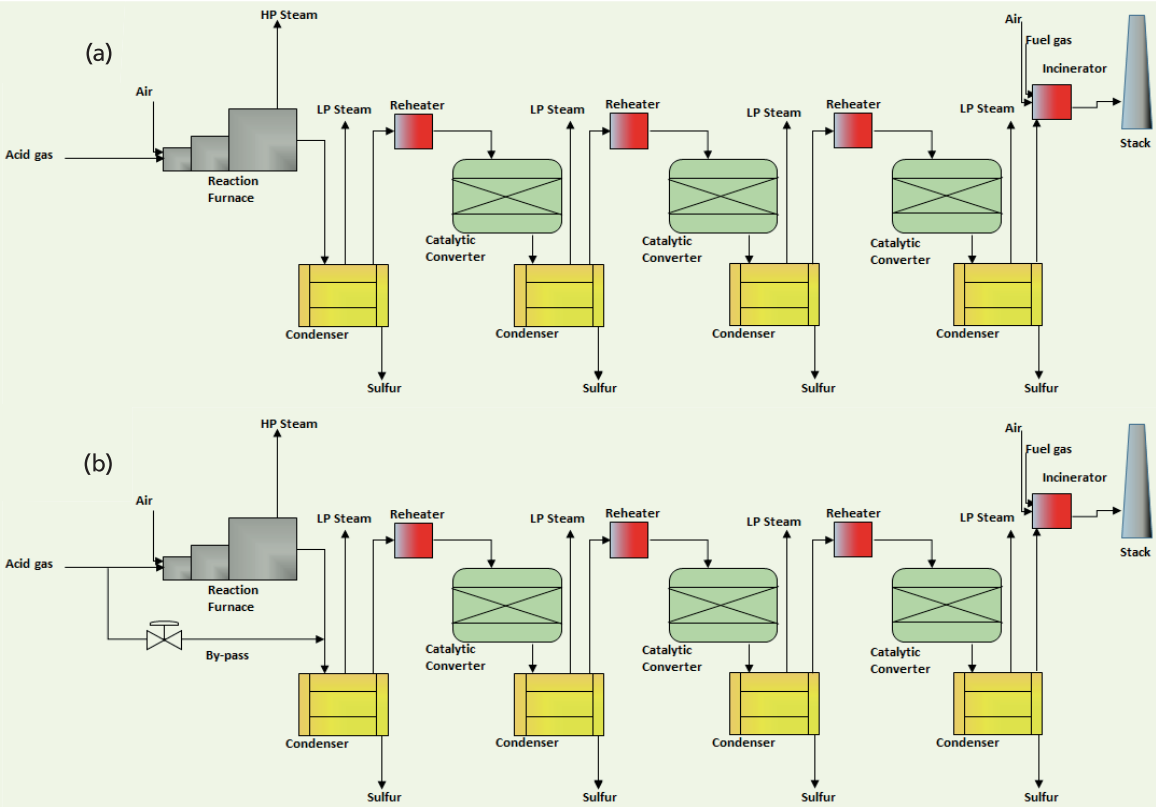

Sulfur Recovery in Split Flow Mode and BTX Issue

Along with the oxidation of one-third of H_2S into SO_2, the reaction furnace of the SRU is also the place for the destruction of hydrocarbon molecules present in the acid gases. A complete destruction of the hydrocarbons requires high temperatures in the reaction furnance[6]: methane is completely destroyed at 1,650 °F, xylene at 1,700 °F, and benzene and toluene at 1,920 °F.

For lean acid gas — containing a low amount of H_2S with respect to CO_2 — a split flow is preferable. A split flow means that a fraction of the acid gas bypasses the reaction furnace. The main reason for this bypass is to minimize the amount of inert (CO_2) in the reaction furnace in an attempt to keep the reaction furnace temperature as high as possible — at least 1,700 °F.

It should be noted that at least one-third of H_2S should be directed to the reaction furnace to ensure that all oxygen is consumed and no oxygen breaks through to the catalyst section, which would damage the catalyst bed. To keep an operational safety margin, the maximal bypass will practically never exceed 60%, i.e., theoretical maximum is 66.67%.

For low H_2S content, indirect air and/or acid gas preheating is applied to reach 1,920 °F in the reaction furnace to ensure BTX destruction[6]. The presence of BTX in the bypass stream remains an issue since this stream is directed to the catalyst stages. At this point, it is important to stress that BTX concentration above a few ppm may cause a loss of catalyst activity within a few hours, and in the extreme range some tailor-made catalyst can sustain BTX in the range of tens of ppm. This results in a drastically shortened life cycle for a Claus converter of 6 months rather than the expected 4 years.

Several plants at Saudi Aramco faced lean acid gases with a high BTX content. A rapid loss of catalyst activity was observed due to the injection of BTX, via the bypass gas going to the catalytic stages. As a remedy, Saudi Aramco has installed carbon bed adsorption units to remove BTX from the acid gas[7]. The acid gases circulate through the bed and hydrocarbons, in particular, BTX is collected by the activated carbon, avoiding the catalyst deactivation, Fig. 3.

The bed is regenerated with low-pressure steam followed by a sweep with dry fuel gas to dry the bed. The activated carbon bed is replaced when its performance begins to decline to avoid carry-over of BTX to the catalyst. The spent carbon is a hazardous waste that requires specialized and costly handling and disposal.

In this article, membrane technology is introduced as an option to increase the time between two replacements of the activated carbon used to remove BTX from the acid gas stream. Ultimately, the membrane

Fig. 3 *The SRU with a split flow configuration and BTX removal unit to avoid introduction of BTX in the catalytic stage.*

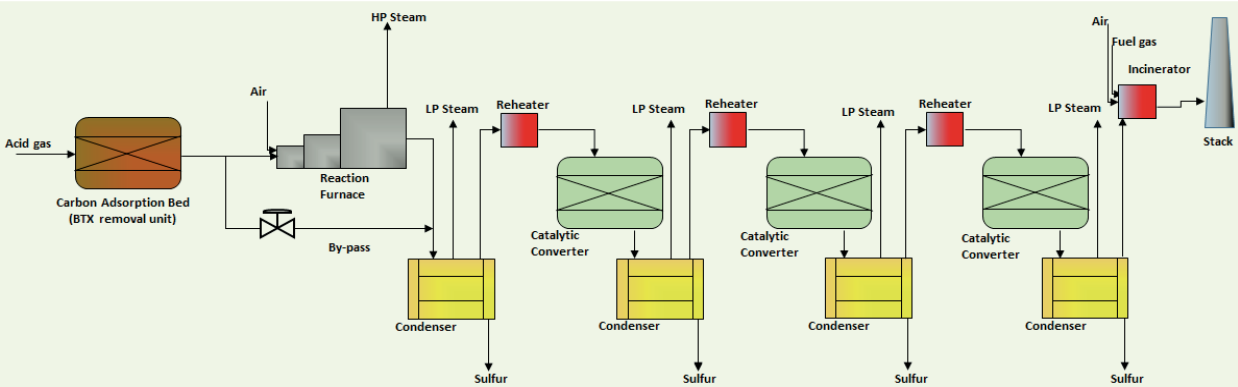

can provide enough BTX rejection to eliminate the need of the activated carbon bed adsorption unit and its regeneration system. Along with BTX rejection, membrane technology can significantly increase H_2S (above 55%), the acid gas feeding the reaction furnace to achieve the desired temperature profile for the destruction of BTX.

Membrane Technology for Partial Acid Gas Enrichment and BTX Rejection

Membrane-based gas separation depends on the ability of gas components to permeate through a nonporous polymeric selective layer at different rates[8]. The difference in permeation rates is due to the molecular size of the gas molecules and/or its solubility in the polymeric layer. It should be noted that the driving force for the gas permeation is the pressure difference across the membrane. The fastest components are concentrated in the low-pressure outlet stream, named permeate, and the slowest components remain in the high-pressure outlet stream, named retentate.

Since CO_2 molecules permeate much faster than methane molecules through the polymeric membrane, CO_2 content is found concentrated in the permeate stream with respect to the inlet. Membrane technology for CO_2 removal has been in use since the mid-1970s, and has therefore, a long track of successful operation[9].

Certain types of polymeric membranes based on fluorinated chemistries exhibit a high permeability rate for CO_2 and a low permeability rate for both H_2S and hydrocarbons (methane and BTX)[10-11]. This kind of membrane concentrates H_2S from a diluted stream and delivers a low-pressure CO_2 concentrate, and a H_2S and hydrocarbon depleted stream.

The purpose of this membrane is to displace BTX and H_2S from the bypass stream and to push them into the sulfur recovery reaction furnace, thereby enabling a higher reaction furnace temperature and BTX destruction, Fig. 4[11]. When the membrane is used, the bypass flow rate can be increased above 60%, and since more than one-third of the H_2S is directed to the reaction furnace, there is no risk of oxygen breakthrough.

For some sulfur recovery applications, as used in petro-chemistry or a refinery, the SRU is also used to destroy ammonia — from the sour water stripper — although, ammonia is very stable and requires a reaction furnace temperature above 2,280 °F[6] to be

Fig. 4 *The SRU with a split flow configuration, CO_2 selective membrane and BTX removal unit to avoid introduction of BTX in the catalytic stage.*

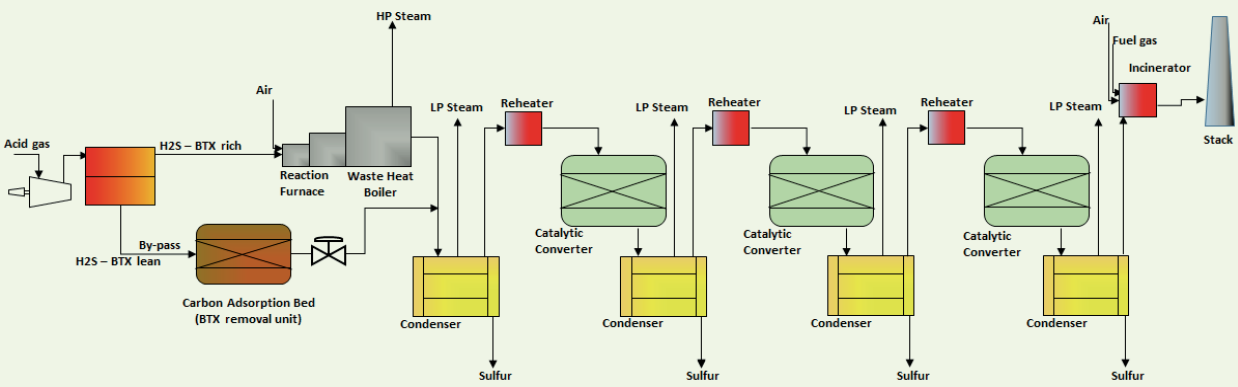

destroyed. To achieve this temperature, a H_2S rich stream is needed as a feed for the SRU. The membrane technology can generate this H_2S rich stream and enable a complete ammonia destruction.

Application of Membrane for Partial Acid Gas Enrichment

Membrane Performance Modeling

Membrane-based gas separation was modeled with the help of a process simulation software PRO II from SimSci. The main purpose of the membrane simulation work is to illustrate the possible H_2S enrichment and the level of BTX that can be achieved with membranes.

Different chemistries provided in the open literature[10] have demonstrated high selectivity for CO_2 vs. H_2S. For all of these chemistries, the material is glassy and prone to reject large molecules like BTX, as compared to CO_2 and H_2S. Process simulations were carried out with membrane selectivity parameters as listed in Table 1.

In this study, membrane feed pressure was set at 155 psig and membrane permeate at 15 psig. The feed pressure is to ensure enough driving force for the membrane operation and can be adjusted by the end user based on its own cost for installed compression and membrane. The permeate pressure is set to ensure enough pressure is used to route the permeate stream to the sulfur recovery plant and avoid additional compression on this stream. The compression of acid gas was achieved by similar equipment to that used for acid gas injection — either reciprocating or centrifugal compressors.

The modeling was performed with targeting a concentration of H_2S in excess of 56% in the reject. The reject is the stream that was sent to the reaction furnace to ensure high temperature and complete BTX and other hydrocarbon destruction.

Table 2 reports the results of the simulation with emphasis on the BTX content in the permeate stream. The merits of the membrane are demonstrated, since H_2S and BTX are simultaneously concentrated. More than 98% of the BTX present in the acid gas is rejected into the H_2S rich gas sent to the reaction furnace. The level of BTX present in the permeate CO_2 rich stream is significantly lower than in the acid gas feeding the membrane.

It is interesting to upgrade the system by changing the feed of the carbon adsorbent bed with the membrane permeate. Such change will reduce the amount of BTX to be removed by the activated carbon and also reduce the load on the recovery and regeneration system associated with the carbon adsorbent bed.

The results of the simulations illustrate the potential benefits of the membrane to reject BTX components to the reaction furnace along with H_2S. The membrane permeate has a BTX concentration 50 times smaller as compared to the original content of the acid gas. This drastic reduction of BTX flow to the carbon adsorbent bed will increase its service life. Ultimately, the membrane permeate can be routed directly to the catalytic converters depending on the achieved performance, Fig. 5, and catalyst tolerance to BTX.

At this point, it should be stressed that BTX components do not have the same deleterious effect on the catalytic bed. According to Crevier et al. (2007)[7], the deactivation factors are as follows: xylene is 4.2 times worse than toluene, and toluene is 17.6 times worse than benzene for the titanium dioxide catalyst at 310 °C.

A sensitivity analysis was conducted with respect to the BTX content and membrane selectivity parameters to assess the potential level of BTX rejection for normal performance and degraded membrane performance. The simulations were performed to assess the amplitude of BTX slippage or concentration increase in the membrane permeate due to a lower selectivity of BTX and H_2S vs. CO_2.

The permeability of the BTX vs. H_2S was doubled as compared to the normal membrane and the H_2S increased by 20% vs. CO_2. The same target of H_2S above 55% was maintained to ensure the reaction

Table 1 *Membrane selectivity parameters used in the simulation.*

Components	Normal Membrane Selectivity vs. H_2S	Degraded Membrane Selectivity vs. H_2S
C1	0.90	0.90
C2	0.40	0.40
C3	0.20	0.20
IC4	0.15	0.15
H_2S	1	1
CO_2	10.00	8.00
H_2O	17.30	17.30
BTEX	0.10	0.20

Table 2 *Membrane feed composition and BTX content in membrane permeate.*

BTEX (ppm) in Acid Gas	100	200	500	1,000	2,000
Membrane feed pressure (psig)	155	155	155	155	155
Membrane permeate (psig)	15	15	15	15	15
C1 (mol%) in acid gas	0.5	0.5	0.5	0.5	0.5
C2 (mol%) in acid gas	0.1	0.1	0.1	0.1	0.1
C3 (mol%) in acid gas	0.05	0.05	0.05	0.05	0.05
IC4 (mol%) in acid gas	0.05	0.05	0.05	0.05	0.05
H_2S (mol%) in acid gas	20, 30, 40	20, 30, 40	20, 30, 40	20, 30, 40	20, 30, 40
CO_2 in acid gas	Balance	Balance	Balance	Balance	Balance
H_2O in acid gas	Saturated	Saturated	Saturated	Saturated	Saturated
Results:					
BTX in permeate (ppm) routed to catalytic converter (normal membrane)	1.7	3.4	8.6	17.2	34.4
BTX in permeate (ppm) routed to catalytic converter (degraded membrane)	4.7	9.3	23.5	47	94
H_2S (mol%) in membrane reject stream routed to SRU reaction furnace	> 55	> 55	> 55	> 55	> 55

Fig. 5 *The SRU with a split flow configuration and CO_2 selective membrane (the BTX removal unit is removed).*

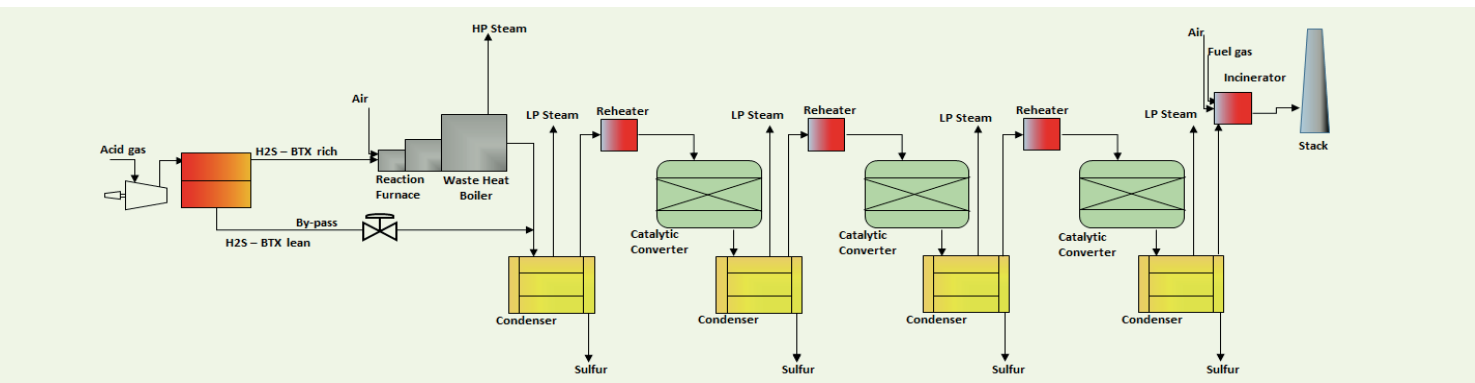

furnace temperature was high enough to destroy any BTX. Due to the higher permeability, the rejection of BTX decreased from 98+% to 95+%. As a result, higher amounts of BTX were sent to the catalytic stage. For the case of 2,000 ppm BTX in the acid gas, a concentration of 94 ppm of BTX is expected in the bypass stream. This may appear high, but as previously mentioned, all BTX components do not have the same deactivation power and focus should be on the xylene and then the toluene content. The analysis is, therefore, on a case-by-case basis to decide if the amount of BTX is an issue or not for the catalyst. As a matter of protecting the catalyst, the carbon adsorbent bed can be maintained to reduce BTX content to the catalytic stage.

SRU Modeling

The heat and mass balance of the SRU process has been obtained with Sulsim® software. A split flow configuration, as previously depicted in Fig. 2b, was selected due to the lean acid gas composition — 20%

Table 3 *Sulfur recovery split flow operation with and without membrane — illustration of the difference process data for streams: Acid gas to reaction furnace, bypass and first condenser.*

		Acid Gas Stream to Reaction Furnace		Bypass Stream		First Condenser Liquid Outlet Stream	
Membrane		No	Yes	No	Yes	No	Yes
Temperature	°F	120	120	120	120	345	345
Pressure	psig	14.3	14.3	14.3	14.3	6.5	6.5
Molar Flow	lb mole/hr	504.0	385.8	756.0	813.5	2.9	126.7
Mass Flow	lb/hr	20,345.5	14,627.1	30,518.3	35,143.6	92.0	4,061.4
C1	(mol%)	0.50	1.45	0.50	0.09	0.00	0.00
CO_2	(mol%)	73.43	40.87	73.43	94.34	0.00	0.00
C_2	(mol%)	0.10	0.31	0.10	0.01	0.00	0.00
H_2S	(mol%)	20.04	56.78	20.04	4.11	0.05	0.03
H_2O	(mol%)	5.81	0.20	5.81	1.45	0.00	0.00
C3	(mol%)	0.05	0.16	0.05	0.00	0.00	0.00
C4	(mol%)	0.05	0.16	0.05	0.00	0.00	0.00
BTX	ppm	200	647	200	3.4	0.00	0.00
S_liquid	(mol%)	0.00	0.00	0.00	0.00	99.95	99.97

H_2S — used for the simulation. Two cases were considered: one with membrane, Fig. 5, and one without membrane, Fig. 2b, with the goal to distinguish the difference due to the presence of the membrane on the sulfur recovery operation.

The bypass was set at 60% in the absence of the membrane since a higher value may result in oxygen breakthrough to the catalytic stage, which is to be avoided to preserve the catalyst performance and integrity. When the membrane is used, a higher bypass is possible while maintaining a large excess of H_2S in the reaction furnace. In the case presented, a bypass of 64% has been selected. Higher bypass flow rates are possible since nearly 87% of the H_2S to be converted into sulfur is sent to the reaction furnace.

This is by far exceeding the required one-third of H_2S to be converted into SO_2. As a consequence, a large amount of sulfur (highlighted in Table 3) is already produced at the reaction furnace/waste heat boiler and collected in the first condenser. This unloads the subsequent catalytic stages and condensers. In contrast, without a membrane and for a 60% bypass, only 40% of the H_2S is sent to the reaction furnace. Since 83.3% of this H_2S will be converted into SO_2 — one-third of the overall H_2S is converted in SO_2 in the reaction furnace — only a small amount of sulfur is collected in the first condenser, which results in loading the subsequent catalyst converters and condensers. It should be noted that the reaction furnace temperatures are different in both cases: without a membrane, a temperature of 2,000 °F is achieved and with a membrane, a temperature of 2,200 °F is achieved.

This higher temperature reflects the H_2S enrichment and reduction in flow rate to the reaction furnace. There is no expectation in improving the overall recovery because no CO_2 was removed from the SRU process and the same number of catalytic stages and sulfur condensers were used.

Table 3 displays the process data for the acid gas stream sent to the reaction furnace or in the bypass, as well as the flow rate of sulfur.

Conclusions

The main conclusions of this study are:

- The membrane can enrich low content H_2S to above 55% and concentrate 98+% of BTX in the stream sent to the SRU reaction furnace. This H_2S enrichment ensures that any contaminants, like BTX, which are catalyst deactivators, are destroyed in the reaction furnace of the SRU.
- The BTX is rejected from the SRU bypass stream (split flow SRU operation) allowing it to direct this gas directly to the catalytic stage or via a significantly smaller BTX removal unit as compared to without use of a membrane.
- The large excess of H_2S routed to the reaction furnace guarantees that no oxygen breakthrough to the catalytic stages will occur using the membrane.
- Although the application of partial acid gas enrichment is new for membrane technology, membranes

have a long track record for bulk CO_2 removal from natural gas.

- The membrane requires gas compression since the acid gas leaving the amine unit is at 10 psig to 15 psig, and the membrane operation requires pressure in the range 50 psig to 250 psig. Safety associated with wet acid gas compression is addressed in many plants, especially the ones involved in acid gas injection.
- Upgrading the split flow operation in the SRU with a membrane does not require any air control logic change.
- Finally, the membrane technology and split flow configuration may offer alternatives to the traditional acid gas enrichment with H_2S selective amine.

References

1. Manning, F.S. and Thompson, R.E.: *Oilfield Processing of Petroleum, Vol. 1: Natural Gas*, PennWell Corp., 1991, 408 p.
2. Stewart. M.: *Surface Production Operations: Vol 2: Design of Gas Handling Systems and Facilities*, 3rd edition, Gulf Professional Publishing, 2014, 672 p.
3. Kidnay, A.J., Parrish, W.R. and McCartney, D.G.: *Fundamentals of Natural Gas Processing*, 3rd edition, CRC Press, 2019, 498 p.
4. Kohl, A.L. and Nielsen, R.: *Gas Purification*, 5th edition, Gulf Publishing, 1997, 900 p.
5. McIntyre, G.D., Hernandez-Valencia, V.N. and Lunsford, K.M.: "Recent GPA Data Improves BTEX Predictions for Amine Sweetening Facilities," paper presented at the 80th Gas Processors Association Convention, San Antonio, Texas, March 12-14, 2001.
6. Paskall, H.G. and Sames, J.A.: *Sulphur Recovery*, Sulphur Experts, 2003.
7. Crevier, P.P., Adab, A.M., Baaqeel, H., Hummam, I.A., et al.: "BTX: Problem and Solution — Conclusion: CBUs Eliminate BTX-Induced Catalyst Deactivation," *Oil and Gas Journal*, Vol. 105, Issue 41, November 2007, pp. 82-90.
8. Baker, R.W.: *Membrane Technology and Applications*, 3rd edition, Wiley, 2012, 590 p.
9. Drioli, E. and Barbieri, G. (editors): *Membrane Engineering for the Treatment of Gases: Vol. 1: Gas-Separation Problems with Membranes*, 1st edition, Royal Society of Chemistry, 2011, 298 p.
10. Merkel, T. and Toy, L.G.: "Comparison of Hydrogen Sulfide Transport Properties in Fluorinated and Nonfluorinated Polymers," *Macromolecules*, Vol. 39, Issue 22, September 2006, pp. 7591-7600.
11. Ballaguet, J-P.R., Vaidya, M.M., Duval, S.A., Harale, H., et al.: "Sulfur Recovery Process for Treating Low to Medium Mole Percent Hydrogen Sulfide Gas Feeds with BTEX in a Claus Unit," U.S. Patents No. 9,981,848 and 9,593,015.

About the Authors

Dr. Milind M. Vaidya

Ph.D. in Polymer Science, NYU/Polytechnic School of Engineering

Dr. Milind M. Vaidya is a Research Science Consultant working in the Oil and Gas Treatment Division of Saudi Aramco's Research & Development Center. He joined Saudi Aramco in 2002.

Milind is the coauthor of 23 journal articles and papers in conference proceedings and 18 presentations given at international conferences. He is also an inventor, holding 57 granted patents.

Milind received his first M.S. degree in Physical Chemistry from the University of Mumbai, Mumbai, India, and his second M.S. degree in Polymer Science from the University of Akron, Akron, OH. Milind received his Ph.D. degree in Polymer Science from the NYU/Polytechnic School of Engineering, New York City, NY.

He has a total of 36 years of experience in the field of polymer material science.

Dr. Sebastien A. Duval

Ph.D. in Electrochemistry, University of Paris IV

Dr. Sebastien A. Duval is a Research Science Consultant working with the Natural Gas Upgrading and Storage team in Saudi Aramco's Research and Development Center (R&DC). Prior to joining Saudi Aramco in 2006, he held the following positions: Research Scientist at Institut Français du Pétrole, Materials Selection and Corrosion Principal Engineer at Saipem SA, and then as a Consultant for Offshore Projects.

Sebastien has authored and coauthored more than 30 papers and holds 25 patents. He is member of National Association of Corrosion Engineers (NACE) International and the Society of Petroleum Engineers (SPE).

Sebastien received his Ph.D. degree in Electrochemistry from the University of Paris IV, Paris, France, in 2000.

Dr. Feras Hamad

Ph.D. in Chemical Engineering, University of Ottawa

Dr. Feras Hamad is an Engineering Specialist working in the Natural Gas Upgrading and Storage team in the Oil and Gas Treatment Division of Saudi Aramco's Research & Development Center. He joined Saudi Aramco in 2008, and since then, Feras has been focusing on the development of membrane technologies.

Previously, he worked in several companies with a total experience of over 20 years.

Feras has coauthored more than 19 peer-reviewed publications, and is a co-inventor of six granted patents for Saudi Aramco.

He received his Ph.D. degree in Chemical Engineering from the University of Ottawa, Ottawa, Ontario, Canada.

John P. O'Connell

B.S. in Chemical Engineering, University of Calgary

John P. O'Connell is a Sulfur Recovery Subject Matter Expert in the Gas Processing Group of Saudi Aramco's Process & Control Systems Department. He is an internationally recognized authority in the field of sulfur recovery, having spent 33 years in the industry.

John founded Sulfur Recovery Engineering (SRE) in 1998, which is a well-recognized consulting company, which offers many different services to gas treating and sulfur recovery operating companies worldwide, with a specialty in sour process gas collection and analysis. He created proprietary gas analysis and sampling technique methodologies as well as in-house sulfur simulation software for SRE's operations.

John currently holds four patents in the field of sulfur recovery for Saudi Aramco and is the creator of the extremely successful Sulfur Solutions Dashboard, which in co-operation with facility operations, has reduced the company's sulfur dioxide emissions by over 250,000 tons since its inception in 2017.

He received his B.S. degree in Chemical Engineering from the University of Calgary, Calgary, Alberta, Canada.

Ghulam Shabbir

M.S. in Chemical Engineering, Institute of Chemical Engineering and Technology

Ghulam Shabbir is working as an Engineering Specialist with the Technical Evaluation Unit of Saudi Aramco's Gas Operations Technical Support and Planning Department.

During his 24-year career in the oil and gas industry, he had provided technical support as a Process/Operation Engineer for the development of many major and mega-projects for Saudi Aramco, as well as for other international operating companies. Ghulam's area of interest is process simulation, NGL recovery, gas treatment and sulfur recovery units.

He received his B.S. degre in Chemical Engineering (with honors) from the University of Engineering & Technology, Lahore, Pakistan. Ghulam received his M.S. degree in Chemical Engineering from the Institute of Chemical Engineering and Technology, Punjab, Lahore, Pakistan.

Ahmed J. Al-Talib

B.S. in Chemical Engineering, Arizona State University

Ahmed J. Al Talib is a Gas Processing Research Engineer working in the Oil and Gas Treatment Division of Saudi Aramco's Research & Development Center. He joined Saudi Aramco in 2012. Ahmed's research work is focused on the validation and integration of membrane gas separation processes for high acid gas removal and carbon capture applications.

He completed a 15-month field deployment assignment as a Process Engineer at the Ju'aymah NGL Fractionation Plant, the world's largest NGL fractionation plant.

Ahmed participated in the organizing committee of ChemIndix 2016 Conference & Exhibition as the Communication & Marketing Team Leader.

In 2012, he received his B.S. degree in Chemical Engineering from Arizona State University, Tempe, AZ.

Dr. Ahmad A. Bahamdan

Ph.D. in Chemistry, Louisiana State University

Dr. Ahmad A. Bahamdan is a Research Science Consultant and the team leader of the Natural Gas Upgrading and Storage team in the Oil and Gas Treatment Division of Saudi Aramco's Research & Development Center. He is a specialist in polymer science and its applications in the oil and gas industry, with 25 years of experience in this field.

Ahmad currently holds six granted patents and 12 published technical papers in refereed journals in the field of polymeric membranes for gas and liquid separations, nonmetallic materials, and polymers for drilling and fracturing fluids.

He received his B.S. degree in Chemistry from King Fahd University of Petroleum and Minerals (KFUPM), Dhahran, Saudi Arabia. Ahmad received his M.S. degree in Chemistry from the University of Arkansas, Little Rock AR, and his Ph.D. degree in Chemistry (Polymer Science) from Louisiana State University, Baton Rouge, LA.

Dr. Faisal D. Al-Otaibi

Ph.D. in Chemical Engineering, University of Calgary

Dr. Faisal D. Al-Otaibi is the Chief Technologist working in the Oil and Gas Treatment Division of Saudi Aramco's Research & Development Center.

He has a wide range of oil and gas industrial experience, including work in oil and gas production facilities, refining and distribution, and gas plants. Faisal also completed an internship assignment at the UOP-Honeywell research center.

He has several published articles in refereed journals and has conducted several workshops, taught college level courses, and presented in many international conferences related to gas hydrates, oil and gas processing, and the application of membranes in the oil and gas industry

Faisal received his B.S. degree in Chemical Engineering from the University of Tulsa, Tulsa, OK, and his M.S. and Ph.D. degrees in Chemical Engineering from the University of Calgary, Calgary, Alberta, Canada.

Integrated Multi-Frequency Characterization of Sandstone Rocks

Dr. Damian P. San-Roman-Alerigi, Dr. Oliverio Alvarez, Dr. Sameeh I. Batarseh and Bander M. Al-Khaldi

Abstract /

The ultimate goal of our work is to develop an electromagnetic (EM) multi-frequency integrated system to enable real-time and in situ characterization during high power EM operations, e.g., logging-while-lasing or logging-while-microwaving. The sensing platform should provide information about the environment, the substrate, the near wellbore (ahead of the beam), and the process.

Real-time sensing is necessary because high power EM operations are faster and avail more control to target the EM energy to attain a specific purpose. Therefore, the sensing systems must be compatible and operate simultaneously with high power EM radiation. In this context, EM multi-frequency characterization could provide valuable information to evaluate the near wellbore volume, fluids, and the environment. This article introduces essential spectrometry components and analytics.

The experiments reported focus on the characterization of tight sandstone rocks from different reservoirs. The characterization process used various tools: microwave and radio frequency resonators, Fourier transform infrared reflectometry (FTIR), porosimetry, and sonic reflectometry. Five resonances were measured using a custom-made microwave resonator with measurements at frequencies between 980 MHz to 3.5 GHz. As this comprehensive characterization evolves, it will use machine learning algorithms to display the correlation between the EM response of the material and other rock properties, e.g., clay content, saturation, porosity, and mechanical properties.

FTIR and low frequency impedance enable the characterization at the surface and bulk volume, respectively. The experimental results confirm the correlation between some chemical, mechanical, and EM properties of materials. These relations could be used to derive clay content, total organic carbon content, maturity, and saturation, among other material properties. The results of this characterization contribute to the growing database of EM properties of rocks under different configurations. The expectation is that this information can be coupled with statistical and machine learning algorithms to build edge neural engines for subsurface characterization and high power EM tools.

EM tools and methods for subsurface use allow characterizing the formation with high accuracy and resolution. The combined results and algorithms could enable the estimation of rock type, porosity, saturation, and other properties while conducting high power EM operations. The information provided could eventually enable automated systems and logging-while-lasing.

This work presents the foundational blocks to achieve this and guide the development of subsurface laser technologies.

Introduction

This article presents a summary of some developments in the road to creating a subsurface electromagnetic (EM) platform for in situ characterization. The primary purpose is to enable comprehensive logging during high power EM applications, such as lasing and microwaving. The implication is that the sensing platform would allow the high power EM tools to "see" in front, around, and ahead of themselves, with varying degrees of resolutions. Real-time sensing is necessary because high power EM operations and subsurface robots are fast and avail more control. Given the multipurpose goal of the platform, the sensing systems must be compatible and operate simultaneously with other EM tools, e.g., high power lasers and microwave stimulation tools.

EM multi-frequency sensors are a natural choice; they can provide information to evaluate subsurface fluids[1], near wellbore volume[2], composition[3], and high power EM processes[4]. In the field, the information coming from these sensors would feed edge neural engines that derive fast predictions, which in turn can be used to control the high power EM processes, evaluate the outcome, and direct the tools. Consequently, secondary applications include any subsurface automated and robotic system that may benefit from these features.

The initial work focused on spectral characterization in the microwave and near infrared range for the EM spectrum. Subsurface spectrometry traditionally measured the dielectric constant of the medium between a transmitter and a receiver at some given set of frequencies[5]. Infrared reflectometry has been utilized to characterize in situ crude oils[6], carbon dioxide content[7], or mineralogy[8].

Fig. 1 *Experimental setup. The TM_{0np} cavity (front) connected to the R&S ZVA vector network analyzer (back). Thorlabs translation stages move the antenna in controlled steps with a minimum resolution of 1 µm (left).*

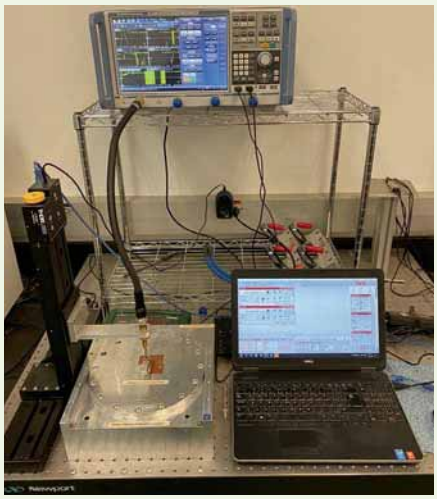

Fig. 2 *Image of the cavity with the sample installed.*

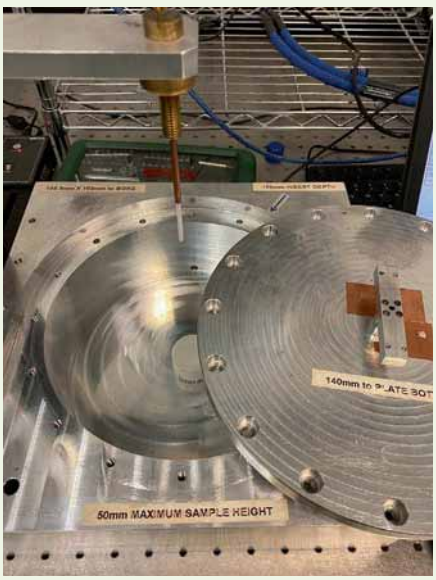

Spectroscopy can be combined with machine learning to conduct in field pressure-volume-temperature[9] or quantitative gas analysis[10]. In the laboratory, microwave and Raman spectrometry have been used to characterize the total organic carbon content and the composition of complex geomaterials[2, 3]. In contrast, Fourier-transform infrared reflectometry (FTIR) has been utilized to characterize the geochemical properties of subsurface matter, including maturity inference and total organic carbon content[4, 11, 12].

A custom-made microwave resonator was used to characterize the bulk volume. The resonator measures discrete points between 980 MHz and 3.5 GHz. The cavity measures the complex permittivity () of solid core plugs with a diameter between 2 cm to 3.8 cm and a maximum height of 5.5 cm. The system could study plugs and cuttings at the surface using a mobile lab.

FTIR was used to characterize the near surface composition. The FTIR probe is part of a multiprobe system known as AutoScan, which leverages automation to map measurements over a dense grid with a minimum spatial resolution of 100 µm. The device can characterize plugs, slabs, or any quasi-flat surface.

San-Roman-Alerigi et al. (2019)[4] combined FTIR and near infrared reflectometry with machine learning to reveal the maturation of organic-rich shales subject to high power laser irradiation.

Fig. 3 *Permittivity of six sandstone plugs: (a) The real part of the permittivity, and (b) The imaginary part of the permittivity.*

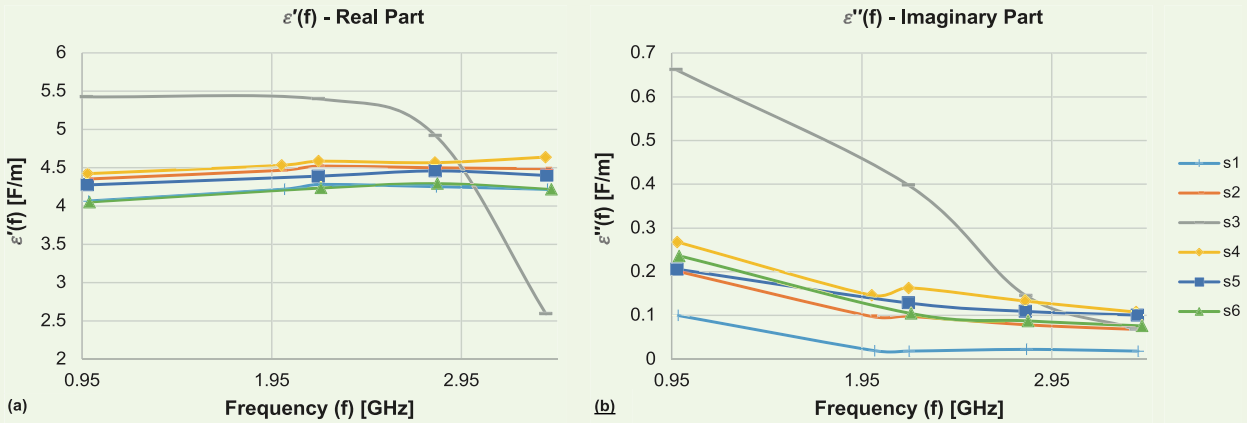

Table 1 *The calculated permittivity for sandstone rocks for five modes between 0.98 MHz and 3.5 GHz. The results are separated into real (ε′) and imaginary (ε″) components. The symbol ∂ε′ denotes the corresponding uncertainty.*

Sample	Mode	f (Hz)	ε′	∂ε′	ε″	∂ε′
1	Mode 1	9.83E+08	4.0648	0.02952	0.0999	0.00500
	Mode 2	2.02E+09	4.2198	0.01422	0.0194	0.00097
	Mode 3	2.20E+09	4.2808	0.00467	0.0184	0.00092
	Mode 4	2.82E+09	4.2523	0.71961	0.0223	0.00112
	Mode 5	3.40E+09	4.2171	0.86789	0.0183	0.00092
2	Mode 1	9.78E+08	4.3517	0.05975	0.2012	0.01006
	Mode 2	2.00E+09	4.4663	0.00896	0.0977	0.00489
	Mode 3	2.19E+09	4.5200	0.03540	0.0980	0.00490
	Mode 4	2.81E+09	4.4989	0.00445	0.0786	0.00393
	Mode 5	3.40E+09	4.4869	0.00449	0.0679	0.00340
3	Mode 1	9.73E+08	5.4257	0.27646	0.6617	0.03309
	Mode 3	2.20E+09	5.3984	0.24822	0.3978	0.01989
	Mode 4	2.81E+09	4.9192	0.00492	0.1454	0.00727
	Mode 5	3.40E+09	2.5885	0.01545	0.0689	0.00345
4	Mode 1	9.79E+08	4.4220	0.10403	0.2679	0.01340
	Mode 2	2.00E+09	4.5315	0.00453	0.1462	0.00731
	Mode 3	2.20E+09	4.5847	0.10033	0.1631	0.00816
	Mode 4	2.81E+09	4.5659	0.00457	0.1328	0.00664
	Mode 5	3.39E+09	4.6385	0.00431	0.1076	0.00538
5	Mode 1	9.79E+08	4.2749	0.07953	0.2056	0.01028
	Mode 3	2.20E+09	4.3898	0.07745	0.1284	0.00642
	Mode 4	2.81E+09	4.4578	0.00446	0.1092	0.00546
	Mode 5	3.40E+09	4.3989	0.00455	0.1006	0.00503
6	Mode 1	9.88E+08	4.0523	0.11845	0.2364	0.01182
	Mode 3	2.21E+09	4.2345	0.05195	0.1043	0.00522
	Mode 4	2.82E+09	4.2913	0.00429	0.0874	0.00437
	Mode 5	3.43E+09	4.2151	0.00474	0.0759	0.00380

Methods

Microwave Resonant Cavity

The character used the TM_{0np} cavity described in Alvarez (2017)[1] and Alvarez and Penaranda-Foix (2018)[2] with some modifications, Fig. 1. The system was upgraded to use translation stages to control the insertion of the antenna and measurement depths with a minimum resolution of 1 μm. The motion control enables a complete scan of the cavity modes with high precision. This feature proved essential to scan the depth and identify the resonant modes, since their positions may vary depending on the rock type.

The measurement process is as follows:

1. The vector network analyzer (Rohde and Schwarz ZNB20 vector network analyzer (VNA)) is calibrated using an Agilent 85052B calibration kit.
2. The antenna is connected to the VNA using a VNA cable (Gore).
3. The empty cavity is closed, and the antenna scanned along the axis of the cavity to measure the six resonant modes. The data is labeled as "air" and stored.
4. The antenna is returned to the home position. The cavity is then opened, and the cylindrical sample

Fig. 4 *The FTIR spectra of the sandstone samples from several outcrops (measurement numbered 0 to 11,000) and Berea sandstone blocks (measurement number 11,001 to 20,000). The spectra were normalized and scaled over the features in preparation for machine learning.*

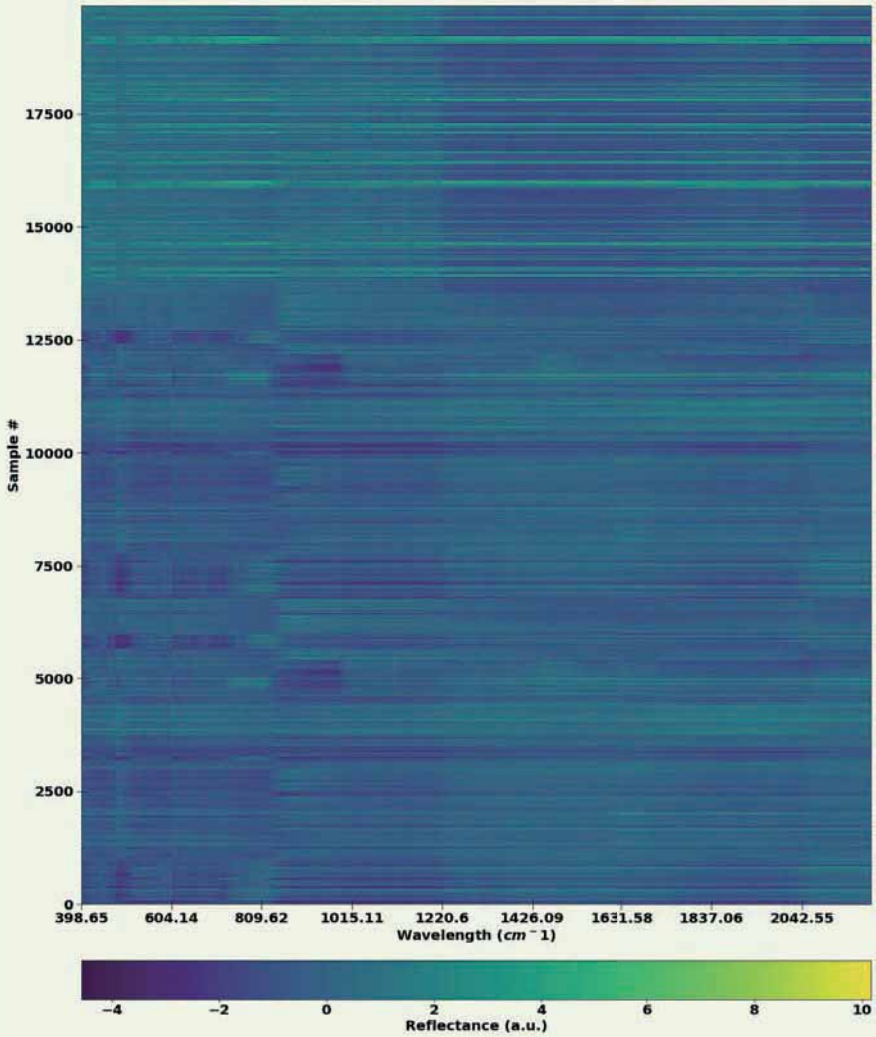

Fig. 5 *The FTIR spectra of the six sandstone plugs from unidentified outcrops. The spectra were normalized and scaled over the features in preparation for machine learning routines.*

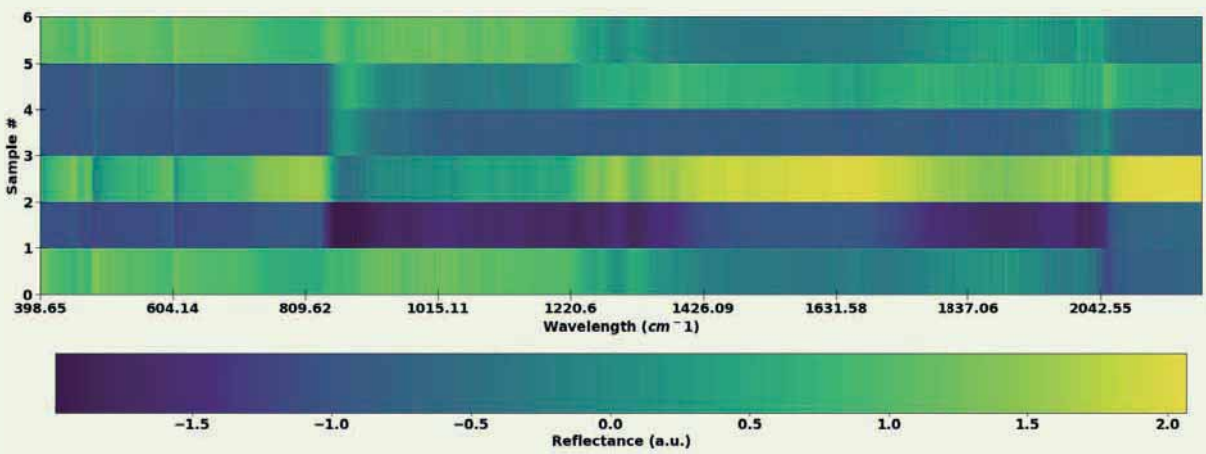

Fig. 6 *Principal component analysis (PCA) of the full spectra. (a) PCA colored by the sample provenance; points corresponding to the Berea sandstone are shown in yellow, and the outcrops 1 to 3 in pink, light purple, and blue. (b) PCA is colored by corresponding K-means cluster with the corresponding cluster node shown in red. The cluster number is given from top-left to bottom-right.*

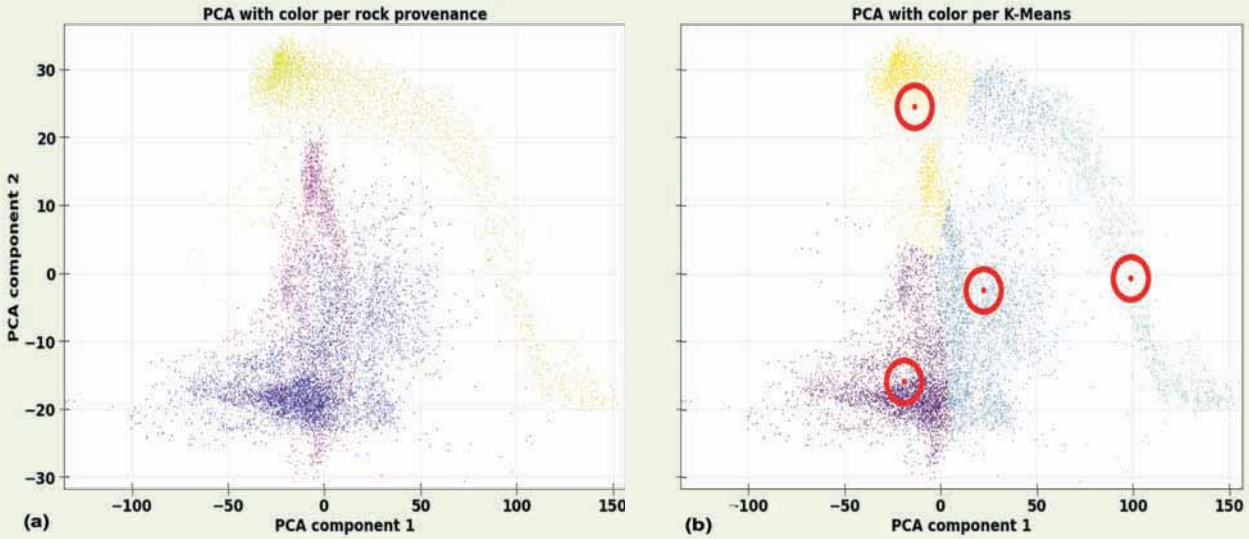

is placed inside, Fig. 2.

5. The cavity with the sample is closed, and the antenna scanned along the axis of the cavity to identify the top and bottom resonant modes using the Schmidt chart as a guide.
6. Measurements are taken every 2 mm between the top and bottom positions identified in step 5. The data is labeled with the corresponding sample name and stored.
7. The stored measurements are processed using ITACA software. It does a coupling correction, identifies the resonant frequency, and calculates the components of the permittivity, Eqn. 1:

$$\varepsilon = \varepsilon' + j\varepsilon'', \; j = \sqrt{-1} \quad (1)$$

FTIR Scan

This characterization step used the AutoScan platform to measure gas permeability, ultrasonic compressional/shear wave velocities, and FTIR, albeit only the last is reported in this text. The device performs a 2D mapping of the measurements in a cartesian grid defined by the user.

The FTIR measurement spectrometer was mounted on a translation stage. The device measures the absorption spectrum of the samples in the mid-infrared range. The diameter of the measurement spot was 3 mm.

This part of the study used the same plug samples as well as their corresponding slabs. In the plugs, measurements were taken at two positions, top and bottom. A scan was performed on the slabs using a step size of 0.25 mm in width and length.

Results

Microwave Resonant Cavity

The tests used six plugs taken from field samples of unidentified sandstone outcrops. The samples were unsaturated. All the measurements were done at a controlled temperature (25 °C) and humidity (~30%).

The compiled results of the measurement are plotted in Fig. 3. It shows the real and imaginary components of the permittivity (Eqn. 1). Table 1 summarizes the calculated values for both parts with their corresponding error.

All the samples, except for sample 3, exhibit similar behavior with almost flat response for the real permittivity ($\varepsilon' \approx f \cdot 4.398\ F/m$) for all frequencies. Similarly, the loss follows an almost constant trend, except for sample 3. The loss is highest at 0.98 GHz and slowly decreases until ~2 GHz; after this point, the loss flattens at ~0.08 F/m.

Little experimental data has looked at the permittivity within the range of study in this article. Yet, some prior results, $f < 1$ GHz, suggest that the values are consistent with sandstone samples with low porosity and mostly composed of quartz[13-16]. The results for sample 3 could be explained by the presence of some organic matter or other materials. Subsequently, given the absence of a geochemical analysis for these rocks, it is not possible to provide a satisfactory conclusion at this point.

FTIR

This test scanned the six plugs used in the microwave cavity, as well as their corresponding slabs. Also, the scan was performed in several Berea gray sandstones. The samples were unsaturated. All the measurements

were done at a controlled temperature (25 °C) and humidity (~30%). In total, the automated FTIR captured 20,000 spectra, of which 13,750 were taken in the slabs and plugs, and 6,250 on various Berea sandstone blocks. The normalized and scaled FTIR spectra for all samples are plotted in Fig. 4.

The spectra corresponding to the Berea gray sandstone shows almost no change between samples, which is expected given that the samples are uniform. The outcrop samples show higher variability due to the presence of different minerals or contaminants.

Figure 5 shows the FTIR spectra of the six sandstone plugs. The results show that each plug had a distinct spectral signature, which would imply variation in composition. Subsequently, as mentioned earlier in the discussion, the results need to be complemented with a geochemical analysis. Yet, it is possible to study the spectra using machine learning algorithms to understand how the samples may differ from each other.

Figure 6 shows the plot of the principal component analysis (PCA) performed over the entire set of spectra. The results are plotted in two coloring schemes showing the sample provenance and K-means cluster. The results show that the majority of the Berea sandstone samples are concentrated in cluster 1 (top right), whereas the outcrop samples are distributed in the remaining three groups. Yet, the K-means analysis suggests that at least a portion of the outcrops share some similarity with the Berea gray sandstones. This result could be due to the high presence of silica.

Figure 7 shows the output of the t-distributed stochastic neighbor embedding (tSNE) on the full data set. It was calculated using the tSNE Spectral Clustering routine implemented by using scikit-learn sofware. The study was repeated with different values of perplexity but showed significant change. The analysis would cluster the data into a single group. The outcome shows no discernable clustering within the spectral data. This outcome contrasts with the result given by K-means; however, it is consistent with the fact that the samples are sandstone, and therefore mostly silica.

Fig. 7 *The tSNE analysis of the full spectral data. The colors correspond to the K-means cluster for that point.*

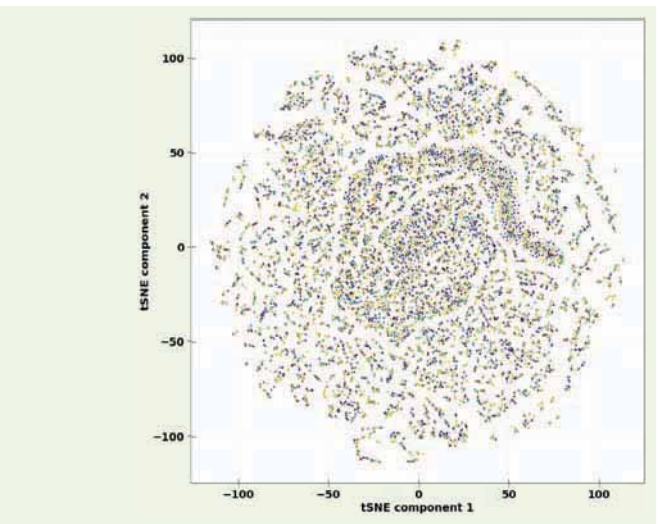

Conclusions

The tests reported in this article are for tight sandstone of an unknown origin and Berea gray sandstone samples. Future work will expand the characterization to other rock types with diverse oil and water saturations.

Past and current experimental results demonstrated that EM properties could be proxies to determine chemical and mechanical properties[4, 17]. These works suggest that the combination with machine learning could enable the estimation of the rock type, porosity, saturation, and other properties while conducting laser operations. The information provided could eventually enable automated systems and logging-while-lasing.

The measurements contribute to the growing catalog of EM properties of rocks under different configurations. The methods will be used in the future to study other rock types at different conditions. The results suggest that reflectance spectrometry could be used to evaluate the effect of high power EM processes, build predictive models, and support the development of autonomous subsurface tools.

In the future, these comprehensive characterizations will be used in conjunction with machine learning algorithms to reveal the correlation between the EM response of the material and other rock properties, e.g., clay content, saturation, porosity, and mechanical properties.

Acknowledgments

This article was prepared for presentation at the Abu Dhabi International Petroleum Exhibition and Conference, Abu Dhabi, UAE, November 9-12, 2020.

References

1. Alvarez, J.O., Jacobi, D. and Bernero, G.: "Dielectric Characterization of Geochemical Properties of Crude Oils and Gas Condensate at 25 °C," paper presented at the IEEE International Geoscience and Remote Sensing Symposium (IGARSS), Fort Worth, Texas, July 23-28, 2017.

2. Alvarez, J.O. and Penaranda-Foix, F.L.: "Multifrequency Microwave Resonance Cavity for Nondestructive Core Plug Measurements," paper presented at the IEEE International Geoscience and Remote Sensing Symposium (IGARSS), Valencia, Spain, July 22-27, 2018.

3. Alvarez, J.O., Penaranda-Foix, F.L., Catala-Civera, J.M. and Gutierrez-Cano, J.D.: "Permittivity Spectrum of Low-Loss Liquid and Powder Geomaterials Using Multipoint Reentrant Cavities," *IEEE Transactions on Geoscience and Remote Sensing*, Vol. 58, Issue 5, May 2020, pp. 3097-3112.

4. San-Roman-Alerigi, D.P., Batarseh, S.I., Li, W. and Othman, H.: "Machine Learning and the Analysis of High Power Electromagnetic Interaction with Subsurface Matter," SPE Middle East Oil and Gas Show and Conference, Manama, Kingdom of Bahrain, March 18-21, 2019.

5. Ellis, D.V. and Singer, J.M.: *Well Logging for Earth Scientists*, 2nd edition, Springer, Dordrecht, the Netherlands, 2007, 708 p.

6. Mullins, O.C., Rodgers, R.P., Weinheber, P., Klein, G.C., et al.: "Oil Reservoir Characterization via Crude Oil Analysis by Downhole Fluid Analysis in Oil Wells with Visible Near Infrared Spectroscopy and by Laboratory Analysis with Electrospray Ionization Fourier Transform Ion Cyclotron Resonance Mass Spectrometry," *Energy & Fuels*, Vol. 20, Issue 6, October 2006, pp. 2448-2456.

7. Piazza, R., Vieira, A., Sacorague, L.A., Jones, C., et al.: "Real-Time Downhole mid-IR Measurement of Carbon Dioxide Content," paper presented at the SPWLA 60th Annual Logging Symposium, The Woodlands, Texas, June 15-19, 2019.

8. Menier, A., Roy, R., Harrison, G., Zerff, R.W., et al.: "Relationship between Rock Physical Properties and Spectral Mineralogy Applied to Exploration for an Unconformity-Related Uranium Deposit (Saskatchewan, Canada)," *Canadian Journal of Earth Sciences*, Vol. 57, Issue 11, March 2020, pp. 1349-1364.

9. Lehne, E. and Cartellieri, A.: "Predicting PVT Properties Using Multivariate Data Analysis of Optical Spectra," paper presented at the Offshore Mediterranean Conference and Exhibition, Ravenna, Italy, March 27-29, 2019.

10. Song, L., Wu, H., Yang, Y., Guo, Q., et al.: "Application of Deep Learning in Quantitative Analysis of the Infrared Spectrum of Logging Gas," *Applied Optics*, Vol. 59, Issue 17, January 2020, pp. E9-E16.

11. Ji, J., Ge, Y., Balsam, W., Damuth, J.E., et al.: "Rapid Identification of Dolomite Using a Fourier Transform Infrared Spectrophotometer (FTIR): A Fast Method for Identifying Heinrich Events in IODP Site U1308," *Marine Geology*, Vol. 258, Issues 1-4, March 2009, pp. 60-68.

12. Cheng, C., Liu, J., Zhang, C., Cai, M., et al.: "An Overview of Infrared Spectroscopy Based on Continuous Wavelet Transform Combined with Machine Learning Algorithms: Application to Chinese Medicines, Plant Classification, and Cancer Diagnosis," *Applied Spectroscopy Reviews*, Vol. 45, Issue 2, March 2010, pp. 148-164.

13. Duba, A., Piwinskii, A.J., Santor, M. and Weed, H.C.: "Comments on 'The Electrical Conductivity of Sandstone, Limestone and Granite'," *Geophysical Journal International*, Vol. 56, Issue 3, March 1979, pp. 477-479.

14. Knight, R.J. and Nur, A.: "Dielectric Constant of Sandstones, 60 kHz to 4 MHz," *Geophysics*, Vol. 52, Issue 5, May 1987, pp. 644-654.

15. Ulaby, F.T., Bengal, T.H., Dobson, M.C., East, J.R., et al.: "Microwave Dielectric Properties of Dry Rocks," *IEEE Transactions on Geoscience and Remote Sensing*, Vol. 28, Issue 3, May 1990, pp. 325-336.

16. Brovelli, A., Cassiani, G., Dalla, E., Bergamini, F., et al.: "Electrical Properties of Partially Saturated Sandstones: Novel Computational Approach with Hydrogeophysical Applications," *Water Resources Research*, Vol. 41, Issue 8, August 2005, pp. 1-12.

17. Batarseh, S.I., San-Roman-Alerigi, D.P., Al Harith, A. and Othman, H.A.: "Laser Perforation: The Smart Completion," SPE paper 187192, presented at the Abu Dhabi International Petroleum Exhibition and Conference, Abu Dhabi, UAE, November 11-14, 2019.

About the Authors

Dr. Damian P. San-Roman-Alerigi

Ph.D. in Electrical Engineering, King Abdullah University of Science and Technology

Dr. Damian P. San-Roman-Alerigi is a Petroleum Scientist working with the Production Technology Team of Saudi Aramco's Exploration and Petroleum Engineering Center – Advanced Research Center (EXPEC ARC). His focus is on developing the next generation of subsurface photonic and electromagnetic tools.

Damian's previous research focused on the interaction of waves with complex media and its application to subsurface technologies. His work encompasses different areas of science and engineering, from oil and gas to applied mathematics. He has published papers in various international journals and conferences around the world.

Damian received his B.S. degree in Physics from the National Autonomous University of Mexico, Mexico City, Mexico. In 2008, he enrolled in King Abdullah University of Science and Technology (KAUST) as a founding class student where he completed his M.S. degree in 2010, and his Ph.D. degree in 2014, both in Electrical Engineering.

Dr. Oliverio Alvarez

Ph.D. in Applied Mathematics, University of Arizona

Dr. Oliverio Alvarez is the Technology Leader for microwave applications of the Sensors Development Team (SDT), the Aramco Americas (formally Aramco Services Company), Aramco Research Center-Houston, joining the company in 2014. He has 15 years of experience both in geoscience and engineering. Oliverio has designed and/or developed microwave technologies for the characterization of geochemical properties of rocks and production fluids.

Prior to joining Aramco Americas, he spent eight years at the ExxonMobil Upstream Research Company, where he worked in completion design for acid stimulation, sand transport, detonation modeling, drilling vibrations, formation evaluation, acoustic logging, and cement bond logging.

Oliverio is an author in highly ranked peer-reviewed journals and in several conferences. He has six granted patents in well stimulation, microwave water cut metering, and microwave measurements. Oliverio is also a reviewer for several internationally renowned journals. He is a senior member of the Institute of Electrical and Electronics Engineers (IEEE) and an active member of the Geoscience and Remote Sensing Society (GRSS).

In 2005, Oliverio received his Ph.D. degree in Applied Mathematics with a minor in Aerospace Engineering from the University of Arizona, Tucson, AZ. He also received a Digital Signal Processing Graduate Certificate from Purdue University in 2013.

Dr. Sameeh I. Batarseh

Ph.D. in Petroleum Engineering, Colorado School of Mines

Dr. Sameeh I. Batarseh is a Petroleum Engineering Consultant working with the Production Technology Team of Saudi Aramco's Exploration and Petroleum Engineering Center – Advanced Research Center (EXPEC ARC). Currently, he is the Focus Area Champion of the Unconventional Resources leading the High-Power Laser Program. Sameeh's area of interest is to develop an in situ laser application in drilling, perforation and fracturing, among many other applications with a focus on unconventional reservoirs.

He is an active member of the Society of Petroleum Engineers (SPE), serving the society for several years while holding different positions, including sitting on the SPE Executive Advisory Committee, chairing the Program Committee and serving as session chairman. He was also the board and vice chair for the Western Region USA San Joaquin Valley. Sameeh's service is recognized worldwide as he received the SPE President Section Award of Excellence, Regional Service Award, and is a SPE Distinguished Lecturer. He has organized over 54 SPE technical workshops.

Sameeh has authored or coauthored more than 74 articles with high-impact publications, and has an H-Index of 36. He holds 48 patents (16 granted patents and has 32 patents in progress).

Sameeh received his Ph.D. degree in Petroleum Engineering from the Colorado School of Mines, Golden, CO.

Bander M. Khaldi

B.S. in Business, King Faisal University

Bander M. Khaldi is a Lab Technician working with the Production Technology Team of Saudi Aramco's Exploration and Petroleum Engineering Center – Advanced Research Center (EXPEC ARC). He joined Saudi Aramco in 2008, and began work in the Analytical Support Laboratory Unit in Abqaiq, and later moved to the EXPEC ARC.

Bander's experience includes seven years of work in water and lubricant oil analysis using spectroscopy. In EXPEC ARC, he expanded his interest and work to microwave spectroscopy and thermal analysis. Bander now has two years of experience in characterization with a specialty in spectroscopy.

He received his B.S. degree in Business from King Faisal University, Hofuf, Saudi Arabia.

Low ECD High Performance Invert Emulsion Drilling Fluids: Lab Development and Field Deployment

Dr. Vikrant B. Wagle, Dr. Abdullah S. Al-Yami, Michael O. Onoriode, Jacques Butcher and Dr. Nivika R. Gupta

Abstract /

This article describes the results of the formulation of an acid-soluble low equivalent circulating density (ECD) organoclay-free invert emulsion drilling fluid formulated with acid-soluble manganese tetroxide ($H_2Mn_2O_4$) and a specially designed bridging package. The article also presents a short summary of field applications to date.

The novel non-damaging fluid has superior rheology resulting in a lower ECD, excellent suspension properties for effective hole cleaning, and barite sag resistance while also reducing the risk of a stuck pipe in high overbalance applications.

The 95 pcf high performance invert emulsion fluid (HPIEF) was formulated using an engineered bridging package comprising of acid-soluble bridging agents and an acid-soluble weighting agent viz. $H_2Mn_2O_4$. The article describes the filtration and rheological properties of the HPIEF after hot rolling at 300 °F. Different tests such as contamination testing, sag factor analysis, high-pressure and high temperature rheology measurements, and filter cake breaking studies at 300 °F were performed on the HPIEF. The 95 pcf fluid was also subjected to particle plugging experiments to determine the invasion characteristics and the non-damaging nature of the fluids.

The 95 pcf HPIEF exhibited optimal filtration properties at high overbalance conditions. The low plastic viscosity values and rheological profile support low ECDs while drilling. The static aging tests performed on the 95 pcf HPIEF resulted in a sag factor of less than 0.53, qualifying the inherent stability for expected downhole conditions.

The HPIEF demonstrated resilience to contamination testing with negligible change in properties.

Filter cake breaking experiments performed using a specially designed breaker fluid system gave high filter cake breaking efficiency. Return permeability studies were performed with the HPIEF against a synthetic core material, the results of which confirmed the non-damaging design of the fluid.

The article demonstrates the superior performance of the HPIEF in achieving the desired lab and field performance.

Introduction

An alternative fluid system was required to meet the increasing challenges presented by certain gas producing fields. Wells in these fields have to date been drilled primarily with either formate-based fluids or barite weighted conventional oil-based mud (OBM).

The non-damaging nature of the formate-based fluids have supported the option for an open hole completion design.

The OBM formulations that have extensive applications present the advantage of lower fluid costs and tight filtration characteristics compared to the alternative formate fluids. The conventional OBM fluid systems can present a notable impact on reservoir producibility that can be ascribed in part to the use of barium sulfate weight materials as well as organoclay and organolignite-based additives. Wells drilled with conventional OBM systems are completed with a cased hole completion.

The motivation to develop a high performance invert emulsion fluid (HPIEF) would offer improved drilling performance in maturing fields and the non-damaging nature would present the option to complete wells with an open hole completion design.

In an organoclay-free invert emulsion drilling fluid, the organoclay is replaced by polymeric viscosifiers and the organolignite is replaced by a polymeric filtration control agent. The use of a polymeric viscosifier in the drilling fluid provides a unique gel structure to the drilling fluid, which not only increases the carrying capacity of the cuttings, but also helps to decrease the sag tendency in the fluid[1]. As the organoclay-free invert emulsion fluids are formulated without any organoclay or organolignite, the content of commercial solids in the fluid is low, compared to an organoclay-based equivalent.

The organoclay-free fluids thereby supports a higher rate of penetration as compared to the conventional organoclay-based fluid systems[2]. Another advantage of the organoclay-free invert emulsion drilling fluids is the inherent fragile gel structure[2]. Organoclay-free invert emulsion drilling fluids owing to the reduced solid content show lower plastic viscosity as compared to the organoclay-based drilling fluid[1].

The solids content in the fluid formulation can also be reduced by changing the weight material from barite — 4.2 SG — to higher density materials such as manganese tetroxide ($H_2Mn_2O_4$) — 4.8 SG. The reduced plastic viscosity, owing to the reduced solids content, would further reduce the surge and swab effects, which in turn would help in better equivalent circulating density (ECD) management[3, 4].

A further reason for using $H_2Mn_2O_4$ instead of barite is the acid-soluble nature of $H_2Mn_2O_4$. The acid solubility of $H_2Mn_2O_4$ can be used to remove the filter cake in the wellbore by using any conventional acid treatment. The total acid solubility of the $H_2Mn_2O_4$ weighting agent makes the fluid non-damaging, especially when drilling through reservoir zones. In the event of a stuck pipe incident, conventional acid treatments would break and dissolve the filter cake, reducing the sticking force on the assembly and supporting rapid pipe release[5].

The advantages associated with the organoclay-free drilling fluid formulated with $H_2Mn_2O_4$ present the option for more aggressive well construction designs. A non-damaging, HPIEF with tight filtration characteristics would support drilling through depleted zones with a low risk of differential sticking when compared to the alternative option with formate-based fluid. Longer lateral sections drilled with a non-damaging HPIEF would support higher reservoir production with an open hole completion design.

This article describes the engineering and qualification process for an organoclay-free drilling fluid. The article further summarizes some key performance data based on the application of the fluid system to date.

Design Considerations for an Acid-Soluble HPIEF

Formulation Overview: HPIEF for Reservoir Drilling Applications

The HPIEF discussed in this article will center on acid-soluble 95 pcf fluids.

The HPIEFs were developed based on the following considerations:

- Non-damaging nature of the fluid and acid solubility.
- Slim hole drilling environment with a bottom-hole temperature (BHT) of ~300 °F.
- Long lateral sections where low rates of penetration can be observed.
- High static overbalance conditions, 3,000 psi to 4,500 psi.
- Registered additives and local diesel (base fluid).
- Resilient to potential contaminants and stable over the expected static periods.
- Ease of use for field applications.

The $H_2Mn_2O_4$ was selected as the weight material due to its high density (4.8 SG) and its non-damaging nature. The acid solubility of the $H_2Mn_2O_4$ using conventional acid treatment was confirmed[6].

The HPIEF were formulated with a 70/30 oil-water ratio (OWR) and a water phase salinity of 180,000 ppm to 230,000 ppm.

Formulation Overview: PST Fluids for Completion Applications

The production screen test (PST) fluids were designed for the completion phase. The main objective of the PST fluid was to make sure that there would be no mechanical skin developed on the 4½" sand screen while running the completion into the hole or during the initial well production.

The PST fluids were developed based on the following design criteria:

- Non-damaging nature and acid-soluble.
- Expected BHT of ~300 °F.
- Registered and available additives with a diesel-based fluid.
- Preferred use of the same additives as the HPIEF for compatibility and logistics.
- Non-impairment characteristics to flow through and flow back through the pore sizes of the lower completion.

Formulation of 95 pcf HPIEF and PST Fluids

Two 95 pcf HPIEFs and one 95 pcf PST fluid were developed. The 95 pcf HPIEFs were based on differences in the bridging package for laterals of varying length and overbalance conditions. The longer interval lengths were expected to present higher mechanical attrition of bridging materials, which in turn would impact on the sealing characteristics of the HPIEF. Considering the high overbalance conditions expected in the target fields, tight filtration properties would mitigate the risk of differential sticking.

A single emulsifier provided adequate emulsification of the external phase and wetting of the solids — weight material, bridging material and low gravity solids.

A single polymeric filtration control additive provided the required filtration characteristics with minimal impact on the rheology. Two suspension agents were included in the fluid formulations, with rheology modifier 2 supporting a higher initial gel structure.

Table 1 lists the 95 pcf HPIEF and PST fluid formations.

The 95 pcf HPIEF #1 was developed with an engineered bridging package of various sized ground marbles specifically for short laterals and lower differential pressures. One advantage of the sized ground marble used in the design was that it had higher hardness and tighter modality than regular calcium carbonate. The acid solubility of the sized calcium carbonate bridging

Table 1 *The 95 pcf HPIEF and PST fluid formulations.*

Additive	Function	Unit of Measure	95 pcf HPIEF #1	95 pcf HPIEF #2	95 pcf PST Fluid
Diesel	Base Fluid	bbl/bbl	0.504	0.504	0.537
Emulsifier	Emulsification	lb/bbl	14.0	14.0	14.0
Lime	Alkalinity	lb/bbl	2.5	2.5	2.5
Polymeric Rheology Modifier 1	Suspension	lb/bbl	0.5	0.5	1.0
Polymeric Filtration Control Additive	Filtration Control	lb/bbl	6.0	6.0	—
Water	Internal Phase	bbl/bbl	0.234	0.234	0.231
Calcium Chloride	Shale Inhibition	lb/bbl	29.0	29.0	32.2
Rheology Modifier 2	Suspension	lb/bbl	1.5	1.5	0.5
Manganese Tetraoxide	Weight Material	lb/bbl	215.39	215.39	251.14
Wetting Agent	Wettability	lb/bbl	0.5	0.5	—
Engineered Bridging Material Package 1	Bridging	lb/bbl	40	—	—
Engineered Bridging Material Package 2	Bridging	lb/bbl	—	40	—

package was also an additional benefit of the HPIEF #1 fluid formulation.

An alternative 95 pcf HPIEF #2 fluid formulation, which included sized ground marble, sized resilient graphite and fibers, was developed for longer intervals with higher overbalance conditions. The engineered bridging package of HPIEF #2 was designed for longer laterals where increased mechanical attrition of bridging solids is expected.

The sized resilient graphitic materials used in the HPIEF #2 bridging material package #2 are not acid-soluble. The low concentration and sizing of graphitic materials relative to the permeable test media was considered to present negligible damage potential. The resilient graphitic materials would form an integral part of the external filter cake. The inclusion of a fiber in the bridging material package #2 was considered advantageous due to the higher aspect ratio of fibers relative to the other bridging materials utilized in the bridging package.

The 95 pcf PST fluid formulation detailed in Table 1 included a low concentration of rheology modifiers for the suspension of the micronized weight materials. A low rheological profile was desirable to minimize fluid friction losses during the PST and flow back during production.

Qualification of Acid-Soluble HPIEF: Test Methods, Results and Discussion

HPIEF Mixing Procedure

The HPIEFs were mixed according to the following procedure:

- The HPIEFs were mixed on the Silverson mixer for a total of 60 minutes in a 2-liter stainless steel mixing cup at 6,000 rpm in the order of addition detailed in Table 1.
- The mixed HPIEFs were decanted into aging cells and a 150 psi nitrogen header pressure was applied prior to loading the sealed cells into the roller ovens.
- The HPIEFs were hot rolled for 16 hours at 300 °F.
- After the dynamic aging had been completed, the cells were allowed to cool to an ambient temperature and then depressurized.
- The hot rolled HPIEF were decanted into the mixing cup and then mixed on the Silverson mixer at 6,000 rpm.

HPIEF Laboratory Testing and Evaluation

The candidate HPIEFs were qualified for application based on industry testing standards and procedures (RP API-13 B2). Regain permeability studies were performed at a third party laboratory and are discussed later. The third party laboratory performed a micro-computed tomography (micro-CT) scan analysis on the synthetic core material and is briefly described later.

Acceptance criteria for the fluids' development was determined as part of the project scope.

The HPIEFs were tested and evaluated based on the following tests.

The 95 pcf HPIEF Properties and Contamination Testing

Fluid properties were tested and reported as follows:

- Before hot roll (BHR).
- After hot roll (AHR) — The HPIEFs were conditioned for 16 hours at 300 °F and the fluid properties were determined thereafter.
- After static age (ASA) 24 hours and 48 hours — The 16 hour hot rolled fluids (300 °F) were subject to static aging periods at 300 °F. The static aged fluids were then tested.
- The 16 hour hot rolled HPIEFs were subject to two contamination tests. The HPIEF that had been hot rolled for 16 hours was contaminated with 10% (vol/vol) water and another was contaminated with 35 ppb "Rev Dust" (synthetic drill solids). The contaminated fluids were hot rolled for a further 16 hours at 300 °F before the fluid properties were tested.

Specific fluid properties of the 95 pcf HPIEFs are detailed in Figs. 1 and 2, as well as Tables 2 and 3.

The fluid properties of the 95 pcf HPIEFs are

Fig. 1 *The rheology and gel strengths of the HPIEF #1 (Fann 35 at 150 °F).*

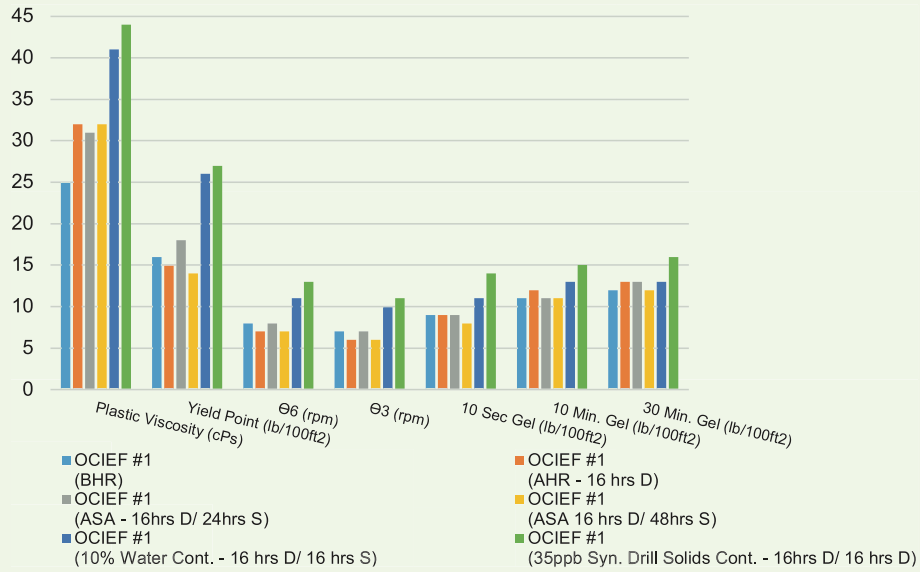

Fig. 2 *The rheology and gel strengths of the HPIEF #2 (Fann 35 at 150 °F).*

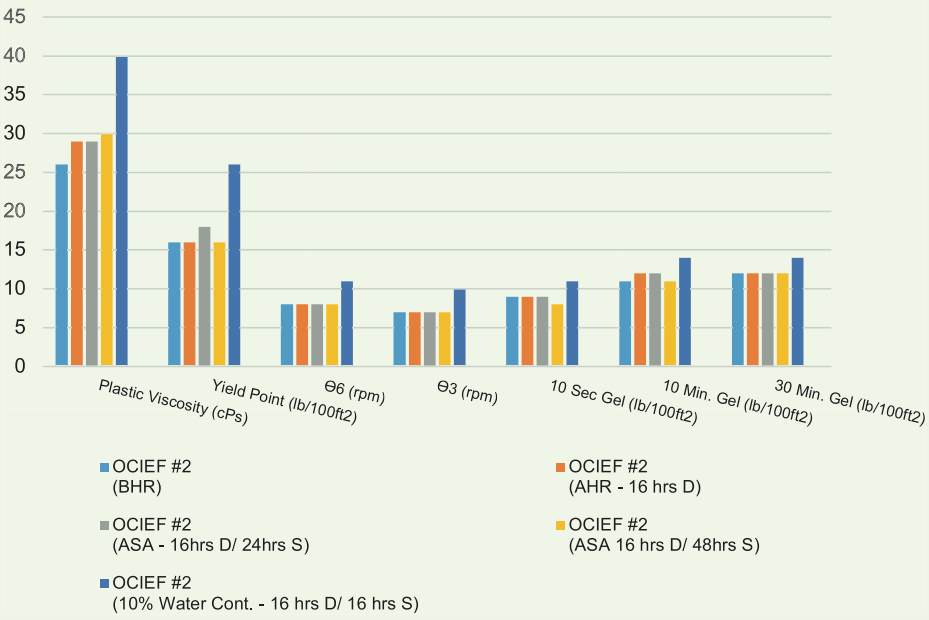

Table 2 *The 95 pcf HPIEFs: Filtration properties at 300 °F.*

Property	Unit of Measure	HPIEF #1 AHR: 16 hrs D	HPIEF #1 ASA: 16 hrs D/24 hrs S	HPIEF #1 ASA: 16 hrs D/48 hrs S	HPIEF #1 10% H_2O Cont. 16 hrs D/16 hrs S	HPIEF #1 35 ppb Syn. Drill Solids 16 hrs D/16 hrs D	HPIEF #2 AHR: 16 hrs D	HPIEF #2 ASA: 16 hrs D/24 hrs S	HPIEF #2 ASA: 16 hrs D/48 hrs S	HPIEF #2 10% H_2O Cont. 16 hrs D/16 hrs S
HPHT Cake	1/32″	2	2	2	2	2	2	2	2	2
HPHT Fluid Loss	ml	2	2.4	1.2	2.4	1.4	2	1.6	2.4	2.4
HPHT Water Breakout	ml	—	—	—	—	—	—	—	—	—
PPA Spurt										
(40 µ, Δ3,000 psi)	ml	0.4	—	—	—	—	1.6	—	—	—
PPA Total										
(40 µ, Δ3,000 psi)	ml	3	—	—	—	—	4.8	—	—	—
PPA Spurt										
(10 µ, Δ3,000 psi)	ml	1	—	—	—	—	0	—	—	—
PPA Total										
(10 µ, Δ3,000 psi)	ml	3.4	—	—	—	—	0.7	—	—	—

Table 3 *The 95 pcf HPIEFs: Stability properties.*

		HPIEF #1 ASA: 16 hrs D/24 hrs S	HPIEF #1 ASA: 16 hrs D/48 hrs S	HPIEF #2 ASA: 16 hrs D/24 hrs S	HPIEF #2 ASA: 16 hrs D/48 hrs S
Free Oil (ml)	ml	0	0	0	0
Top Density	SG	1.47	1.49	1.512	1.522
Bottom Density	SG	1.56	1.579	1.552	1.602
Sag Factor		0.514	0.514	0.507	0.513

discussed in generalized terms as the two formulations are comparable, exclusive of the inert bridging material selection.

Fluid Rheology and Gels

Both the fluid rheology and gel structure are stable across the BHR, AHR, and ASA range as evidenced in Figs. 1 and 2. Low plastic viscosity can be attributed to the size and spherical nature of the micronized weight material, as well as the selection of the emulsifier and the inclusion of polymeric low end rheology modifiers.

The low plastic viscosities observed across the static and dynamic aged fluids infers low circulating pressures in slim hole applications while drilling. The nonprogressive gel structure would minimize surge and swab pressures during tripping operations.

Filtration Characteristics

The filtration characteristics of the HPIEFs are extremely tight as evidenced by low spurt and total filtrate recorded during the particle plugging apparatus (PPA) tests performed at 300 °F with differential pressures of 3,000 psi, Table 2. The performance of

the engineered bridging materials and the polymeric filtration control additive can be confirmed with successful PPA tests on 10 µ and 40 µ aloxite discs.

The validation of the sealing performance against two different permeable media was based on potentially intersecting formations that exhibit heterogeneity in lithology, or potentially wide porosity or permeability ranges. Drilling formations with uncertainties at high overbalance pressure presents the risk of differential sticking events.

Emulsion Stability

The emulsion stability of the HPIEFs is evidenced by the all oil filtrate observed in the high-pressure, high temperature (HPHT) tests performed at 300 °F, Table 2. The lack of free fluid and the low sag factor results can be attributed to the emulsion stability of the formulations. The emulsion stability of the HPIEF is further validated by the fact that there was no free water observed in the HPHT test performed on the 10% water contaminated fluid.

Fluid Stability

The stability of the HPIEFs was evidenced by the low sag factors and lack of free fluid observed during the sag testing on the static aged fluids, Table 3. The 48-hour static fluids did not exhibit thermal gelation tendencies when samples were drawn for the sag tests.

The stability of the 95 pcf HPIEFs can be attributed to the low settling propensity of micronized weight material (Stoke's Law) in combination with the emulsifier and rheology modifiers.

The 10% (vol/vol) water contamination of the 95 pcf HPIEF's increased rheology and gel strengths was a consequence of a larger internal phase and expected reduction in relative solids wetting as indicated in Figs. 1 and 2.

As seen in Table 2, the filtration properties remained tight with HPHT filtrate of 2.4 ml when tested at 300 °F against filter paper. No free water was observed in the filtrate. The 10% water contamination could be treated with additions of Emulsifier 1 and base fluid.

The 95 pcf HPIEF #1 was contaminated with 35 ppb synthetic drill solids (Rev Dust) to simulate contamination by reactive clays as indicated in Fig. 1. The rheology and gel strengths of the solids contaminated 95 pcf HPIEFs increased primarily due to the reactive nature of the sodium montmorillonite addition.

The HPHT filtration characteristics of the solids contaminated HPIEF can be attributed to the higher rheology and cake building nature of the additional colloidal size clay particles. The 35 ppb synthetic drill solids contamination is an extreme solids contamination test for a sandstone reservoir (especially when drilled at high angle).

The elevated rheology and gel strengths resulting from the solids contamination could be treated to within target specifications with a higher OWR pre-mix volume that is inclusive of increased concentrations of Emulsifier 1.

HPHT Rheology of the 95 pcf HPIEFs

The HPHT rheology of the 95 pcf HPIEFs were determined using the Fann 75 HPHT rheometer.

Test temperatures and pressures were determined for the 95 pcf HPIEF #1 and HPIEF #2 based on points of interest in a typical well architecture. The test results are detailed in Table 4 and Table 5, respectively.

The HPHT rheology values are consistent between the 95 pcf HPIEF #1 and the 95 pcf HPIEF #2. There is no significant fluid thickening observed when the

Table 4 *The HPHT rheology of the 95 pcf HPIEF #1.*

		Fann 35	**Fann 75 Testing**								
Temperature	(°F)	**150**	**150**	**150**	**150**	**267**	**267**	**311**	**311**	**331**	**331**
Pressure	(psi)	**0**	**0**	**1,954**	**3,457**	**5,059**	**7,272**	**6,628**	**8,469**	**7,617**	**9,733**
Rheology at 150 °F											
θ600		74	74	88	98	53	61	49	54	48	55
θ300		45	46	51	57	34	38	32	36	31	34
θ200		33	36	40	42	27	30	25	28	25	28
θ100		22	25	28	28	19	20	18	20	19	21
θ6		8	9	10	9	7	7	7	7	8	7
θ3		7	7	7	7	5	5	5	5	6	5
Plastic Viscosity	cP	29	28	37	41	19	23	17	18	17	21
Yield Point	lb/100 ft^2	16	18	14	16	15	15	15	18	14	13

Table 5 *The HPHT rheology of the 95 pcf HPIEF #2.*

		Fann 35	Fann 75 Testing								
Temperature	(°F)	**150**	**150**	**150**	**150**	**267**	**267**	**311**	**311**	**331**	**331**
Pressure	(psi)	**0**	**0**	**1,954**	**3,457**	**5,059**	**7,272**	**6,628**	**8,469**	**7,617**	**9,733**
Rheology at 150 °F											
θ600		79	83	104	115	59	68	52	60	52	57
θ300		47	50	61	68	36	42	33	37	33	35
θ200		36	38	45	50	30	35	28	30	27	29
θ100		23	26	30	32	23	25	20	23	19	20
θ6		7	9	9	9	10	11	7	10	7	8
θ3		6	7	6	7	7	8	5	7	5	5
Plastic Viscosity	cP	32	33	43	47	23	26	19	23	19	22
Yield Point	lb/100 ft^2	15	17	18	21	13	16	14	14	14	13

fluids are subject to varying temperature and pressure regimes. The HPIEFs exhibit satisfactory dynamic suspension characteristics across the range of defined HPHT conditions performed in the tests. The test data indicates that the HPIEF formulations have low inherent ECD potential for the expected application.

Regain Permeability Test of the 95 pcf HPIEF

An extensive regain permeability study was performed on Clashach synthetic core using hot rolled 95 pcf HPIEFs. Formation core samples were not available and the synthetic core material had minerology, porosity, and permeability comparable to the main target formation.

The core samples were 100% saturated in simulated formation brine in a pressure saturator.

The application and drawdown of the 95 pcf HPIEFs were conducted in the following manner:

- A base permeability measurement with (synthetic) formation brine was taken in the formation to the wellbore direction at a low flow rate and with 400 psi confining pressure.
- The core samples were then prepared to irreducible brine saturation using an ultra-centrifuge.
- The core samples were loaded into the HPHT core holders and the effective pressure was gradually increased to 11,420 psi.
- The base effective permeability measurement was taken at 300 °F with 5,300 psi pore pressure and 16,270 psi confining pressure (reservoir conditions) in the formation to the wellbore direction with CO_2 flow at 5 ml/min.
- The HPIEFs were applied dynamically across the wellbore face of the core samples at 4,500 psi overbalance pressure and 3.33 ml/minute for a 24-hour period.
- The drawdown to (simulated) production phase CO_2 was performed by flowing the gas through the sample in the direction of the formation to the wellbore at 5 ml/minute while recording the differential pressure measurements. On completion of the drawdown phase, an effective permeability measurement to CO_2 at residual saturation was made in the formation to the wellbore direction.
- The core samples were removed from the core holders and HPIEF and filter cake remnants were removed from the core face.
- The cores were then reloaded into the test equipment and recalibrated to reservoir conditions (described above). An effective permeability to CO_2 was established in the formation to the wellbore direction.
- The core samples were again unloaded from the core holder and spun down with an ultra-centrifuge.
- The cores were then re-equilibrated to reservoir conditions and an effective permeability to CO_2 at residual saturation was measured in the direction of the formation to the wellbore.

Table 6 summarizes the test results for the 95 pcf HPIEF application and drawdown process.

The low filtrate values recorded at the high overbalance test conditions validates the efficiency of the bridging materials and filter cake building additives within the 95 pcf HPIEFs.

The spin down procedure with the ultra-centrifuge is more representative of radial, long-term production after the back production has swept all the filtrate and solids from the near wellbore area. In both tests there was an almost complete regain in permeability for both the 95 pcf HPIEF #1 and #2.

The only slightly damaging mechanism that caused a

Table 6 *The 95 pcf HPIEFs: Filtration properties at 300 °F.*

Core Sample	Pore Volume	Fluid Applied	Total Filtrate Volume Loss (ml) (Pore Volume)	Base Specific Permeability to Formation Brine Kw (mD)	Base Effective Permeability to CO_2 Kg at Swi (mD)	Effective Permeability to CO_2 after Drawdown Kg at Sr (mD)	Effective Permeability to CO_2 Minus Drilling Mud Cake Kg at Sr (mD)	Effective Permeability to CO_2 After Spindown Kg at Sr (mD) Filtrate Out (ml)
V3	2.873	95 pcf HPIEF #1	1.383 (0.440)	98.6	91.6	36.5 (-60.2%)	37.0 (-59.6%)	88.7 (-3.17%) [0.65]
V14	3.046	95 pcf HPIEF #2	1.648 (0.574)	131	129	70.4 (-45.4%)	83.0 (-35.7%)	126 (-2.33%) [0.40]

reduction in permeability was the residual filtrate and solids that blocked some pore spaces in the wellbore face side of the core samples.

The 95 pcf HPIEF #2 does have marginally better final regain permeability — and higher regain permeability after drawdown and after cake removal — than the 95 pcf HPIEF #1.

Micro-CT Scan of Synthetic Core Material

The 2D and 3D micro-CT scan analysis was performed on the Clashach core (V3) before and after the coreflood experiment.

The 2D micro-CT scan image, Fig. 3a, indicated that within the subsampled region of the wellbore end of the core sample exposed to 95 pcf HPIEF #1, the filtrate (white colored areas) invaded just the first few pore spaces to a depth of ~1 mm from the wellbore face after spin down. The (black) low intensity features represent pore spaces in the core sample. The (light) high X-ray intensity features represent high density grains or patches of cementation.

The observation of low invasion is also shown by the 3D visualization of the invaded filtrate in Fig. 3b. The image indicates the spatial distribution of filtrate invasion (blue). Note that the rock matrix (with different CT values) has been removed in this image but the white boundary lines indicates the core sample outline.

The micro-CT scan supports the results of the regain permeability study and tight filtration characteristics of the 95 pcf HPIEFs.

Acid Solubility of Filter Cake

Filter cake breaking studies were performed on the 95 pcf HPIEFs. The study was performed with different acid formulations with a view to achieving optimal filter cake removal efficiency. The following procedure

Fig. 3 *The (a) 2D and (b) 3D micro-CT scan of the core sample after spin down (95 pcf HPIEF #1).*

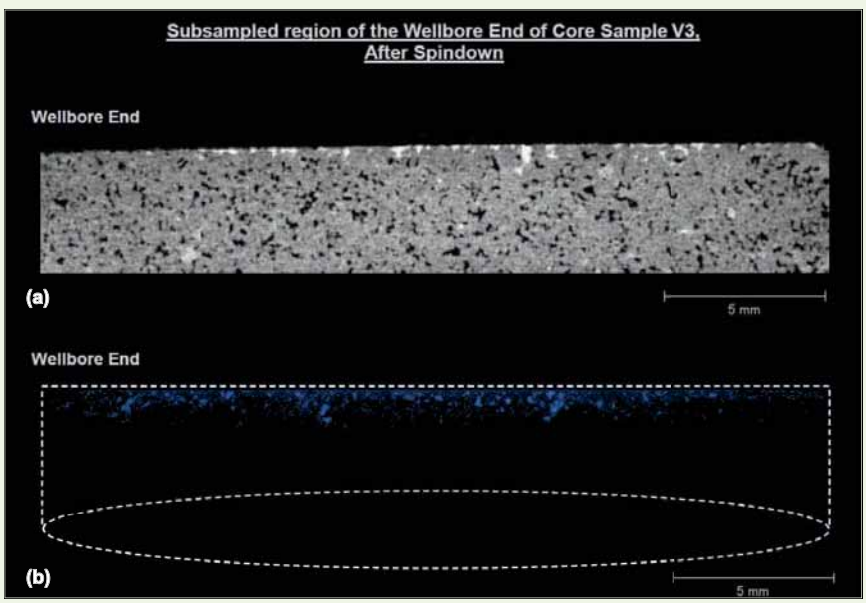

was applied to the cake dissolution study.

1. Filter cake formation with HPHT apparatus:
   - The weight of a dry 55 µ aloxite disc was initially measured before saturating in diesel for 10 minutes.
   - A HPHT filtration test was performed on the 95 pcf HPIEF #1 against a 55 µ aloxite disc (300 °F, Δ500 psi) for 30 minutes.
   - After completing the HPHT test, the aloxite disc (with filter cake) was carefully removed from the test apparatus and weighed.
2. The application of acid treatment soaks to dissolve the filter cake:
   - The 55 µ aloxite disc with the filter cake was placed back into the HPHT cell.
   - A 100 ml acid treatment fluid was poured slowly into the cell and onto the filter cake.
   - The HPHT cell was then subsequently shut-in for 24 hours at 300 °F with 200 psi nitrogen header pressure.
   - After 24 hours of shut-in, the acid soak test was stopped and the cell was allowed to cool-down.
   - The 55 µ aloxite was subsequently removed from the HPHT cell and weighed.
   - The filter cake removal efficiency of the acid treatment fluid was then calculated taking into account the weight of the filter cake before and after the experiment.

Two different acid treatment fluids were used to determine the filter cake removal efficiency against the 95 pcf HPIEF #1. The formulation of both acid treatment fluids are detailed in Table 7. The acid treatment formulated with a combination of 1% (w/w) HCl acid and 9% formic acid resulted in a filter cake removal efficiency of 85%. A second acid treatment fluid with a combination of 2% (w/w) HCl acid and 9% formic acid had a filter cake removal efficiency of 94.5%.

The acid treatment fluids demonstrated high filter cake efficiency against the 95 pcf HPIEF filter cake.

Figure 4 shows the effect of acid treatment fluid #1 on the 95 pcf HPIEF #1 filter cake at 300 °F, (a) before, and (b) after.

Figure 5 shows the effect of acid treatment fluid #2 on the 95 pcf HPIEF #1 filter cake at 300 °F, (a) before, and (b) after.

PST Fluids Mixing Procedure

The PST fluids were mixed according to the following procedure:

- The PST fluids were mixed on the Silverson mixer

Fig. 4 *The effect of acid treatment fluid #1 on the 95 pcf HPIEF #1 filter cake at 300 °F.*

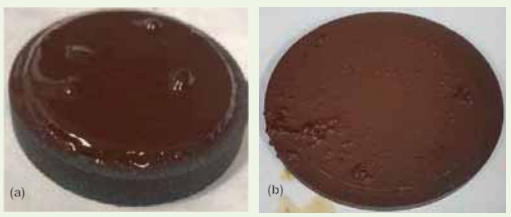

Fig. 5 *The effect of acid treatment fluid #2 on the 95 pcf HPIEF #1 filter cake at 300 °F.*

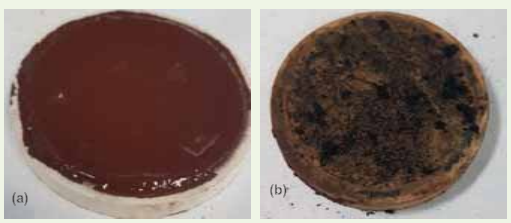

Table 7 *The two acid treatments and removal efficiencies.*

	Acid Treatment #1	Acid Treatment #2
Water	141.8 ml	141.8 ml
HCl Acid	1 wt%	2 wt%
Formic Acid	9 wt%	9 wt%
Mutual Solvent	10 vol%	10 vol%
Water Wetting Surfactant	0.2 vol%	0.2 vol%
Corrosion Inhibitor	2.5 vol%	2.5 vol%
Intensifier 1	4 vol%	4 vol%
Intensifier 2	4 vol%	4 vol%
Filter Cake Removal Efficiency	85%	94.45%

for 60 minutes at 6,500 rpm. A water bath was used as a heat sink.

- The PST additives were mixed according to the sequence indicated in Table 2.
- The PST fluid was mixed for a further 60 minutes on the Silverson mixer at 6,500 rpm to simulate the effect of extended shearing time expected during field application.

PST Laboratory Testing and Evaluation

The PST fluids were tested according to RP API-13 B2 and company PST test procedures. Select properties were evaluated as follows:

- The density, rheology, and gel strengths were determined on fresh mixed PST fluid (BHR) as well as a sample of the PST fluid contaminated with 50 ppb sized ground marble (simulated bridging solids contamination arising from inefficient displacement). The solids were mixed into the PST fluid for 10 minutes on the Silverson mixer at 6,500 rpm.
- PST testing was performed on 5 × 1 liter samples of PST fluid against 250 µ screen coupons with 10 psi header pressure.
- A PST test was performed on the contaminated PST fluid. The PST test was performed against a 250 µ screen with a 10 psi header pressure.

The 95 pcf PST fluids were tested and recorded properties are detailed in Fig. 6.

The 95 pcf PST Fluid Properties and Contamination Testing

The 95 pcf PST fluid exhibited appropriate rheology and gel strength values for the intended application. The 95 pcf PST fluid was contaminated with 50 ppb bridging solids and mixed as previously mentioned. After the addition of solids to the PST fluid density, the rheologies and gel strengths increased as expected.

PST Test Results

The results of the PST test detailed in Fig. 7 confirms that the fluid formulation does not blind the 250 µ screen coupons. The full test volume of 5 × 1 liter PST fluid passed through the same screen coupon at a comparable time. When the screen coupon was recovered from the cell there was no residual buildup on the face of the coupon, Fig. 8.

A PST test was also performed on contaminated PST fluid — 50 ppb bridging materials. The complete PST test was stopped after 3 × 1 liter samples had passed through the 250 µ screen coupon as the flow through times were comparable to the PST fluid.

Summary of Field Experience

The HPIEFs have seen extensive use since the fluids were first developed, with 24 applications to date. Wells drilled with HPIEF in this period have been applied in 10 different fields and in both vertical and horizontal 5⅞" slim hole well designs.

The drilling performance with HPIEFs has been satisfactory and there have been no stuck events during drilling or completion operations. The HPIEFs have to date been used for a number of high overbalance applications, Fig. 9.

The wells drilled with HPIEF have resulted in a reduction in invisible lost time when compared to wells drilled with formate fluids. The practice of performing

Fig. 6 The test results of the 95 pcf PST fluids and recorded properties.

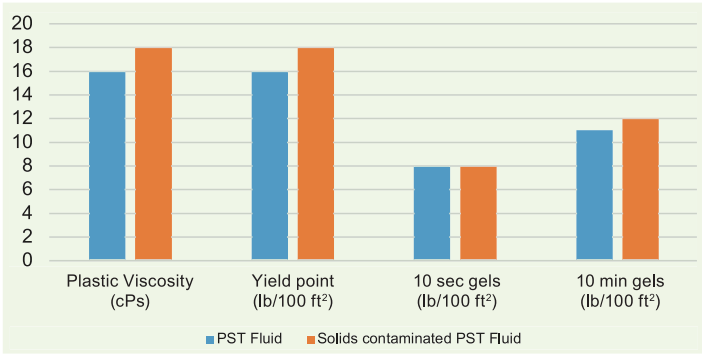

Fig. 7 The PST test results.

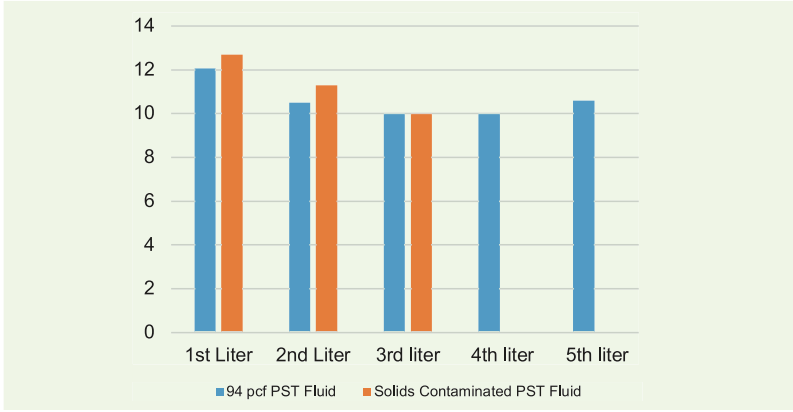

Fig. 8 The 250 µ screen after PST, showing no residual buildup on the face of the coupon.

Fig. 9 *The static overbalance of HPIEF wells drilled.*

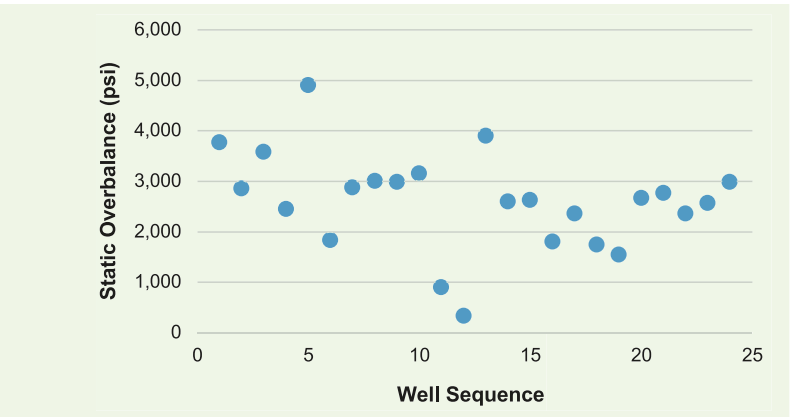

reaming trips (12-24 hour duration) on wells drilled with formate fluids have been eliminated on wells drilled with HPIEF. There have been no instances of hole problems attributable to fluids drilled with HPIEF.

The HPIEF properties have been maintained within target specifications on the referenced wells. There have been no instances of fluid properties impeding drilling or completion operations, e.g., sag, or high viscosity fluid. Compliance with fluid property targets also validates the fluid system's ease of use in the field.

The HPIEF formulations deployed in the field have been customized for each specific well application utilizing the fluid additives from the qualified 95 pcf HPIEFs. The subtle differences between fluid formulations deployed to date have centered predominantly on density and the bridging/sealing additives and properties. The HPIEF densities have ranged from 75 pcf to 100 pcf.

The 24 wells that have been drilled with HPIEF have been assessed on a fluids cost/well basis and compared to the equivalent volume of formate fluids — same density. The average fluids cost per well drilled with HPIEF is 41% lower than drilling with formate fluids.

Production from all wells drilled with HPIEF have exceeded expectations validating the fluid's non-damaging design and the successful deployment thereof.

Conclusions

The formulation of the HPIEF has proven that reservoirs can be safely drilled with non-damaging fluids at high overbalance. The combination of bridging materials and polymeric fluid loss additives has provided the required mitigation to the risk of differential sticking. The utility of the HPIEF design can support drilling longer laterals with the potential for higher mud weights if so required.

The use of a high-pressure shearing unit at the rig site proved to be useful when preparing initial fresh HPIEFs. As HPIEF volumes have increased in the field and liquid mud plant since the initial deployment, there has been a reduced reliance on the shearing unit to support fluid mixing.

There have been no instances of notable contamination to the HPIEFs, which can be attributed to prudent fluid engineering practices at the rig location.

The approach for developing PST compliant fluids has evolved since the HPIEF and PST fluids were initially deployed in the field. PST fluids were initially prepared with fresh mixed fluids. Over time, the PST fluids have been developed using active HPIEFs and a refinement of operational practices. The benefits of using — PST compliant — HPIEFs for displacing into the open hole includes lower cost and fluid volumes handled as well as lower conditioning time.

The acid solubility of the filter cake has been evidenced in the article. Acid treatment has not been required to release the pipe during drilling or completion operations.

Acknowledgments

This article was prepared for presentation at the SPE/IADC Middle East Drilling Technology Conference and Exhibition, Abu Dhabi, UAE, May 25-27, 2021.

References

1. Carbajal, D.L., Burress, C.N., Shumway, W. and Zhang, Y.: "Combining Proven Anti-Sag Technologies for HPHT North Sea Applications: Clay-Free Oil-Based Fluid and Synthetic, Sub-Micron Weight Material," SPE paper 119378, presented at the SPE/IADC Drilling Conference and Exhibition, Amsterdam, the Netherlands, March 17-19, 2009.

2. Burrows, K., Carbajal, D.L., Kirsner, J. and Owen, B.: "Benchmark Performance: Zero Barite Sag and Significantly Reduced Downhole Losses with the Industry's First Clay-Free Synthetic-Based Fluid," SPE paper 87138, presented at the IADC/SPE Drilling Conference, Dallas, Texas, March 2-4, 2004.

3. Nicora, L.F., Pirovano, P., Blomberg, N. and Taugbol, K.: "High-Density Invert Emulsion System with Very Low Solids Content to Drill ERD and HPHT Wells," SPE paper 65000, presented at the SPE International Symposium on Oil Field Chemistry, Houston, Texas, February 13-16, 2001.

4. Wagle, V.B., Al-Yami, A.S., AlAbdullatif, Z., Bubshait, A.S., et al.: "Mitigation of Stuck Pipe Challenges in HTHP Conditions Using Acid Soluble Blend of Barite and Manganese Tetroxide as Weighting Materials for Drilling Fluids," SPE paper 175844, presented at the SPE North Africa Technical Conference and Exhibition, Cairo, Egypt, September 14-16, 2015.

5. Montgomery, J.K., Keller, S.R., Krahel, N. and Smith, M.V.: "Improved Method for Use of Chelation to Free Stuck Pipe and Enhance Treatment of Lost Returns," SPE paper 105567, presented at the SPE/IADC Drilling Conference, Amsterdam, the Netherlands, February 20-22, 2007.

6. Wagle, V.B., Al-Yami, A.S., AlAbdullatif, Z., Bubshait, A.S., et al.: "Operational Benefits of Designing Acid-Soluble Drilling Fluids for Horizontal Wells in HTHP Conditions," SPE paper 178214, presented at the SPE/IADC Middle East Drilling Technology Conference and Exhibition, Abu Dhabi, UAE, January 26-28, 2016.

About the Authors

Dr. Vikrant B. Wagle

Ph.D. in Surfactant and Colloidal Science,
Mumbai University Institute of Chemical Technology

Dr. Vikrant B. Wagle is a Petroleum Scientist with the Drilling Technology Team of Saudi Aramco's Exploration and Petroleum Engineering Center – Advanced Research Center (EXPEC ARC). His experience revolves around the design of novel, environmentally friendly drilling fluid additives and the development of high-pressure, high temperature tolerant drilling fluid systems.

Vikrant has 45 technical publications and 83 granted U.S. patents, and he has filed several other U.S. patent applications, all in the area of drilling fluids, cementing, and loss circulation.

He received his M.S. degree in Chemistry from the University of Mumbai, Mumbai, India, and his Ph.D. degree in Surfactant and Colloidal Science from the Mumbai University Institute of Chemical Technology, Mumbai, India.

Dr. Abdullah S. Al-Yami

Ph.D. in Petroleum Engineering,
Texas A&M University

Dr. Abdullah S. Al-Yami is a Petroleum Engineer with the Drilling Technology Team of Saudi Aramco's Exploration and Petroleum Engineering Center – Advanced Research Center (EXPEC ARC). He has 18 years of experience with Saudi Aramco and previously worked in different positions, including as a Lab Scientist and Drilling Engineer, conducting research related to drilling engineering.

Abdullah has received several awards during his career, including Saudi Aramco's Research and Development Center (R&DC) Innovation Award and its Successful Field Application Award for his research work. He also received Saudi Aramco's EXPEC ARC Effective Publications Award. A member of the Society of Petroleum of Engineers (SPE), Abdullah was awarded the 2009 SPE Outstanding Technical Editor Award for his work on the SPE *Drilling and Completion Journal*. He also received the 2014 SPE Regional (Middle East, North Africa and South Asia) Drilling Engineering Award, and both the 2015 and 2016 CEO Saudi Aramco Excellence Award. In 2016, Abdullah received Oil & Gas Middle East Award "highly commended" recognition in the category of internal control valve (ICV) Strategy of the Year for his efforts in developing drilling products utilizing a local resources strategy. In 2017, he was awarded the Saudi Arabian Board of Engineering Award.

Abdullah is a coauthor of the textbook *Underbalanced Drilling: Limits and Extremes*; he has 82 granted U.S. patents and 129 filed patents; and has more than 80 publications to his credit, all in the area of drilling and completions.

Abdullah received his B.S. degree in Chemistry from Florida Institute of Technology, Melbourne, FL; his M.S. degree in Petroleum Engineering from King Fahd University of Petroleum and Minerals (KFUPM), Dhahran, Saudi Arabia; and his Ph.D. degree in Petroleum Engineering from Texas A&M University, College Station, TX.

Michael O. Onoriode

B.S. in Chemical Engineering,
University of Lagos

Michael O. Onoriode is working as a Petroleum Engineer with the Drilling Fluids Support Team of Saudi Aramco's Exploration and Petroleum Engineering Center – Advanced Research Center (EXPEC ARC).

His experience is centered on the design, deployment, and implementation of novel environmentally friendly drilling and completion fluids for high-pressure, high temperature wells.

Michael received his B.S. degree in Chemical Engineering from the University of Lagos, Lagos, Nigeria.

Jacques Butcher

MBA,
Bradford University

Jacques Butcher worked as an Industrial Engineer in the automotive industry before joining Halliburton Baroid as a Mud Engineer in 2001. He is currently working in Dubai as the Baroid Regional Technical Manager.

Jacques has worked in various field and operational positions with Baroid in West Africa, Asia Pacific, and Latin America. He has also held technical positions within the drilling and completion fluids discipline in Asia Pacific, and recently in Saudi Arabia.

Jacques received his MBA degree from University of Bradford, Bradford, West Yorkshire, U.K.

Dr. Nivika R. Gupta

Ph.D. in Polymer Science,
National Chemical Laboratory

Dr. Nivika R. Gupta is a Senior Scientist-Chemist working for Baroid at Halliburton's Technology Centre in Pune, India. She joined Halliburton R&D in 2013 and has worked on the development of new drilling and completion fluid technologies. Nivika has also provided technical service for fluids technology deployment.

She has coauthored several publications and filed several patents.

In 2013, Nivika received her Ph.D. degree in Polymer Science from the National Chemical Laboratory, Pune, India.

Self-Destructive Barite Filter Cake in Water-Based and Oil-Based Drilling Fluids

Zeeshan Tariq, Dr. Muhammad S. Kamal, Dr. Mohamed Mahmoud, and Ayman R. Al-Nakhli

Abstract /

The complete removal of filter cake containing barium sulfate ($BaSO_4$) is a challenging and difficult task because of the involvement of various issues, such as incompatibility and insolubility. Conventional filter cake removal techniques include the use of chelating agents and are ineffective in completely removing the barite filter cakes. Barite is completely insoluble in water as well as in various acids, such as acetic acid, lactic acid, hydrochloric (HCl) acid, and formic acid.

In this study, a novel method is introduced to remove the $BaSO_4$ filter cake by introducing a new formulation of both oil-based mud (OBM) and water-based mud (WBM). The new formulation can self-destruct the $BaSO_4$ filter cake formed with OBM and WBMs. The new formulation is comprised of encapsulated thermochemical fluids in addition to the conventional additives. These thermochemical fluids can cause a strongly exothermic reaction that can significantly increase the temperature and pressure. The generated heat and pressure can dissolve or dislodge the filter cake.

The performance of the proposed formulation to self-destruct the filter cake was evaluated using a filter press cell. The results showed that the new formulation can completely remove the filter cake in a single stage within 48 hours. The new formulation can be used as a promising formula to remove the filter cake before the cementing operation.

Introduction

Among the various objectives of the drilling fluids, one of them is to keep the formation pressure under control by adding various weighing materials. During the drilling operation, the permeable formations allow only the liquid from the drilling fluids to penetrate inside them leaving behind a layer of residue or solid particles called filter cake or mud cake.

This mud cake forms on the face of the porous and permeable media and is typically highly impermeable in nature[1]. The permeability of filter cake usually lies between 0.01 mD to 100 nD[2]. From the perspective of drilling, this filter cake has several advantages, e.g., it controls further drilling fluid loss and mitigates solid invasion in the formation, which ultimately prevents formation damage[3].

Formation damage is less significant and critical in vertical wells than in inclined and horizontal wells. Horizontal wells are exposed to the drilling fluid for longer periods compared to vertical wells[4]. On the other hand, in terms of an oil well casing cementing operation and reservoir production perspectives, this filter cake has various disadvantages. Before a cementing operation, if the filter cake is left untreated, it will cause the debonding of the cement between the casing and the formation.

During production, if the filter cake is left untreated, it stops or minimizes the production of oil and gas from permeable formations into the wellbore. Therefore, the removal of filter cake during or after the drilling operation is necessary.

Barite is the most common weighting material in drilling fluid formulations. Therefore, the resulting filter cake consists of mainly barite particles. Barite has poor solubility in water and acids such as acetic acid, hydrochloric (HCl) acid, and formic acid. Barite is partially soluble in chelating agents, which includes ethylene-diamine-tetra-acetic acid (EDTA). The formation of the filter cake on the face of the permeable formation highly depends on several parameters of drilling fluids such as the weightage of solid particles, the composition, rheology, additives, differential pressure, and formation mineralogy[5].

Weighting materials are the main constituent of the drilling fluids[6]. The whole filter cake removal program focused on the dissolution of the weighting material. The filter cake removal program can be done in two different steps. In the first step, breaking of the polymer coat is achieved, and the second stage is for the dissolution of the weighting materials[7].

Simultaneous removal of mud cake and the inhibition of formation damage in carbonate formations with HCl acid is a very expensive and challenging task, especially in a horizontal well. This can be attributed to the fact that because of the fast reaction, the consumption of acid will be very high. The tortuosity in the horizontal section and the difficulty of selecting an appropriate location for acid placement cause additional

efforts[8]. The following reaction can happen when HCl acid reacts with carbonate rocks.

$$CaCO_3 + 2HCl \rightarrow CaCl_2 + H_2O \quad (1)$$

Tjon-Joe-Pin et al. (1993)[9] used polymer specific enzymes to remove the damage caused by polymers in drilling, completion, and workover fluids. They conducted core flooding experiments and found a significant increase in permeability after the deployment of biotechnology-based polymer enzymes. Acids and oxidizers can attack the active sites on polymer strands, the polymer backbone does not react with acids leading to partial degradation of the polymer strands[10].

Mahadi et al. (2014)[11] used a new acid precursor (ester) of an organic acid to remove filter cake. According to this study, field applications have shown that filter cake can be removed using an acid precursor.

Howard et al. (2016)[12] studied barite solubility in potassium and cesium formate brines in both buffered and unbuffered solutions. They found that the barite solubility in formate brines is 3,500 mg/L at 100 °C. They showed that in the buffered formate by bicarbonate/carbonate, the solubility of barium sulfate ($BaSO_4$) is very low because the dissolved barium will convert to barium carbonate ($BaCO_3$). The resulting $BaCO_3$ is soluble in the concentrated formate brines. They showed that in the buffered potassium formate brine, potassium sulfate and $BaCO_3$ will precipitate.

Many factors, such as the oil type, co-surfactant, surfactant, salinity, and temperature, affect the behavior of the microemulsion phase. In addition, because the drilled wells are not identical, each well requires a specific design and the performance of the microemulsion fluid must be confirmed in the laboratory before implementation in the field[13]. Bourrel et al. (1982)[14] stated that the microstructure of a microemulsion should be characterized to determine its potential as a breaker fluid.

Many researchers have investigated the microstructures of the microemulsions[15]. They concluded that the characterization of microemulsions is difficult because of their complexity, the presence of a variety of structures, and the components involved in building the microstructures.

Jiao and Sharma (1992)[16] studied the impact of formation damage with oil-based mud (OBM) in horizontal wells. They tested new fluids to remove the filter cake formed with OBM. Davison et al. (2001)[17] studied the formation damage associated with OBM and water-based mud (WBM). They studied the effect of bentonite concentration, polymer additive concentration, the degree of flocculation, and the particles in drilling fluids.

The efficiency of the removal of oil-based barite filter cake using current technologies is less than 60%[18]. This can be attributed to the following; low barite solubility, the complexity of the filter cake constituents, and the presence of an oil coat. In this study, new formulations that can be implemented in a single-stage or a multistage approach was introduced. The new formulation contains barite solids removers in addition to oil dissolvers.

Elkatatny and Nasr-El-Din (2012)[19] have shown the successful implementation of a two-stage removal of filter cake using polylactic acid and enzymes. In their previous study[20], the filter cake formed with calcium carbonate-based drilling fluid in a single-stage using glutamic diacetic acid was removed. The removal of filter cake containing $BaSO_4$ or barite is a challenging and difficult task because of the involvement of incompatibility and solubility issues. Conventional removal treatments comprised of chelating agents and HCl acid were ineffective in completely removing the barite filter cakes. Barite is completely insoluble in water as well as in various acids such as acetic acid, HCl acid, and formic acid[21]. Barite is partially soluble in chelating agents, which includes pentetic acid and EDTA[22].

In this work, encapsulated thermochemical fluids were used in drilling formulations that can self-destruct the filter cake. The key objective of this study is to formulate new OBM and WBM, and evaluate the efficiency of the encapsulated thermochemical fluids in the removal of the formed filter cake.

Thermochemical Fluids Application in the Petroleum Industry

Upon reaction, the thermochemical fluids can cause a strongly exothermic reaction which simultaneously generates pressure and heat. For the past few years, the petroleum industry has witnessed a large number of thermochemical fluid applications in different areas. The first application of a thermochemical reaction in the petroleum industry appeared in 1986 when it was used to dissolve the paraffin waxes from the tubing of producing wells. Khalil et al. (1994)[23] used thermochemical fluids to dissolve paraffin deposited in subsea production lines.

Amin et al. (2007)[24] found a huge increment in the production profiles of the wells treated with thermochemical fluids for wax and organic scale removal. Al-Nakhli (2015)[25] used thermochemical fluids to enhance the stimulated reservoir volume (SRV) by in situ generation of the localized pressure and temperature. They found that due to chemically induced pressure pulses, the SRV increases tremendously.

Wang et al. (2018)[26] used thermochemical fluids for the first time in the application of enhanced oil recovery. They generated the in situ foams by mixing surfactants with thermochemical fluids, and then carried out oil recovery experiments using a coreflooding setup.

Through their experiments, they reported a 20% to 34% increment in oil recovery. The other areas of petroleum engineering where thermochemical reactions have been investigated include thermochemical fracturing[27, 28], wax removal[29], paraffin removal[23], filter cake removal[30], organic scale removal[24], foam flooding by mixing thermochemical fluids with surfactants[26], heavy oil recovery[31], sludge removal[32], stimulated reservoir volume enhancement[25, 33], and in situ steam generation[34].

Materials and Experiments

Materials

Table 1 shows the new and old WBM formulations, which are implemented in this study. Distilled water was used as a base fluid in both the old and new formulations. The old formulation refers to the conventional drilling fluid system commonly used in the industry. The new formulation of the drilling fluid is comprised of the two types of encapsulated thermochemical fluids. In both formulations, barite particles were the main constituent of the drilling fluid system.

Barite particles weighing 278 g out of the total solids' weight (552 g to 566 g) comprised of weightage of 50% of the total solids. Xanthan gum (XC polymer) was added in the system to improve the cutting transportation and rheology of the drilling fluids. This were also added to avoid filtrate loss[35]. Xanthan gum is a polysaccharide discharged by the bacteria called Xanthomonas campestris.

It is the calcium, potassium, and sodium salt of a higher molecular weight polysaccharide. These polysaccharides contain d-glucuronic, d-glucose, and d-mannose acid. It is completely soluble in water and has a color of the cream powder. It contains at least 1.5% of pyruvic acid. The caustic soda was added in both the new and old formulations to maintain the pH of the drilling fluid. Calcium carbonate with two different micron-sized particles was used as a bridging agent. Sodium chloride (NaCl) was used as a clay stabilization additive.

Hydroxypropyl starch, which is a derivative of natural starch, was added in both the new and old formulations of the drilling fluid system to avoid fluid loss. They are nonionic and can only be affected by hardness and salinity of the fluids. In the new formulation, the amount of encapsulated thermochemical fluids added was 8.5 g and 5.5 g. The encapsulated size of the pills was between 25 and 50 microns.

Diesel was used as a base fluid in both the old and new formulations of OBM. An emulsifier is a chemical added in both the new and old formulations to lower the oil/water interfacial tension. This ensured the formation of stable and small drops. Calcium chloride ($CaCl_2$) was used as a clay stabilization additive in both the new and old formulations. In the new formulations of OBM, the amount of encapsulated thermochemical fluids added was 8.5 g and 5.5 g. The encapsulated size of the pills was between 25 and 50 microns.

Thermochemical Fluids

In this study, the thermochemical fluids used were comprised of salts of nitrogen such as sodium nitrite ($NaNO_2$) and ammonium chloride (NH_4Cl). The two reagents were used in the proportion of one to one. The solution mixture was prepared at ambient temperature and pressure conditions. When one mole of $NaNO_2$ reacts with one mole of NH_4Cl, a strong exothermic chemical reaction happens, and NaCl, water (steam), and nitrogen gas can be released. The release of nitrogen gas can become the reason for high-pressure generation. The thermochemical reaction can be defined by Eqn. 2.

$$NH_4Cl + NaNO_2 \rightarrow [NH_4NO_2 + NaCl.NH_4NO_2\ Themolabile] \rightarrow NaCl + 2H_2O + N_2\ (gas) + \Delta H\ (heat) \quad (2)$$

This reaction resulted in the generation of a reaction intermediate product called "Themolabile," which immediately transformed into NaCl (brine), nitrogen gas, and steam.

Experimental

The rheology of drilling fluids' rheology was evaluated using a GRACE viscometer (Model M3600). The

Table 1 The WBM formulations used in this study.

Additives	Chemical Formula	Old Formation	New Formulation	Units
Distilled Water	H_2O	241.5	241.5	cm^3
Xanthomonas Campestris (XC) Polymer (xanthan gum)		1	1	g
Caustic Soda	NaOH	0.25	0.25	g
Sodium Chloride	NaCl	22	22	g
Starch (hydroxypropyl)	$C_6H_5O_{10}$	4	4	g
Calcium Carbonate (25 micron)	$CaCO_3$	3	3	g
Calcium Carbonate (38 micron)	$CaCO_3$	3	3	g
Barite (60 microns)	$BaSO_4$	278	278	g
Encapsulated TCFA (25 to 50 microns)	$NH_4Cl + NaNO_2$	0	5.5	g
Encapsulated TCFB (25 to 50 microns)	$NH_4Cl + NaNO_2$	0	8.5	g

reaction kinetics were evaluated using an autoclave reactor. To create and remove the filter cake using the old and new formulations, the high-pressure, high temperature (HPHT) API static filter press apparatus was used. The tests were conducted at a pressure difference of 200 psi and at ambient temperature.

The size of the ceramic disk on which the filter cake formed was 25 microns. Figure 1 is a diagram of the HPHT API filter press. Four different experiments were performed, two for the old formulation and two for the encapsulated thermochemical fluids with the new formulation.

The new formulations were comprised of encapsulated thermochemical fluids. To evaluate the efficiency of the proposed formulations, the HPHT filtration setup was used. The filter cake was placed in a HPHT cell and heated up to 100 °C for 48 hours soaking time. The differential pressure of 200 psi was applied.

Results and Discussions

Reaction Kinetics

Reaction kinetics of thermochemical fluids were investigated and the reaction parameters such as enthalpy change, thermal conductivity, and specific heat capacity were determined. These parameters were determined to produce the thermal energy required to dissolve filter cake formed with WBM and OBMs. This reaction can generate a temperature of up to 371 °C and pressure up to 3,500 psi.

Figure 2 shows the pressure generation profile from the thermochemical reactions, after necessary modifications to the available ratio. This figure essentially shows that increasing the molar concentration of the reactants could enhance the pressure generation. The thermochemical reaction was initiated by preheating a cell to 100 °C. This generated pressure pulse from the release of nitrogen gas was logged in an aging cell with a capacity of 20 cc.

Figure 3 shows the sensitivity of the initial reservoir temperature on the reaction time. The initial reservoir temperature was varied between 50 °C to 100 °C. As shown in the figure, the reaction time of thermochemical fluids is a strong function of an initial reservoir temperature.

Rheological Properties of Drilling Fluids

In Fig. 4, the major properties of the WBM are shown, and in Fig. 5, the major properties of the OBM are shown. The basic drilling fluid properties measured were density, plastic viscosity, yield point, 10 s gel strength, 10 min gel strength, and pH.

From the analysis of Figs. 4 and 5, it can be observed that the basic drilling fluid properties were not affected by the new formulation of drilling fluids. The microencapsulated thermochemical fluids did not affect the rheology of the drilling fluid, therefore, encapsulated thermochemical fluids can be considered compatible with the drilling fluid ingredients and did not have a significant effect on the properties of the drilling fluid.

Fig. 1 *A diagram of the HPHT API filter press.*

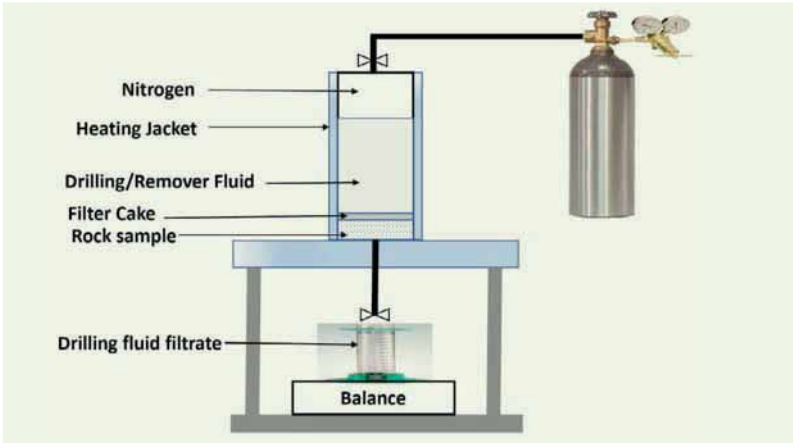

Fig. 2 *The effect of a reactant molar concentration on the pressure pulse generation due to thermochemical fluids.*

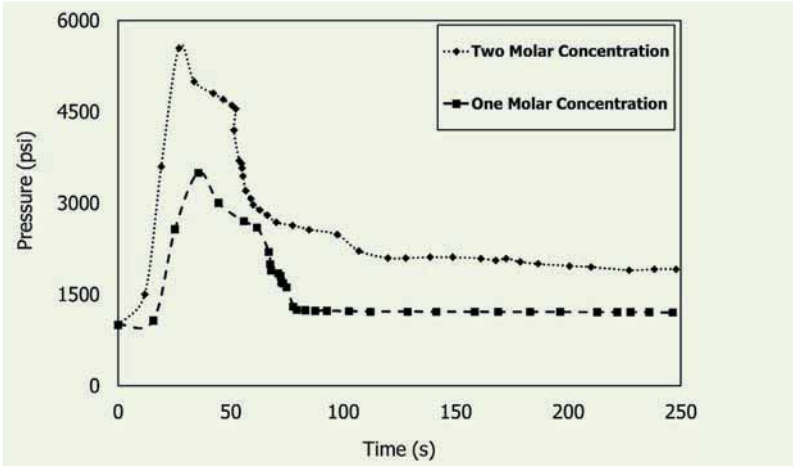

Fig. 3 *The time required to achieve maximum temperature as a function of reservoir temperature.*

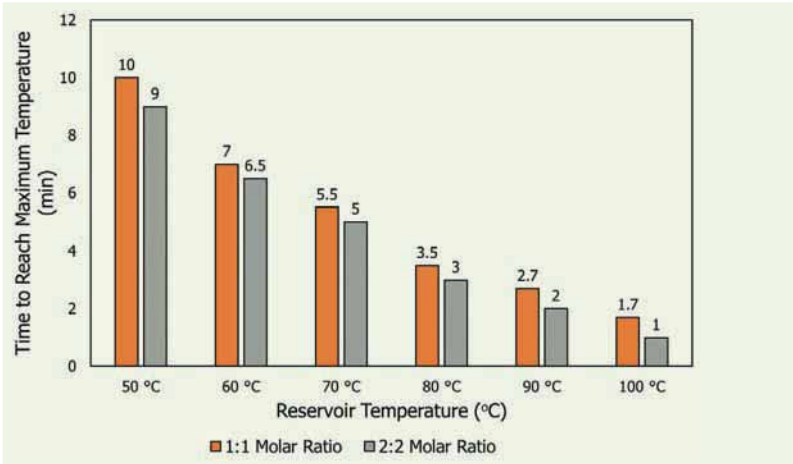

Fig. 4 *The WBM properties with the old and new formulations.*

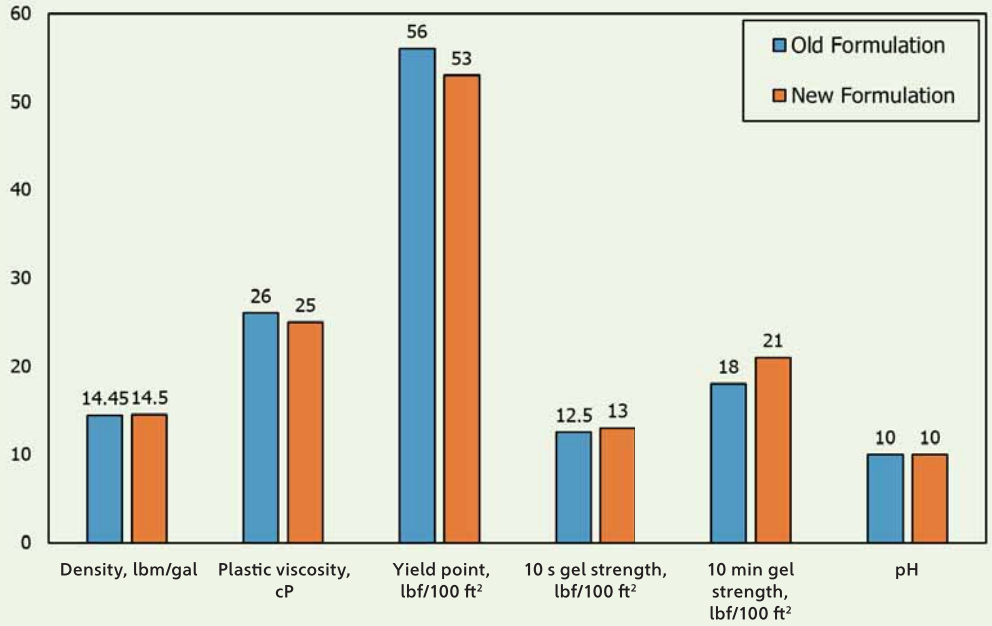

Fig. 5 *The OBM properties with the old and new formulations.*

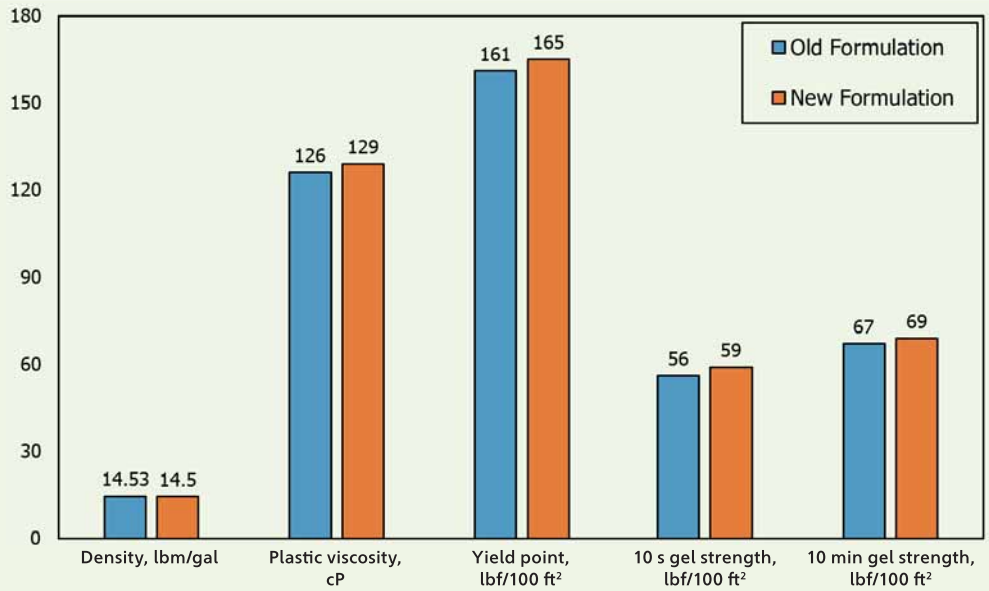

API Static Filtration Experiments

API static filtration experiments were conducted using a Fann filter press apparatus for all the new and old formulations. Figure 6 shows the filtration performances of both the new and old formulations of WBM on a ceramic disk. Results shown are for a standard test time of 30 minutes. The WBM with the old formulation yielded a total filtrate volume of 9.7 cm^3. The filter cake formed on a ceramic disc with a thickness of 1.3 mm. The WBM with a new formulation yielded a filtrate volume of 9.5 cm^3. The filter cake that formed on a ceramic disk was 1.2 mm thick.

Figure 7 shows the filtration performances of both the new and old formulations of the OBM. The old formulation of the OBM resulted in the filtrate loss of 5.1 cm^3, while the new formulation of the OBM

Fig. 6 *The filtration performances of both the new and old formulations of WBM on a ceramic disk.*

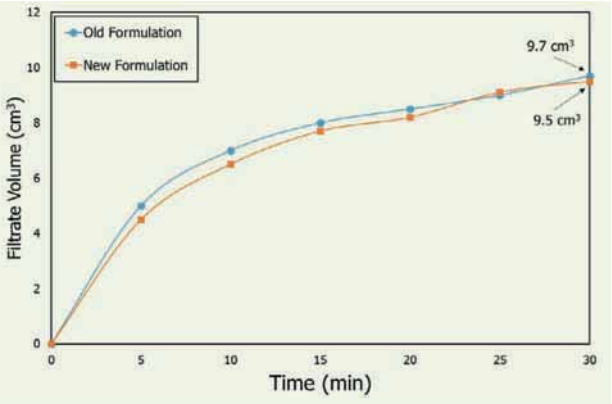

Fig. 7 *The filtration performances of both the new and old formulations of the OBM.*

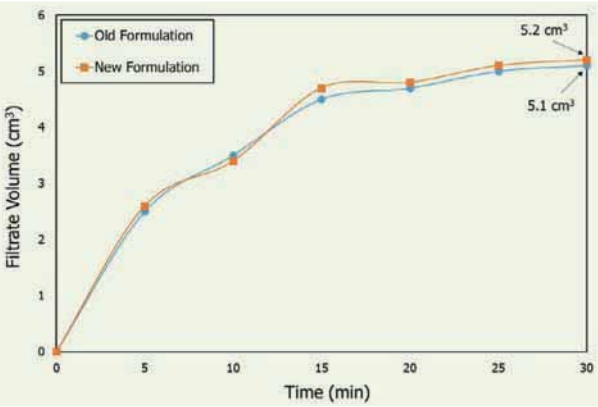

resulted in the filtrate loss of 5.2 cm^3. The filtration of the new formulations in both OBM and WBM were almost identical with the original formulations without the encapsulated thermochemical fluids. This can be attributed to the plugging efficiency of the micro-sized capsules. The addition of the encapsulated thermochemical fluids in micro-size acted as a plugging agent and prevented the drilling fluid filtration to the rock. The ratio used in this study can be optimized based on the formation rock pore throat distribution. The capsule size of the thermochemical fluids should be comparable with the formation rock pore throat size distribution.

Figure 8 shows the filter cake formed using the old and new formulation of the WBM. The removal efficiency in the case of WBM was 70%, by taking the weight difference between the original weight and final weight of the filter cake. This confirmed that the encapsulated thermochemical fluids was an integral part of the filter cake and once the reaction took place, the generated pressure and temperature disturbed the filter cake and removed the majority of the solids to be the bulk of the drilling fluid. In the case of real field operations, the efficiency is expected to be higher because the encapsulated thermochemical fluids that invaded the formation — once they react — will generate very high pressure that will push back most of the solids remaining from the filter cake.

Figure 9 shows the filter cake in the case of the OBM. The removal efficiency in the case of the OBM reached 85%. This is expected in the OBM because the generated temperature, in addition to the very high generated pressure, will dissolve the oil from the filter cake to the bulk of the drilling fluid. In the case of field conditions, this efficiency is expected to be higher because of the generated pressure and temperature from the encapsulated thermochemical fluids that invaded the formation.

Figure 10 compares the filter cake thickness formed with the old and new formulation of both the WBM and OBMs. The thickness of the filter cake formed with the old conventional WBM was 1.7 mm, and with the new formulation, because of self-destruction, it was 0.45 mm. Similarly, in the case of the OBM with the old conventional drilling fluids, the filter cake formed on a ceramic disk had a thickness of 1.3 mm, while with the new formulation the filter cake formed with a thickness of 0.25 mm.

Figure 11 shows the stability time of the encapsulated thermochemical fluids and the generation of pressure and temperature, due to a strongly exothermic reaction. The stability time of the encapsulated thermochemical fluids was 48 hours. For a normal drilling operation,

Fig. 8 *Filter cake formed with WBMs: (a) The old formulation, and (b) The new formulation.*

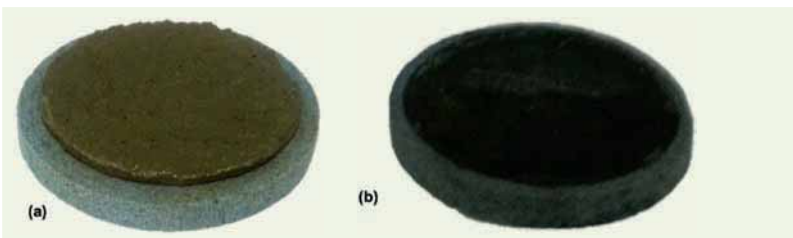

Fig. 9 *The filter cake formed with OBMs: (a) The old formulation, and (b) The new formulation.*

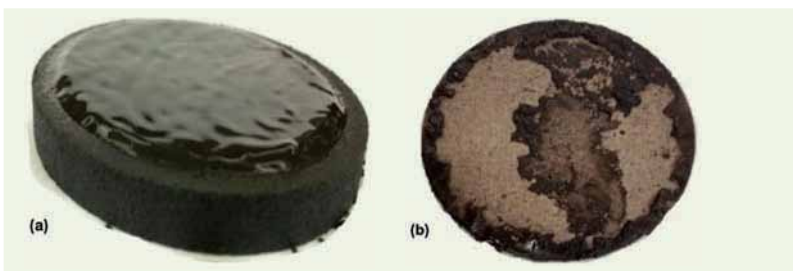

Fig. 10 *The comparison of filter cake thickness with the old and new formulation of WBM and OBMs.*

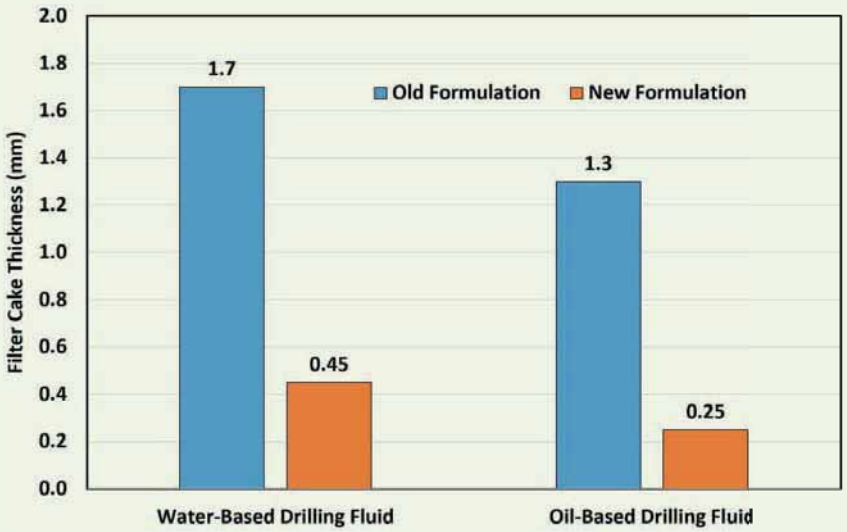

at least 48 hours are needed for the trip in and trip out before moving into cementing operations. After 48 hours, the strongly exothermic reaction was initiated, and the thermochemical fluids reacted. Upon reaction, the pressure increased from 200 psi to 1,100 psi.

The temperature increased from 100 °C to 180 °C. The capsules were stable almost for 2 days, therefore they can be compared with the reaction of the thermochemical fluids without encapsulation as well.

Figure 12 shows the generated pressure and temperature for the same thermochemical fluids used in the capsules. The temperature of the reactor was 100 °C, the reaction took place in less than 2 minutes, compared to the 2 days for the encapsulated thermochemical fluids. The generated pressure and temperature is comparable with that obtained in the case of the encapsulated thermochemical fluids.

Conclusions

The following major conclusions can be drawn from the discussion:

1. The new formulation for both the OBM and WBM comprised of encapsulated thermochemical fluids are developed.

Fig. 11 *The pressure and temperature generation from the encapsulated thermochemical fluids.*

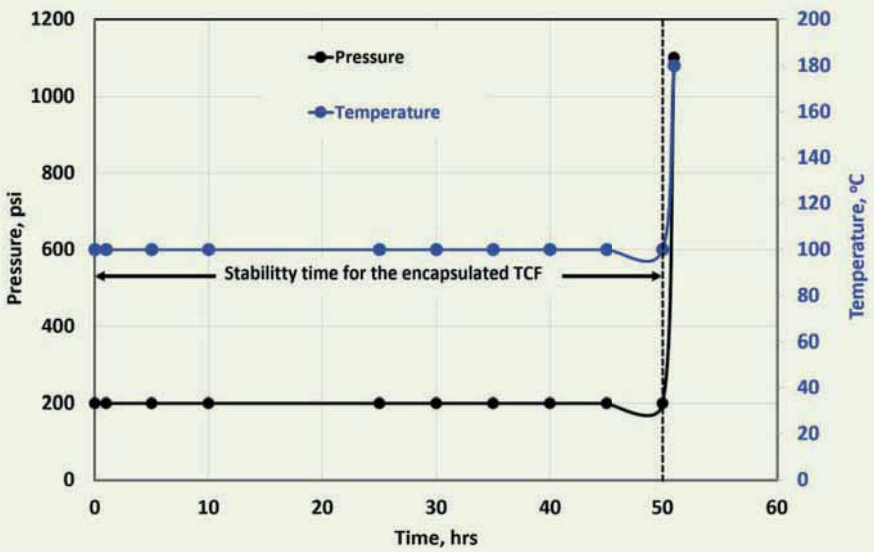

Fig. 12 *The pressure and temperature generated from the thermochemical fluids.*

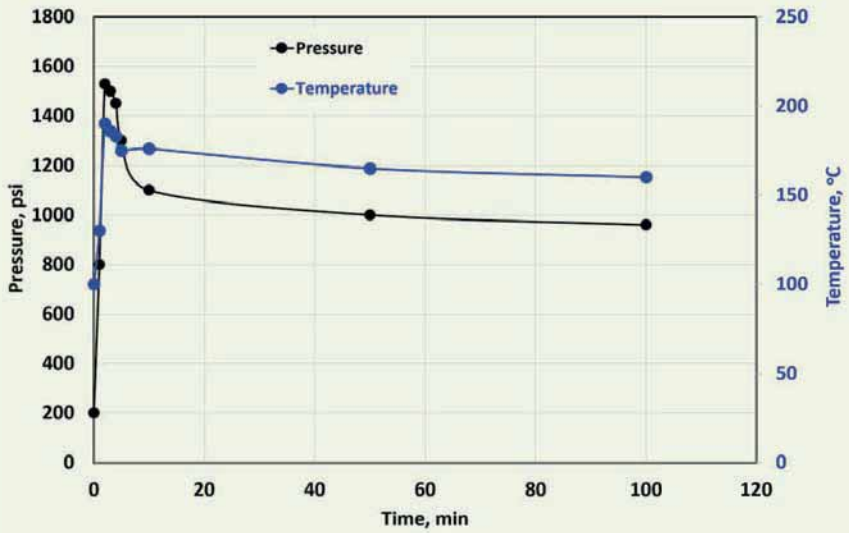

2. The new formulation resulted in the self-destruction of the filter cake formed with both OBM and WBM.
3. The thickness of the filter cake formed was 0.6 mm and 0.5 mm with the new formulation of the WBM and the OBM, while with the old formulation the thicknesses were 1.7 mm and 1.3 mm, respectively.
4. The stability time for the encapsulated thermochemical fluids was enough to carry auxiliary drilling events before the well completion.

References

1. Civan, F.: "A Multiphase Mud Filtrate Invasion and Wellbore Filter Cake Formation Model," SPE paper 28709, presented at the International Petroleum Conference and Exhibition of Mexico, Veracruz, Mexico, October 10-13, 1994.
2. Hanssen, J.E., Jiang, P., Pedersen, H.H. and Jørgensen, J.F.: "New Enzyme Process for Downhole Cleanup of Reservoir Drilling Fluid Filter Cake," SPE paper 50709, presented at the SPE International Symposium on Oil Field Chemistry, Houston, Texas, February 16-19, 1999.
3. Bageri, B.S., Mahmoud, M.A., Al-Mutairi, S.H., Kuwait, C., et al.: "Filter Cake Porosity and Permeability Profile along the Horizontal Well and Their Impact on Filter Cake Removal," IPTC paper 18465, presented at the International Petroleum Technology Conference, Doha, Qatar, December 6-9, 2015.
4. Frick, T.P. and Economides, M.J.: "Horizontal Well Damage Characterization and Removal," *SPE Production and Facilities*, Vol. 8, Issue 1, February 1993, pp. 15-22.
5. Bageri, B.S., Al-Mutairi, S.H. and Mahmoud, M.A.: "Different Techniques for Characterizing the Filter Cake," SPE paper 163960, presented at the SPE Unconventional Gas Conference and Exhibition, Muscat, Oman, January 28-30, 2013.
6. Caenn, R. and Chillingar, G.V.: "Drilling Fluids: State-of-the-Art," *Journal of Petroleum Science and Engineering*, Vol. 14, Issues 3-4, May 1996, pp. 221-230.
7. Mahmoud, M.A. and Elkatatny, S.: "Removal of Barite Scale and Barite Weighted Water — or Oil-Based Drilling Fluid Residue in a Single Stage," *SPE Drilling and Completion*, Vol. 34, Issue 1, March 2019, pp. 16-26.
8. Parlar, M., Tibbles, R.J., Chang, F.F., Fu, D., et al.: "Laboratory Development of a Novel, Simultaneous Cake Cleanup and Gravel Packing System for Long, Highly Deviated or Horizontal Open Hole Completions," SPE paper 50651, presented at the European Petroleum Conference, the Hague, the Netherlands, October 20-22, 1998.
9. Tjon-Joe-Pin, R., Brannon, H.D. and Rickards, A.R.: "Remedial Treatment for Polymeric Damage Removal Provides Improved Well Productivity," SPE paper 25214, presented at the SPE International Symposium on Oil Field Chemistry, New Orleans, Louisiana, March 2-5, 1993.
10. Brannon, H.D.: "Biotechnological Breakthrough Improves Performance of Moderate to High Temperature Fracturing Applications," SPE paper 28513, presented at the SPE Annual Technical Conference and Exhibition, New Orleans, Louisiana, September 25-28, 1994.
11. Mahadi, K.A., Nizam, M.I., Jadid, M.B., Ogbonna, C., et al.: "Use of Acid Precursor as Alternative to Acid Treatment to Drill-in Fluid Filter Cake Removal: FN Case Study," IPTC paper 17713, presented at the International Petroleum Technology Conference, Kuala Lumpur, Malaysia, December 10-12, 2014.
12. Howard, S., Anderson, Z. and Parker, S.: "Solubility of Barium Sulfate in Formate Brines — New Insight into Solubility Levels and Reaction Mechanisms," SPE paper 179021, presented at the SPE International Conference and Exhibition on Formation Damage Control, Lafayette, Louisiana, February 24-26, 2016.
13. Brege, J.J., El Sherbeny, W., Quintero, L. and Jones, T.A.: "Using Microemulsion Technology to Remove Oil-Based Mud in Wellbore Displacement and Remediation Applications," SPE paper 150237, presented at the North Africa Technical Conference and Exhibition, Cairo, Egypt, February 20-22, 2012.

14. Bourrel, M., Chambu, C., Schechter, R.S. and Wade, W.H.: "The Topology of Phase Boundaries," *SPE Journal*, Vol. 22, Issue 1, February 1982, pp. 28-36.

15. Graciaa, A., Lachaise, J., Cucuphat, C., Bourrel, M., et al.: "Interfacial Segregation of an Ethyl Oleate/Hexadecane Oil Mixture in Microemulsion Systems," *Langmuir*, Vol. 9, Issue 6, June 1993, pp. 1473-1478.

16. Jiao, D. and Sharma, M.M.: "Formation Damage due to Static and Dynamic Filtration of Water-Based Muds," SPE paper 23823, presented at the SPE Formation Damage Control Symposium, Lafayette, Louisiana, February 26-27, 1992.

17. Davison, J.M., Jones, M., Shuchart, C.E. and Gerard, C.: "Oil-Based Muds for Reservoir Drilling: Their Performance and Cleanup Characteristics," *SPE Drilling and Completion*, Vol. 16, Issue 2, June 2001, pp. 127-134.

18. Nasr-El-Din, H.A., Al-Mutairi, S.H., Al-Hajji, H.H. and Lynn, J.D.: "Evaluation of a New Barite Dissolver: Lab Studies," SPE paper 86501, presented at the SPE International Symposium and Exhibition on Formation Damage Control, Lafayette, Louisiana, February 18-20, 2004.

19. Elkatatny, S.M. and Nasr-El-Din, H.A.: "Removal Efficiency of Water-Based Drill-in Fluid Filter Cake Using Polylactic Acid," SPE paper 154192, presented at the SPE EUROPEC/EAGE Annual Conference and Exhibition, Copenhagen, Denmark, June 4-7, 2012.

20. Elkatatny, S.M. and Nasr-El-Din, H.A.: "Removal of Water-Based Filter Cake and Stimulation of the Formation in One Step Using an Environmentally Friendly Chelating Agent," *International Journal of Oil, Gas and Coal Technology*, Vol. 7, Issue 2, 2014, pp. 169-181.

21. Lakatos, I., Lakatos-Szabó, J. and Kosztin, B.: "Optimization of Barite Dissolvers by Organic Acids and pH Regulation," SPE paper 74667, presented at the International Symposium on Oil Field Scale, Aberdeen, Scotland, U.K., January 30-31, 2002.

22. Al Otaibi, M.B., Nasr-El-Din, H.A. and Hill, A.D.: "Characteristics and Removal of Filter Cake Formed by Formate-Based Drilling Mud," SPE paper 112427, presented at the SPE International Symposium and Exhibition on Formation Damage Control, Lafayette, Louisiana, February 13-15, 2008.

23. Khalil, C.N., Neumann, L.F., Linard, C.A. and Santos, I.G.: "Thermochemical Process to Remove Paraffin Deposits in Subsea Production Lines," OTC paper 7575, presented at the Offshore Technology Conference, Houston, Texas, May 2-5, 1994.

24. Amin, R.A.M., Halim, N., Rosli, K.A., Ali, M.I., et al.: "Production Profile of Wells Before and After Treatment Using a Novel Thermochemical Technique," SPE paper 107663, presented at the European Formation Damage Conference, Scheveningen, the Netherlands, May 30-June 1, 2007.

25. Al-Nakhli, A.R.: "Chemically Induced Pressure Pulse: A New Fracturing Technology for Unconventional Reservoirs," SPE paper 172551, presented at the SPE Middle East Oil and Gas Show and Conference, Manama, Kingdom of Bahrain, March 8-11, 2015.

26. Wang, F., Chen, H., Alzobaidi, S. and Li, Z.: "Application and Mechanisms of Self-Generated Heat Foam for Enhanced Oil Recovery," *Energy & Fuels*, Vol. 32, Issue 9, August 2018, pp. 9093-9105.

27. Tariq, Z., Mahmoud, M.A., Abdulraheem, A., Al-Nakhli, A.R., et al.: "An Experimental Study to Reduce the Fracture Pressure of High Strength Rocks Using a Novel Thermochemical Fracturing Approach," *Geofluids*, Vol. 2019, August 2019, pp. 1-16.

28. Tariq, Z., Mahmoud, M., Abdulraheem, A., Al-Nakhli, A.R., et al.: "An Experimental Study to Reduce the Breakdown Pressure of the Unconventional Carbonate Rock by Cyclic Injection of Thermochemical Fluids," *Journal of Petroleum Science and Engineering*, Vol. 187, April 2020.

29. Rocha, N.O., Khalil, C.N., Leite, L.F. and Bastos, R.M.: "A Thermochemical Process for Wax Damage Removal," SPE paper 80266, presented at the International Symposium on Oil Field Chemistry, Houston, Texas, February 5-7, 2003.

30. Mahmoud, M.: "Well Clean-Up Using a Combined Thermochemical/Chelating Agent Fluids," *Journal of Energy Resources Technology*, Vol. 141, Issue 10, October 2019.

31. Alade, O.S., Mahmoud, M., Hassan, A., Al-Shehri, D., et al.: "Evaluation of Kinetics and Energetics of Thermochemical Fluids for Enhanced Recovery of Heavy Oil and Liquid Condensate," *Energy & Fuels*, Vol. 33, Issue 6, April 2019, pp. 5538-5543.

32. Rocha, N.O., Khalil, C.N., Leite, L.F. and Goja Ferrira, A.M.: "Thermochemical Process to Remove Sludge from Storage Tanks," SPE paper 105765, presented at the International Symposium on Oil Field Chemistry, Houston, Texas, February 28-March 2, 2007.

33. Al-Nakhli, A.R., BaTaweel, M., Mustafa, A., Tariq, Z., et al.: "Novel Methodology to Reduce the Strength of High Stress-Tight Gas Reservoirs Using Thermochemical," paper presented at the 53rd U.S. Rock Mechanics/Geomechanics Symposium, New York City, New York, June 23-26, 2019.

34. Mahmoud, M., Alade, O.S., Hamdy, M., Patil, S., et al.: "In Situ Steam and Nitrogen Gas Generation by Thermochemical Fluid Injection: A New Approach for Heavy Oil Recovery," *Energy Conversion and Management*, Vol. 202, December 2019.

35. Kameda, E., de Queiroz Neto, J.C., Langone, M.A.P. and Coelho, M.A.Z.: "Removal of Polymeric Filter Cake in Petroleum Wells: A Study of Commercial Amylase Stability," *Journal of Petroleum Science and Engineering*, Vol. 59, Issues 3-4, November 2007, pp. 263-270.

About the Authors

Dr. Zeeshan Tariq

Ph.D. in Petroleum Engineering, King Fahd University of Petroleum and Minerals

Dr. Zeeshan Tariq is an Associate Professor working at the King Fahd University of Petroleum and Minerals (KFUPM). His areas of research interests are geomechanics, hydraulic fracturing, artificial intelligence, and petrophysics.

Zeeshan has published more than 20 peer-reviewed journal articles and filed several patents.

He is an active member of various societies, such as the Society of Petroleum Engineers (SPE), the Society of Petrophysicists and Well Log Analysts (SPWLA), the Society of Exploration Geophysicists (SEG), and the American Rock Mechanics Association (ARMA).

Zeeshan received his M.S. degree in Petroleum Engineering from KFUPM, Dhahran, Saudi Arabia. He received his Ph.D. degree at the College of Petroleum Engineering and Geosciences, KFUPM.

Dr. Muhammad S. Kamal

Ph.D. in Chemical Engineering, King Fahd University of Petroleum and Minerals

Dr. Muhammad S. Kamal is working as a Research Engineer (Associate Professor) at the Center for Integrative Petroleum Research (CIPR) at King Fahd University of Petroleum and Minerals (KFUPM).

In 2015, he joined CIPR as a Research Engineer, where he focuses on several aspects of oil field chemistry, including but not limited to chemical enhanced oil recovery, rheology of complex fluids, water-soluble polymers, drilling fluids, and interfacial phenomenon. Muhammad also contributed to developing the fluid lab at CIPR, and manages this lab as a lab manager.

He is a technical reviewer for several prestigious journals. Muhammad is the author of several publications on the subject of oil field chemistry.

In 2010, he received his M.S. degree in Polymer and Process Engineering from the University of Engineering and Technology, Lahore, Pakistan.

Muhammad received his Ph.D. degree in Chemical Engineering from KFUPM, Dhahran, Saudi Arabia, in 2015.

Dr. Mohamed Mahmoud

Ph.D. in Petroleum Engineering, Texas A&M University

Dr. Mohamed Mahmoud is an Associate Professor working in the Petroleum Engineering Department with King Fahd University of Petroleum and Minerals (KFUPM), Dhahran, Saudi Arabia. Prior to assuming this position in 2016, he had been a Research Assistant in the same department since 2008.

From 2004 to 2008, Mohamed worked as a Petroleum Engineer at Belayim Petroleum Co. in Egypt. During the period from 2001 to 2004, he was a Drilling Engineer at Magawish Petroleum Co., Egypt.

Mohamed's research interests are varied and cover several subjects, including well simulation, enhanced oil recovery, and multiphase flow in vertical and horizontal wells.

He received his Ph.D. degree in Petroleum Engineering from Texas A&M University, College Station, TX, in 2011.

Ayman R. Al-Nakhli

M.S. in Entrepreneurship for New Business Development, Open University Malaysia

Ayman R. Al-Nakhli is a Petroleum Scientist in Saudi Aramco's Exploration and Petroleum Engineering Center – Advanced Research Center (EXPEC ARC), where he leads the research program on thermochemicals and develops technologies related to conventional and unconventional reservoirs such as pulse fracturing, stimulation, diverting agents, and heavy oil.

Ayman has developed and field deployed several novel technologies, with four of them being commercialized with international service companies. He received the World Oil Award for Best Production Chemical in 2015.

Ayman has filed more than 20 patents, published 35 journal papers, and 40 conference papers.

He received his B.S. degree in Industrial Chemistry from King Fahd University of Petroleum and Minerals (KFUPM), Dhahran, Saudi Arabia, and an M.S. degree in Entrepreneurship for New Business Development from Open University Malaysia, Bahrain.

Modeling of Deep Polymer Gel Conformance Treatments Using Machine Learning

Mohammed A. Alghazal and Prof. Turgay Ertekin

Abstract /

Polymer gel technologies have been widely employed in conformance control applications to improve sweep and recovery from high permeability reservoirs. Modeling of polymer gel propagation, gelation time, and adsorption in the porous media requires a complex full-order computation of diffusivity equations, heat transfer, and chemical reactions for components partitioning in oleic and aqueous phases. This article presents a soft computing alternative and data-driven approach to using machine learning to model deep polymer gel treatments in fractured reservoirs.

Reference simulation models of various dual permeability systems were used to generate the data set for the machine learning model, an artificial neural network (ANN). A second-order reaction scheme for gel formulation was used to describe the chemical reaction between the polymer, polyacrylamide, and the crosslinker component, chromium acetate. Viscosities, adsorption properties and residual resistance factors of the polymer and produced gel were populated based on experimental data. Various conformance design factors and reservoir properties were parameterized for inclusion in the neural network, including temperature, injection rate, gel concentration, bottom-hole pressure, drainage radius, porosity, fracture spacing, and permeability.

Feature analysis of the input variables indicated that 10 parameters are sufficient to train the model and predict the performance of the conformance treatment with indicators, including the oil and water rate profiles' improvement after applying the polymer gel treatment. The data set was randomly divided into 80% training, 10% validation, and 10% testing sets.

Early stopping and monitoring of the validation and testing set's errors were used to generalize the solution and enhance the performance of the neural network. Hyperparameter tuning showed that using a deep multiple hidden layer neural network was more effective than increasing the neurons in a single hidden layer. The weights and biases of the model were adjusted using a mean squared error (MSE) loss function and a gradient descent optimizer.

A correlation of 90% was achieved for the test samples with a mean absolute deviation of less than 10% for all modeled variables. The developed neural network model was able to reduce the complexity of the full-order simulation model by accurately predicting the performance of polymer gel treatments in fractured reservoirs at a speed 200 times faster than commercial simulators with only 10 input variables of polymer gel design and reservoir properties.

This work presents a unique surrogate modeling approach based on machine learning to describe complex polymer gel kinetics and flow dynamics in deep conformance applications. The presented neural network model can be used to robustly predict the oil recovery performance of polymer gel treatments in fractured reservoirs outperforming commercial simulators in terms of computational complexity and processing speed.

Introduction

Polymer gel treatments are commonly used in the industry to mitigate sweep conformance problems in highly fractured reservoirs. There are essentially two types of polymers used in the application of polymer flooding: (1) partially hydrolyzed poly-acrylamides, and (2) biopolymer or xanthan gum[1, 2]. Partially hydrolyzed poly-acrylamides is most commonly used for conformance treatment processes due to its ability to adsorb on the rock surface and its economic feasibility compared to biopolymers[2].

Polymer solutions are mixed with a crosslinking agent to form an in situ polymer gel that can be used to treat common reservoir conformance problems[3]. Such a gel system is often referred to as Cr(III)-carboxylate/acrylamide polymer[4]. The Cr(III)-carboxylate/acrylamide polymer gels can be selectively injected within the region between the injectors and producers to selectively treat and plug fractures with high permeability anomalies to improve sweep efficiency and oil recovery from the producible matrix[4].

Modeling of polymer gel propagation, gelation time, and adsorption in the porous media requires a complex

full-order computation of diffusivity equations, heat transfer, and chemical reactions for components partitioning in oleic and aqueous phases. Scott et al. (1987)[5] provides one of the earliest techniques attempted to describe in situ gel calculations in reservoir simulation. Chemical reaction and heat transfer terms are incorporated with the mass and energy balance equations to solve for the changes in saturation, pressure and temperature per component at each time step inside the simulator.

There are at least five fluid components that interact inside the reservoir media in polymer gel applications, including oil, water, polymer, crosslinker, and the formulated gel. All, but the oil, are typically assumed to be partitioning in aqueous phases. Retention, adsorption and permeability reduction properties for the gel components also need to be computed inside the simulator along the reaction module. Full-order computation of these modules inside chemical simulators are both sophisticated and time-consuming. Simultaneously solving these diffusivity and chemical reaction equations in a simulation model with hundreds of cells may take up to several minutes to hours to converge.

Surrogate data-driven models based on machine learning can be used to approximate the solutions of the reservoir simulator by reducing its complexity and computational time. In supervised machine learning, several statistical and probabilistic models can be used to map the relation between a certain set of features to a target variable.

This target can be either a discrete label or a continuous variable, separating two types of common machine learning problems, classification and regression models. Classic machine learning algorithms, including decision trees, support vector machines, Naïve Bayes, and regression models, are capable of solving both regression and classification problems. Ensemble methods are also popular models combining one or more learning algorithms to improve the prediction of base estimators, i.e., decision trees[6].

In general, these classical models and learning algorithms require handcrafted features to generate a strong inference model. Additionally, such classic algorithms are limited to commonly predicting a single target variable, mapping a set of features, or multiple input parameters, to a single target variable, or output. In other regression problems, where more than one target variable is required to be predicted, multiple output regression or multivariate target models can be used.

There are two methods that can be used to model these complex problems in classic machine learning problems by transformation and algorithm adaptation methods[7]. The transformation method transforms the multiple output regression problem into multiple and independent single output problems, each to be predicted by a classical machine learning algorithm. In algorithm adaptation methods, a single target machine learning algorithm, such as decision trees or support vector machines, are used to directly predict the multiple output data set. The latter is a challenging problem as the learning algorithm not only needs to map the features to more than one output variable, but is also required to interpret the dependencies among these multiple targets.

Another powerful technique that is also a subset of machine learning and that can handle complex multiple variate target problems is the Artificial Neural Network (ANN). Compared to the aforementioned classical models, the ANN algorithm can be used to build deep networks with multiple hidden layers to predict multiple target variables without handcrafted features.

The advancement in deep learning has inspired many applications in computer vision, natural language processing, time series prediction, and image generation via using more sophisticated forms of neural networks, such as the Convolutional Neural Network, the Recurrent Neural Network, and the Generative Adversarial Nets. Nonetheless, modeling using ANN is sometimes referred to as black-box modeling, as deep learning models can be difficult to understand of how it can arrive to a certain prediction by summing up the information coming from different nodes and layers.

In this article, reference simulation models from a commercial simulator with the objective of modeling the deep polymer gel model inside a naturally fractured reservoir are generated. Several well design and reservoir features are extracted from the simulation models along with multiple target production outputs to generate a data set to be used for training and validating an ANN model capable of approximating the production results from the reservoir simulator.

Reservoir Modeling

A commercial reservoir simulator was used to prepare the input features and multiple target production data for the neural network. Detailed reservoir description of the grid, fluid components, chemical reaction, adsorption modules, relative permeability curves, and the wells' configurations used in the simulations are provided.

Reservoir Grid. The reservoir is a 3D Cartesian model with three uniform layers of equal thickness. A grid block sensitivity analysis was performed to determine the optimum number of grids to be used to construct the model. Cumulative production data and simulation running time was compared using different grid sizes from 10 × 10 to 55 × 55, where the number of grids are the same in the x and y directions for each grid size.

Figure 1 is the grid sensitivity analysis showing that the cumulative production results start to level at a grid size of 25 × 25. In addition, the simulation time significantly starts to increase for larger grid sizes. Therefore, a grid size of 25 × 25 was used as an optimum grid size to construct all the models and generate the data set as it gives accurate production results combined with a faster running time.

Generally, there are two types of grid models for naturally fractured reservoirs in modern reservoir

Fig. 1 *Grid sensitivity analysis.*

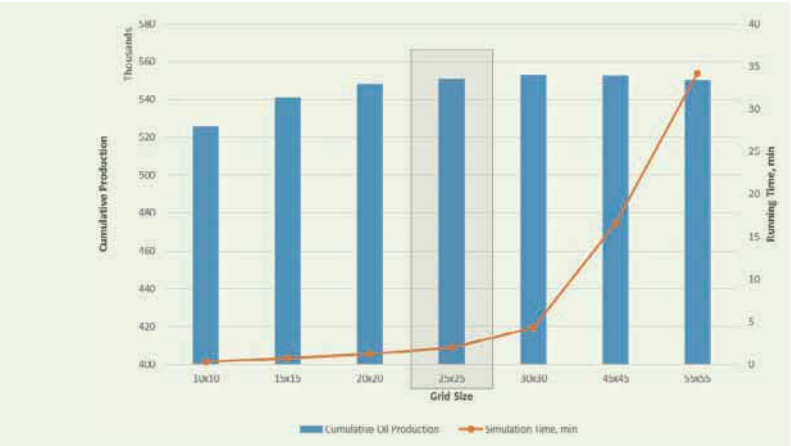

simulation packages: dual porosity and dual permeability models[8]. The dual porosity models assume that the fractures are the essential components responsible for fluid flow into the wellbore having a low permeable matrix. Therefore, fluid flows from the discrete matrix blocks into the fractures, and consequently, toward the wellbore in dual porosity models. On the other hand, in dual permeability models, both the fracture and matrix components provide a means for fluid and heat transfer within the media and toward the wellbore.

Figure 2 demonstrates the difference between the dual porosity and dual permeability models in terms of fluid flow direction as captured in the reservoir simulation. In our model, we use the dual permeability concept to represent the natural fractures in the reservoir media.

Fluid Components and In Situ Gel Kinetics. There are five types of fluid that are injected into the reservoir: oil, water, polymer, crosslinker, and gel. It is assumed that all of these components exist in an aqueous phase except for the oil, where it partitions into an oleic phase. Fluid component properties were adopted[5], where we use an oil API of 45° and molecular weights of 10,000 lb/lbmol and 206 lb/lbmol for the polymer and crosslinker components, respectively.

The in situ gel, which is essentially responsible for plugging the fractures, is formed by considering a simple reaction mechanism between the added polymer and crosslinker, such that a 1 lbmol of polymer is reacting with 1 lbmol of crosslinker to produce 1 lbmol of in situ gel[5]. It is assumed that the gel formation is the first order in each of the reactions, i.e., second order overall. Given that the C1° and C2° are the initial concentrations of polymer and crosslinker, respectively, the gel concentration at any time can be calculated given a single rate constant, $K = 5\times10^{6}$ day^{-1} from Eqn. 1[5]:

$$C_3 = \frac{KC_1C_2(C_1+C_2)t}{1+KC_1C_2t} \quad (1)$$

Rock-Fluid Properties (Adsorption and Relative Permeability Data). Table 1 lists the adsorption properties for both the polymer and gel components populated in the model[5]. Table 2 lists the ratio between the fluid permeability before and after injecting the gel, for the formed in situ gel is greater than the polymer,

Fig. 2 *Representation of the difference between the dual porosity model (left) and the dual permeability model (right) in terms of fluid flow direction as captured in the reservoir simulation[8].*

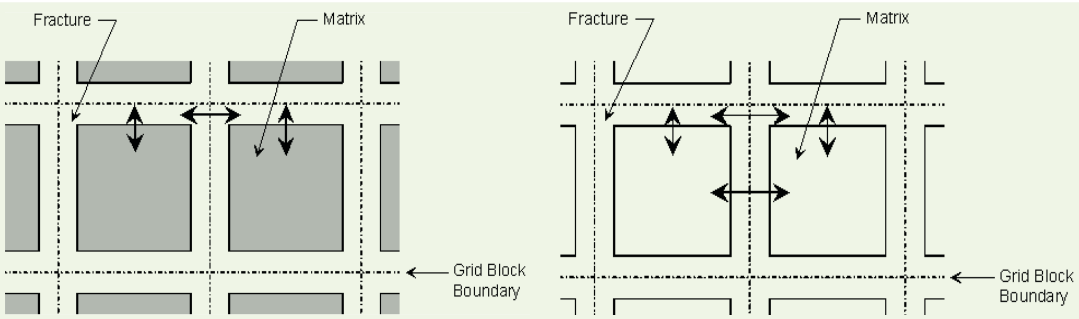

Table 1 *The adsorption properties for polymer and gel components in a matrix and fracture populated in the model.*

Fluid	Polymer		Gel	
	Matrix	Fracture	Matrix	Fracture
Adsorption Capacity (lbmol/ft^3)	0.01364×10^{-4}	0.0572×10^{-4}	0.0267×10^{-4}	0.0575×10^{-4}
Residual Resistance Factor	1.8	2.5	40	80

Table 2 Relative permeability data[5].

Water Saturation (S_w)	Relative Permeability to Water (k_{rw})	Relative Permeability to Oil (k_{row})
0.25	0	0.9
0.3	0.002	0.69
0.4	0.03	0.33
0.5	0.06	0.13
0.6	0.14	0.04
0.7	0.2	0.005
0.78	0.3	0

causing a significant reduction in effective permeability in the reservoir system and mainly acting as a plugging agent for the existing fractures in the reservoir model.

The water-oil relative permeability model was also adapted after Scott et al. (1987)[5]. The relative permeability data used in the model assumes a water-wet system with relatively high permeable layers, as in the case of this model.

Figure 3 displays the relative permeability data included in the model.

Well Configuration. Two vertical wells are included in the model: (1) a producer, and (2) an injector. The placement of these two wells is selected to reflect the position of one-fourth of a five spot injection pattern, Fig. 4. Therefore, the generated production profiles could be used to reflect the behavior of a polymer gel flooding or waterflooding pilot with a five-spot pattern arrangement.

Fig. 4 A 3D cross section of the placement of these two wells is selected to reflect the position of onefourth of a five spot injection pattern.

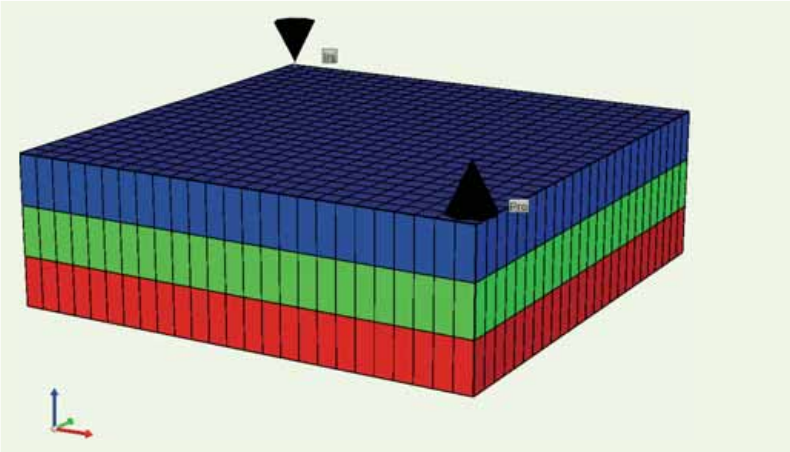

Data Set Generation

The 12 input features of the reservoir properties and well design parameters, such as matrix porosity, fracture permeability, injection rate, etc., were independently randomly generated within a predetermined range. Figures 5 and 6 are examples of the generated random matrix and fracture permeability data for all 1,000 generated cases, respectively. These ranges were selected to cover a wide range of dual permeability reservoirs and sensitivity analyses. Tables 3 and 4 show the various ranges of input features used to build the simulation model and generate the data set.

As this is a multiple output problem, for each generated case, three target variables are collected over a specified time frequency: (1) oil rate, (2) water cut,

Fig. 3 Relative permeability curve[5].

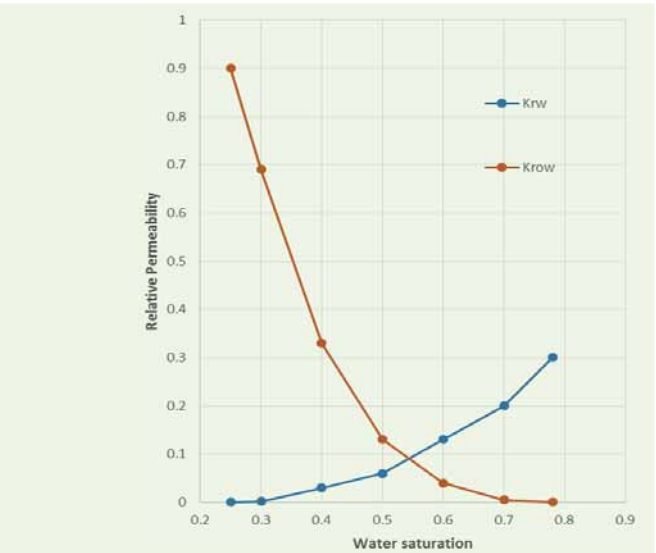

Fig. 5 The distribution of randomly generated matrix permeability data.

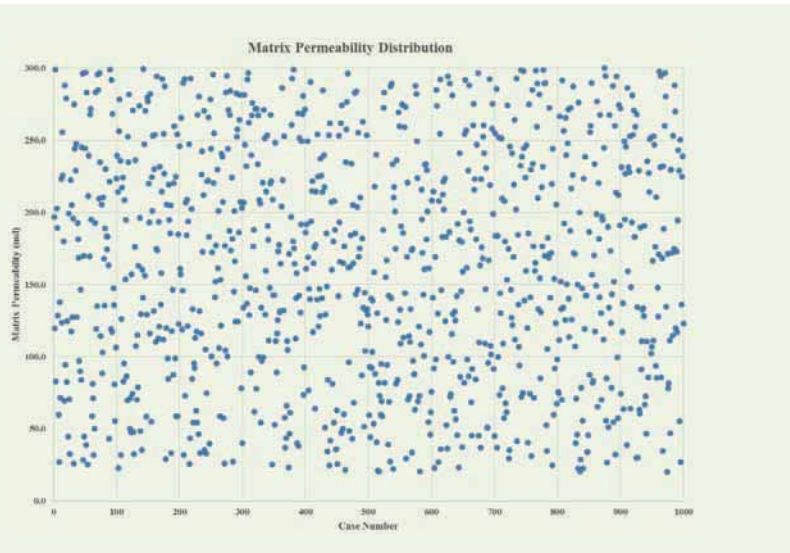

Fig. 6 *The distribution of randomly generated fracture permeability data.*

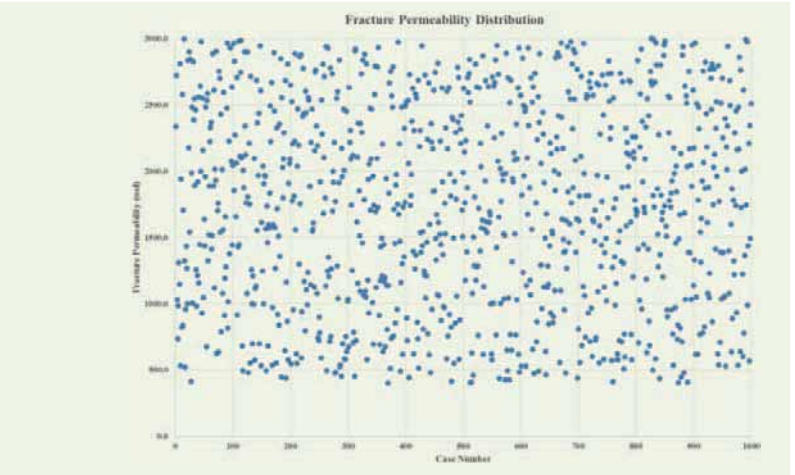

and (3) recovery factor. The results are collected over a 10-year period. For the first two years, the data is collected every 15 and 30 days. For the remaining years, the data is collected every 90 days. It was desired to have a higher resolution time for the first two years to better capture the behavior of water breakthrough occurring at early production.

In total, 68 data points were collected over the 10-year period for each target variable. In addition, an abandonment rate of 10 stock tank barrels per day is considered for all cases. Table 5 demonstrates the input features that are used to generate two example cases, case 10 and case 13.

Figures 7 and 8 show the collected results of oil rate, recovery factor (RF), and water cut for these two cases. To have a consistent 68 data points and time frequency for all of the cases, data points after abandonment condition were set equal to the data point at the abandonment time.

Determining the optimum number of data sets for a given data-driven model requires the developer to know beforehand the various ranges of features and different expected trends of the target production data to avoid training unnecessary large data sets that could potentially lead to memorization and overfitting. In this study, initially 500 cases were used to build the network.

It was observed later that the model always fails to predict a common trend of production curves regardless of the ANN structure being used. After further analysis of these production trends, it was realized that these trends were mostly associated with a low injection rate and low permeable systems. Therefore, more cases within these ranges were generated and augmented to the original data set. After several investigations

Table 3 *The range of reservoir properties used in the model.*

Reservoir Property	Min	Max	Unit
Reservoir Thickness (h)	50	300	ft
Matrix Porosity (Φ_m)	0.15	0.4	fraction
Fracture Porosity (Φ_f)	0.0001	0.01	fraction
Matrix Permeability (k_m)	20	300	mD
Fracture Permeability (k_f)	400	3,000	mD
Fracture Spacing (d_f)	33	328	ft
Initial Water Saturation (S_w)	0.1	0.3	fraction

Table 4 *The ranges of project design parameters used in the model.*

Design Parameter	Min	Max	Unit
Injection Rate (q_w)	100	5,000	bbl/d
Producer Flowing Pressure (p_{wf})	3,000	3,700	psia
Drainage Area (A)	5	30	acres
Polymer Concentration ($PLMR$)	1000	5,000	ppm
Cross-linker Concentration ($XLKR$)	100	500	ppm

Table 5 *The input features for example cases 10 and 13.*

Input Features	Case 10	Case 13	Unit
Reservoir Thickness (h)	119	107	ft
Matrix Porosity (Φ_m)	0.20	0.16	fraction
Fracture Porosity (Φ_f)	0.0002	0.01	fraction
Matrix Permeability (k_m)	138	124	mD
Fracture Permeability (k_f)	1,941	836	mD
Fracture Spacing (d_f)	94	31	ft
Initial Water Saturation (S_w)	0.22	0.13	fraction
Injection Rate (q_w)	1,700	990	bpd
Producer Flowing Pressure (p_{wf})	3,442	3,033	psia
Drainage Area (A)	22	22	acres
Polymer Concentration (*PLMR*)	2,296	3,917	ppm
Crosslinker Concentration (*XLKR*)	214	239	ppm

Fig. 7 *An example of the production data collected for case-10.*

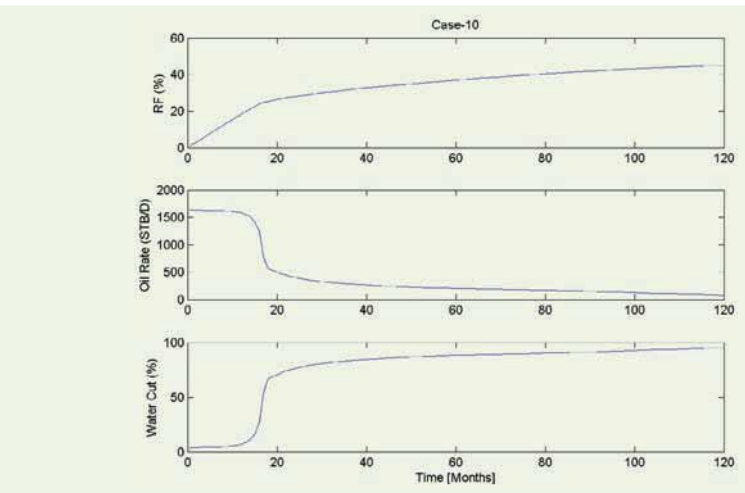

Fig. 8 *An example of the production data collected for case-13 (gel scenario).*

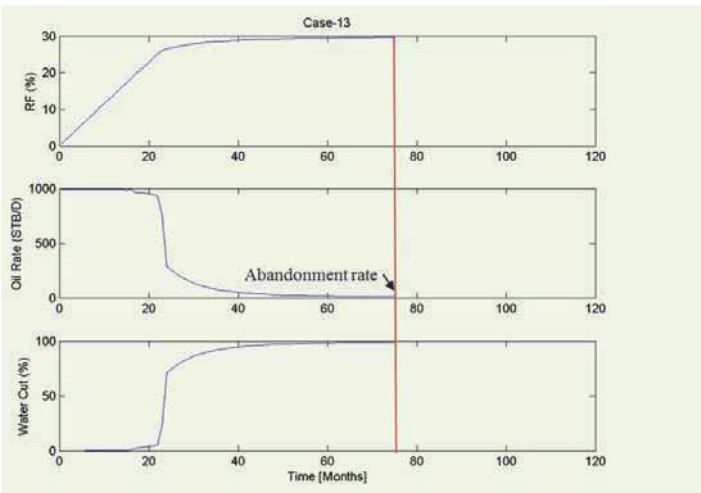

and optimization of the data set, it was found that using 1,000 generated cases is the optimum number for this problem.

ANN

Background

ANN is an information processing system that attempts to mimic the functionality and complexity of the neural biological system[9]. The information, in the form of electrical signals, are received by the dendrites, processed by the soma and then passed to the axon. Similarly, the artificial neurons are the building blocks for the ANN. The information comes to the artificial neuron via inputs, where each input is multiplied by a weighting function before entering the neuron. The neuron then sums the weighted inputs and bias, and processes the sum via an activation or a transfer function before passing the information to the outputs[10].

Figure 9 indicates the difference between the biological and artificial neurons.

In most cases, using one artificial neural is not sufficient to solve complex problems. Therefore, we often find neurons combined and arranged in layers. The arrangement of these layers and connection between neurons define the ANN architecture.

There are typically two types of networks, a single

Fig. 9 The difference between a biological neuron (left) and an artificial neuron (right)[10].

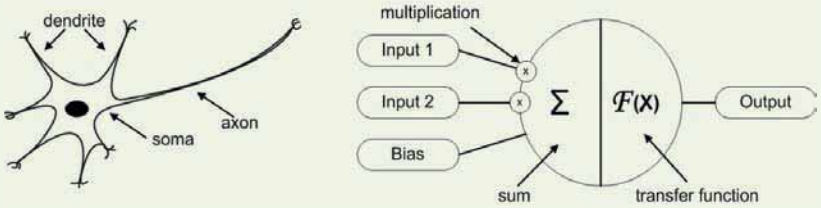

layer network or a multilayer network. A single layer network contains only one layer, whereas, multilayer networks could have more than one layer. These layers are often referred to as hidden layers, as opposed to the input and output layer of the network.

Figures 10[11] and 11[11] demonstrate the difference between a single layer network and a multilayer network.

Fig. 10 An example of a single layer network[11].

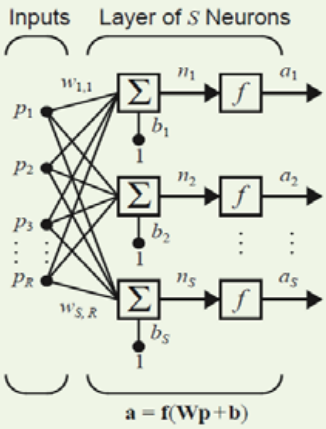

ANN Algorithm

The following explains the calculation steps occurring inside the ANN model for generating the output results. Generally, the ANN model undergoes two major calculation passes: (1) a forward pass from the features input to the target output, and (2) a backward pass from the output target to the features input for updating the initial weights and biases of the model using an optimization algorithm, such as the gradient descent.

Forward pass. For a set of features, x, the predicted output, $\hat{y}$ from the network in a forward pass is calculated by summing the product of weights and biases of all input features and passing it to an activation function to get the $\hat{y}$, as:

$$\hat{y} = \sum_i f(W_i x_i + b_i) \quad (2)$$

where $\hat{y}$ is the predicted output from the network, W_i is the initial weight for a given feature, b_i is the bias for a given feature, x_i is the input feature, and f is the activation function.

A common f is the sigmoid activation function, which is used in this article. Given an input, x, the sigmoid activation function is calculated as:

$$\sigma(x) = \left(\frac{1}{1+e^{-x}}\right) \quad (3)$$

Backward pass. The loss is calculated between the

Fig. 11 An example of a multilayer network containing three layers[11].

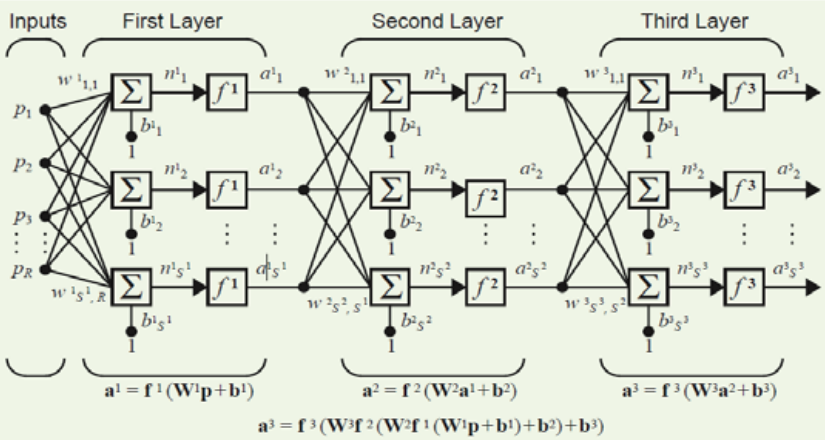

target, y, and the predicted output by the network, $\hat{y}$. A common loss function is to use the sum of the mean squared error (MSE), as used in this article, which is defined as:

$$E = \frac{1}{2m}\sum_{\mu}(y^{\mu} - \hat{y}^{\mu})^2 \quad (4)$$

This error is summed across all output targets and across all data points (m). The derivative of these losses with respect to the weights are then calculated to obtain the new weights via an optimization algorithm to prorogate back the updated weights through the network, i.e., backpropagation. This study uses the stochastic gradient descent optimization algorithm, where the new weights are updated as:

$$W_i = W_i + \alpha\delta x_i \quad (5)$$

where δ is the learning rate of the network, and α is the error term.

The error term is defined as:

$$\delta = (y - \hat{y})f'(\sum_i W_i x_i) \quad (6)$$

The derivative of the sigmoid activation function used in this article is calculated as:

$$\sigma'(x) = \sigma(x)\,(1 - \sigma(x)) \quad (7)$$

Given the above procedure, the model will continue running, updating weights and improving prediction for all targets until a certain number of iterations or epochs is reached, which is one of the tuning hyperparameters of the network. The model also could be stopped earlier given a specified validation loss, the early stopping technique, to prevent the model from .memorization and overfitting

Evaluation Metrics

The generated data set was randomly divided into 90% for training, 5% for validation and 5% for testing. The validation set was monitored closely throughout training to prevent underfitting or overfitting of the data. Furthermore, the data sets allocated for testing are used as a caliber to evaluate the prediction's accuracy of the network for cases outside the training set. Therefore, the absolute error between the network's output (ANN value), and the simulator's original value (simulator value), is calculated for each data point in the testing data set as:

$$Error\ \% = \left|\frac{Target_{Simulator} - Output_{ANN}}{Target_{Simulator}}\right| \times 100 \quad (8)$$

Furthermore, the average error per testing case can be used as a performance indicator of the network's efficiency and is calculated as:

$$Average\ Error\ \% = \frac{\sum_{i=1}^{N} Testing\ Error\ \%}{N} \quad (9)$$

where N represents the total number of data points per testing case. The error between the predicted network output and desired target was regularly evaluated for all testing cases, and progressively improved via fine-tuning of the network's hyperparameters, including the number of epochs, learning rate, number of

Table 6 *The input, output, and functional link components for the generated ANN model.*

INPUT	**Reservoir Properties**	Reservoir Thickness
		Matrix Porosity
		Fracture Porosity
		Matrix Permeability (Lateral direction-H)
		Matrix Permeability (Vertical direction-V)
		Fracture Permeability
		Fracture Spacing
		Initial Water Saturation
	Design Parameters	Injection Rate
		Producer BHP
		Drainage Area
		Polymer Concentration
		XLinker Concentration
	Functional Links	(Injection Rate/Matrix Permeability)/100
		log[(Injection Rate)$^{0.5}$ + (Matrix Permeability)$^{0.5}$]/10
		(Fracture Permeability/Injection Rate)/10
		log[(Injection Rate)$^{0.5}$ + (Fracture Permeability)$^{0.5}$]/10
		Drainage Area/Injection Rate
		Fracture Spacing/Injection Rate
		log[Matrix Porosity/Injection Rate]*100
		log[Fracture Porosity/Injection Rate]*1000
		log[Injection Rate/Producer BHP]
		log[Injection Rate/Thickness]
		log[Injection Rate/Water Saturation]
		log[Thickness * Drainage Area]
		log[(injection Rate)$^{0.5}$ + (Thickness)$^{0.5}$]
		log[(injection Rate)$^{0.5}$ + (Drainage Area)$^{0.5}$]
		log[Polymer Concen. + Xlinker Concen.]/10
		log[(Injection Rate) $^{0.5}$ + (Polymer + Xlinker Concen.)$^{0.5}$]
OUTPUT	**Oil rate, water cut, and recovery factor**	68 data points for each; time frequency as follows: 15 days for year 1, 30 days for year 2, 90 days for years 3 to 10

hidden layers, and the number of neurons inside the hidden layers.

ANN Model

An ANN model is developed to predict and generate production profiles of the oil rate, water cut, and recovery factor for a given specified set of dual permeability reservoir properties and polymer gel design parameters that were described in the data generation set. The input features and output production targets were normalized prior to training to a value of 1 and -1, using Eqn. 10:

$$x' = \frac{x - \min(x)}{x - max\,(x)} \qquad 10$$

where x represents the original input feature or target value, and x' represents the transformed scaled values.

This scaling was performed to improve the network's learning rate. Additionally, some extra features, called functional links, were added, which helped to improve the performance of the network.

There are no generalized forms of these functional links and they could be a random combination between different input or output parameters[12]. In this model, the injection rate was found to be an important feature that can help the network estimate the initial oil rate of the well, and therefore, was used to link and connect other features.

Table 6 shows the various inputs and outputs that was used to build the network. The input layer contains 29 features, 16 of which are functional links between the reservoir properties and design parameters in the input layer. For each case, the output layer contains a target vector with 204 neurons, representing the associated targets of the oil rate, water cut, and recovery factor per case, with a total frequency of 68 data points for every target variable collected over a 10-year period, given the time frequency provided in the data generation section.

Fig. 12 *The performance of the ANN network showing the training, testing, and validation losses for the data set.*

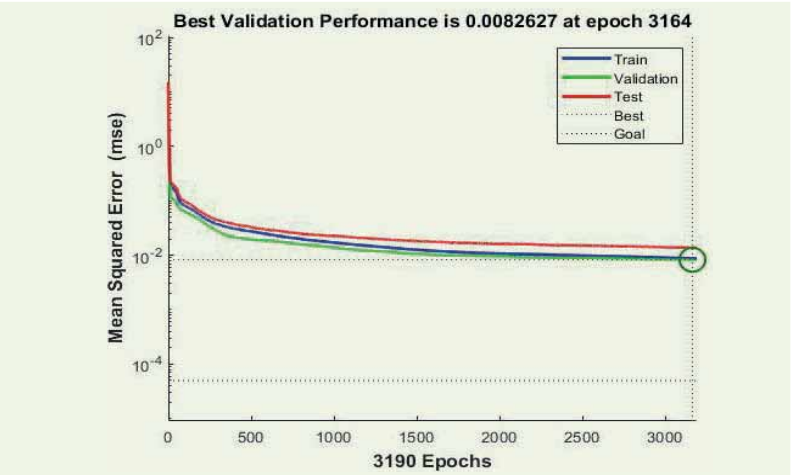

Hyperparameters Optimization

The ANN model was run for over 3,000 epochs. The validation loss, using the MSE, was monitored to ensure that the model is not overfitting. Figure 12 shows the training, validation, and testing losses against the

Fig. 13 *The ANN prediction vs. target correlation coefficient for the training, validation, and testing sets.*

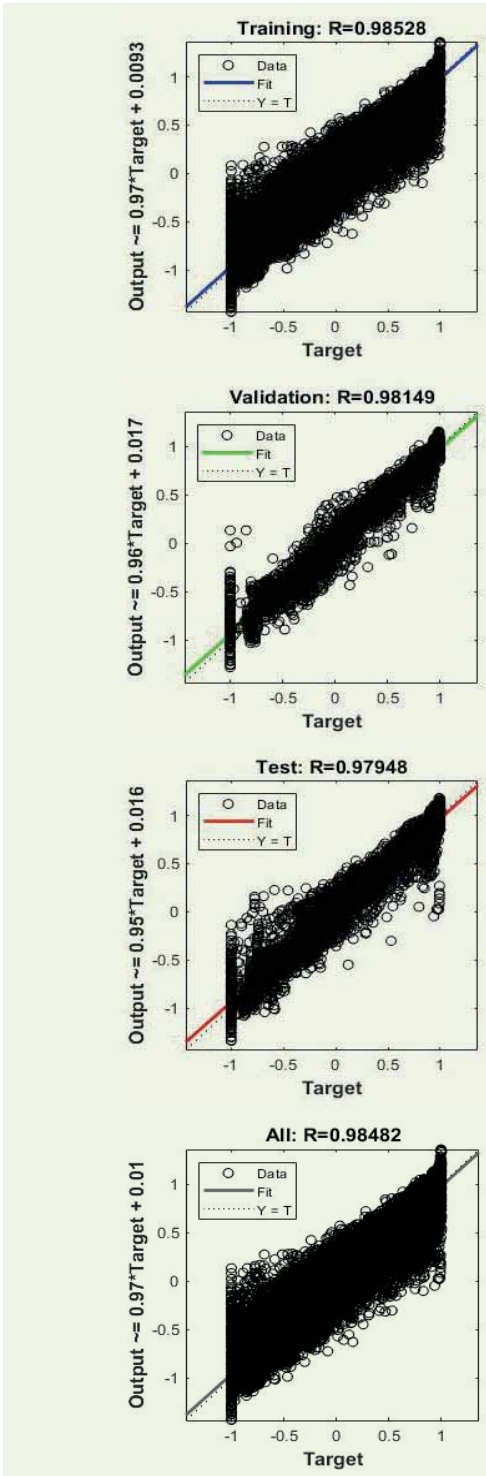

number of total epochs or model's iterations.

Figure 13 shows the correlation coefficients obtained for the training, validation, and testing data set, exceeding 0.97. This model was generated using a total of six hidden layers. There is no single rule of thumb to determine the number of hidden layers or neurons required to fit a data set. Determining the number of hidden layers and neurons in a neural network is a heuristic process. In this study, an iterative algorithm was developed to automatically fit several initial network structures to the data set by assigning a random number of neurons and layers to each structure. Then, the performance of these structures are compared against each other to estimate the best possible combination of total hidden layers and neurons that would yield the least MSE for all testing cases, as previously mentioned.

Table 7 shows a summary of the hyper parameters used to generate the model. Table 8 shows the input features for some of the selected test cases, and Figs. 14 to 17 show the production profiles generated by the ANN model matching the results of the simulation model for these cases. As can be seen from these plots, the addition of polymer gels improves the production profiles by arresting early water breakthrough and sustaining a higher plateau oil rate during the first 20 to 40 months of production. For all 50 test cases, the mean average error were 2.46%, 10.31%, and 8.01% for the recovery factor, oil rate, and water cut, respectively.

Figures 18 to 20 shows the MSE distribution per test case for each target variable. The maximum error observed was less than 25% for all cases.

Table 7 *The final hyperparameters used to construct the ANN model.*

Hyperparameter	Value
Number of epochs	3,164
Optimization algorithm	Gradient Descent
Learning rate	0.001
Loss	MSE
Activation function	Sigmoid
Neurons in hidden Layer 1	90
Neurons in hidden Layer 2	95
Neurons in hidden Layer 3	110
Neurons in hidden Layer 4	150
Neurons in hidden Layer 5	110
Neurons in hidden Layer 6	115

Conclusions

This work presents a unique surrogate modeling approach based on machine learning to describe complex polymer gel kinetics and flow dynamics in deep conformance applications. The presented neural network model was used to robustly predict the production and oil recovery performance of polymer gel treatments in fractured reservoirs outperforming commercial simulators in terms of computational complexity and processing speed. The following conclusions are derived from this study:

Table 8 *The input features for some of the selected test cases.*

Input Feature	Testing Cases			
	Case 53	Case 227	Case 589	Case 801
Reservoir Thickness (h)	18.19	15.27	20.02	18.58
Matrix Porosity (Φ_m)	50.79	41.77	88.91	94.80
Fracture Porosity (Φ_f)	0.38	0.52	0.18	0.43
Matrix Permeability (k_m)	0.01	0.01	0.01	0.00
Fracture Permeability (k_f)	283.03	117.44	160.46	75.50
Fracture Spacing (d_f)	2,481.36	2,440.62	2,084.87	1,668.80
Initial Water Saturation (S_w)	2,241.36	2,200.34	4,262.43	1,753.73
Injection Rate (q_w)	3,040.62	3,625.07	3,553.94	3,456.19
Producer Flowing Pressure (p_{wf})	0.27	0.26	0.14	0.22
Drainage Area (A)	52.74	277.35	177.53	214.71
Polymer Concentration ($PLMR$)	3,956.79	2,528.83	2,756.47	4,266.55
Cross-linker Concentration ($XLKR$)	233.74	145.15	293.17	421.14

Fig. 14 *The comparison of the polymer gel production profiles generated by the ANN model matching the results of the simulation model for these cases (Test Case-53).*

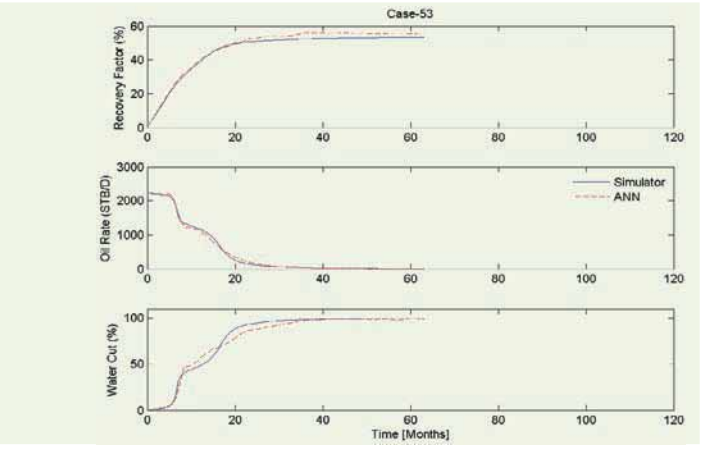

Fig. 15 *The comparison of the polymer gel production profiles generated by the ANN model matching the results of the simulation model for these cases (Test Case-227).*

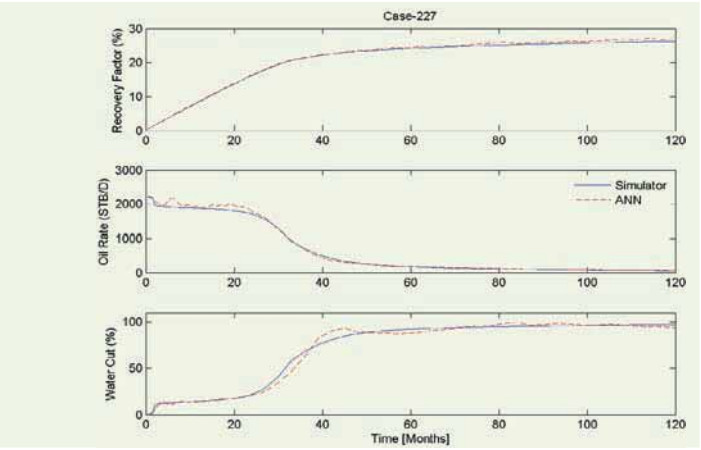

Fig. 16 *The comparison of the polymer gel production profiles generated by the ANN model matching the results of the simulation model for these cases (Test Case-589).*

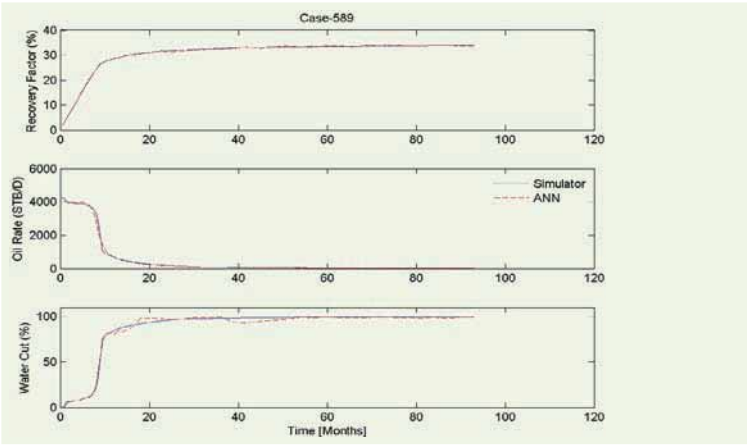

Fig. 17 *The comparison of the polymer gel production profiles generated by the ANN model matching the results of the simulation model for these cases (Test Case-801).*

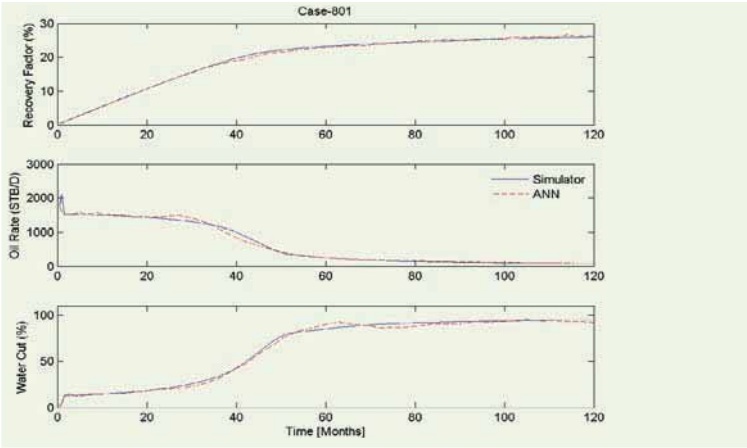

- The ANN models can be used to fit multiple output regression problems as shown in this study. For a given 29 input features and functional links of reservoir and well parameters, the model was able to accurately predict 204 outputs representing the oil rates, water cuts, and recovery factor production profiles over a 10-year period for polymer gel conformance treatments in the fractured reservoirs. Therefore, the ANN model was able to generate a time series forecasting of multiple target variables offering an advantage over classic machine learning algorithms commonly limited to a single target variable.
- Hyperparameter tuning indicates that using a sigmoid activation function and updating the model's weights using a MSE loss and a gradient descent algorithm are the best combination to train the neural network with total iterations of 3,142.
- Optimization results also indicate that generating a deep network with six hidden layers yields the best prediction results for this problem. The mean average error for all testing cases were 2.46%, 10.31%, and 8.01% for the recovery factor, oil rate, and water cut's target variables, respectively.

Fig. 18 *The MSE distribution per test case for the recovery factor.*

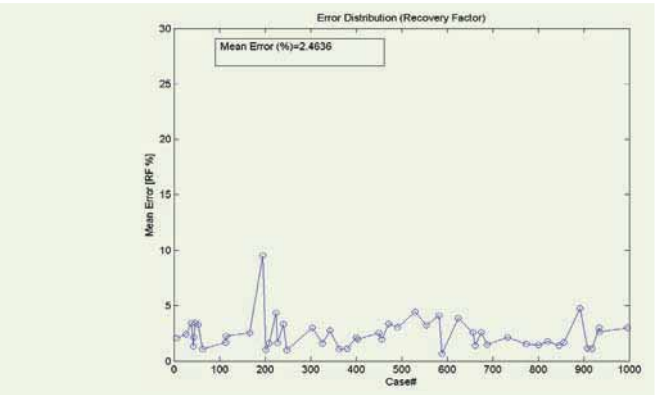

Fig. 19 *The MSE distribution per test case for the water cut.*

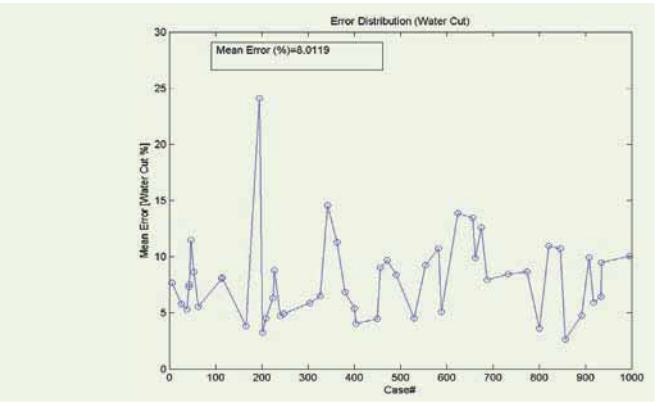

Fig. 20 *The MSE distribution per test case for the oil rate.*

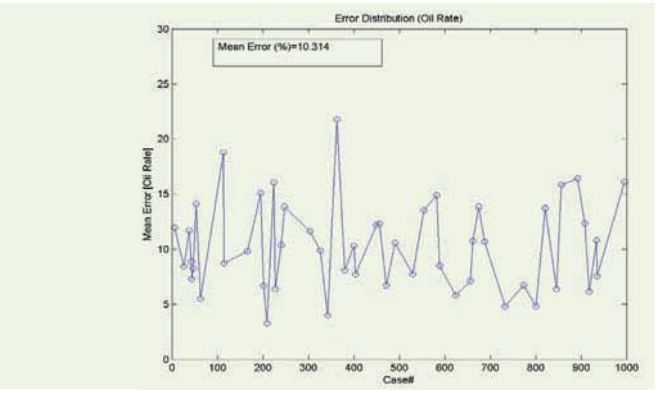

Acknowledgments

This article was prepared for presentation at the Abu Dhabi International Petroleum Exhibition and Conference, Abu Dhabi, UAE, November 9-12, 2020.

References

1. Argabright, P.A., Rhudy, J.S. and Trujillo, E.M.: "Anatomy of a Full Field Polymer Augmented Waterflood Project," Chapter 15 in *Water-Soluble Polymers Beauty with Performance*, Glass, J.E. (ed.) from the *Advances in Chemistry Series*, Vol. 213, May 1986, pp. 269-311.
2. Du, Y. and Guan, L.: "Field-Scale Polymer Flooding: Lessons Learnt and Experiences Gained during Past 40 Years," SPE paper 91787, presented at the SPE International Petroleum Conference in Mexico, Puebla Pue, Mexico, November 7-9, 2004.
3. Sydansk, R.D.: "A New Conformance Improvement Treatment Chromium(III) Gel Technology," SPE paper 17329, presented at the SPE Enhanced Oil Recovery Symposium, Tulsa, Oklahoma, April 16-21, 1988.
4. Sydansk, R.D. and Southwell, G.P.: "More Than 12 Years of Experience with a Successful Conformance Control Polymer Gel Technology," *SPE Production and Facilities*, Vol. 15, Issue 4, November 2000, pp. 270-278.
5. Scott, T., Roberts, L.J., Sharp, S.R., Clifford, P.J., et al.: "In Situ Gel Calculations in Complex Reservoir Systems Using a New Chemical Flood Simulator," *SPE Reservoir Engineering*, Vol. 2, Issue 4, November 1987, pp. 634-646.
6. Dey, A.: "Machine Learning Algorithms: A Review," *International Journal of Computer Science and Information Technologies*, Vol. 7, Issue 3, 2016, pp. 1174-1179.
7. Borchan, H., Varando, G., Bielza, C. and Larranaga, P.: "A Survey on Multi-Output Regression," *Wiley Interdisciplinary Reviews: Data Mining and Knowledge Discovery*, Vol. 5, Issue 5, July 2015.
8. Computer Modeling Group Ltd.: "STARS User Guide: Advanced Process and Thermal Reservoir Simulator," 2012.
9. Mohaghegh, S.: "Virtual Intelligence Applications in Petroleum Engineering: Part 1 — Artificial Neural Networks," *Journal of Petroleum Technology*, Vol. 52, Issue 9, September 2000, pp. 64-73.
10. Suzuki, K. (ed.): *Artificial Neural Networks — Methodological Advances and Biomedical Applications*, InTechOpen, 2011, 374 p.
11. Hagan, M.T., Demuth, H.B., Beale, M.H. and de Jesus, O.: *Neural Network Design*, 2nd edition, 2002, 800 p.
12. Ersahin, A., Gul, S., Ertekin, T. and Temizel, C.: "Artificial Neural Network Modeling of Cyclic Steam Injection Process in Naturally Fractured Reservoirs," SPE paper 195307, presented at the SPE Western Regional Meeting, San Jose, California, April 23-26, 2019.

About the Authors

Mohammed A. Alghazal

M.S. in Petroleum Engineering, Pennsylvania State University

Mohammed A. Alghazal is currently working as a Lead Reservoir Management Engineer in the South Ghawar Reservoir Management Division of Saudi Aramco's Southern Area Reservoir Management Department. He previously worked as a Core Analyst in the Petrophysics Unit in the Exploration and Petroleum Engineering Center – Advance Research Center (EXPEC ARC), and as a member of the Reservoir Technical Study group in the Southern Area Reservoir Management Department.

Throughout Mohammed's career, he conducted several reservoir assessment studies in the area of reservoir fluid characterization, sweep efficiency evaluation, complex reservoir development, secondary reservoir evaluation and well testing. Mohammed also has a key interest in utilizing artificial intelligence and machine learning to solve complex data-driven problems.

Mohammed is an active member of the Society of Petroleum Engineers (SPE), and a SPE Certified Petroleum Engineer. He has authored and coauthored several technical papers at local, regional, and international SPE conferences.

In 2010, Mohammed received his B.S. degree in Petroleum Engineering from the University of Manchester, Manchester, U.K. In 2015, he received his M.S. degree Petroleum Engineering from Pennsylvania State University, State College, PA.

Mohammed also has two Nanodegrees in Data Science related to machine and deep learning.

Prof. Turgay Ertekin

Ph.D. in Petroleum and Natural Gas Engineering, Pennsylvania State University

Professor Turgay Ertekin is a Professor of Petroleum and Natural Gas Engineering and Head of the John and Willie Leone Family Department of Energy and Mineral Engineering at Pennsylvania State University. He is also the holder of the George E. Trimble Chair in Earth and Mineral Sciences at the university. Turgay's main research area is mathematical modeling of fluid flow dynamics in porous media and implementation of artificial intelligence technology with respect to various reservoir engineering process analyses.

He is a recipient of several Society of Petroleum Engineers (SPE) international awards, including the 1998 Distinguished Achievement Award for Petroleum Engineering Faculty, the 2001 Lester C. Uren Award for Distinguished Achievement in the Technology of Petroleum Engineering, the 2001 SPE Distinguished Member Award, and the 2013 SPE Honorary Membership Award.

At Penn State, Turgay has received the College of Earth and Mineral Sciences' Teaching, Research, Service, and Mentorships awards and also the university's Graduate School Teaching Award.

For a two-year period, he served as the Executive Editor of the *SPE Formation Evaluation Journal* and he currently is serving as Editor-in-Chief for the *Journal of Petroleum Exploration and Production Technology*.

Turgay received his B.S. and M.S. degrees in Petroleum Engineering from the Middle East Technical University, Ankara, Turkey, and his Ph.D. degree in Petroleum and Natural Gas Engineering from Pennsylvania State University, State College, PA.

Physical Performance Testing of a Prototype Gerotor Pump Operating in Liquid and Gas-Liquid Conditions

Dr. Chidirim E. Ejim, Dr. Jinjiang Xiao and Dr. Olanrewaju M. Oshinowo

Abstract /

Gerotors are positive displacement pumps and potential artificial lift options in the oil and gas industry. This study presents the performance characteristics from physical testing of a unique one-stage, equal-walled gerotor pump design operating in oil and oil-air mixtures. The pump was tested at various rotational speeds in a flow loop. The performance results were obtained to ascertain potential design optimizations of the pump before embarking on manufacturing and testing of the field prototype pump.

A physical prototype of a one-stage 400 series gerotor pump, suitable for application in a 5½" casing, was designed, manufactured, assembled, and tested. Mineral oil and air were used as the operating media. For given pump outlet valve settings, the pump rotational speeds were set to 200, 250, 300, and 350 revolutions per minute (rpm). The gas volume fractions (GVF) at the pump inlet were varied from 0% to the maximum the current pump design could handle. For each test point, the corresponding pump parameters were measured. Dimensionless performance plots were established for obtaining pump performance at other flow conditions.

The results showed that pump flow rate decreased with increasing differential pressure, typical of positive displacement pumps. At 200 rpm and 350 rpm, maximum pump delivery is approximately 190 barrels per day (bpd) and 330 bpd of oil, respectively, at zero differential pressure. The pump can supply flow against a differential pressure of up to approximately 5.5 psi at 200 rpm and 15 psi at 350 rpm. For the 200 rpm to 350 rpm speed range, volumetric efficiencies varied from 30% to 73%, whereas the electric power input varied from 145 watts (W) to 191 W. When pumping oil-air mixtures, the current gerotor pump design can handle a maximum of 15% GVF, at 250 rpm, 300 rpm, and 350 rpm.

For certain pump outlet pressures, the total fluid flow rates decreased as the GVF increased to 15%. The volumetric efficiencies at 15% GVF varied from 32% to 53%, for the 300 rpm to 350 rpm speed range, whereas the motor's electric power input decreased with increasing the GVF up to 15%. Increasing the pump's rotational speed improves the volumetric efficiency and the gas handling capability of the gerotor pump. These observations will aid in the required design optimization to enhance the performance of the future field prototype gerotor pump.

This study presents the capabilities of gerotors as potential artificial lift alternatives to handle liquid and gas-liquid mixtures for boosting applications in oil field operations. The technology with additional design optimization can be readily integrated into oil field equipment architecture. The mechanical simplicity of gerotors and their compactness provides a promising artificial lift substitute that may be implemented for downhole or surface production of liquid or gas-liquid mixtures in the oil and gas industry.

Introduction

Oil field operations involve the production of liquids (oil, water, condensate, etc.) and gases from a downhole reservoir to the wellhead at the surface and onward to production facilities. Artificial lift systems are typically installed in wells to either sustain or boost hydrocarbon production from reservoirs. These artificial lift systems can be of different types, e.g., rotordynamic, positive displacement, gas lift, hydraulic lift, or can utilize the reservoir fluid energy to produce the well.

The presence of gas in the well depends on the properties of the reservoir fluid and the pressure in the well. When the downhole pressure decreases below the bubble point pressure, gas within the oil comes out of the solution. When this occurs, the gas, which occupies more volume than the oil, reduces oil production to the surface. Therefore, the volume of gas to total liquid and gas at a given pressure and temperature, or gas

volume fraction (GVF), is an important parameter when producing gas-liquid multiphase flows.

A majority of artificial lift systems operate satisfactorily when handling pure liquids; however, their performance deteriorates when they produce gas-liquid multiphase flows. Handling gas-liquid multiphase flows using artificial lift systems can include the use of helicoaxial pumps, centrifugal multiphase pumps, twin-screw pumps, and progressing cavity pumps (PCPs)[1]. PCPs are a type of positive displacement pump that typically has an elastomeric stator and a metal rotor.

Typical GVF handling capabilities for these pumps is approximately 33%, and is due to a 120 °C temperature limitation of the stator's elastomer[2], as the pump compresses the gas in the gas-liquid mixture. PCPs with metallic stators and rotors are now being developed. These have temperature limitations of 350 °C, and the capability to handle GVFs up to 60%[3].

Gerotors are positive displacement pumps with relatively simple components, fewer moving parts, and compact size. The major components are an inner metal rotor, which is enclosed by an outer metal rotor. The inner rotor, which has one tooth less than the outer rotor, also drives the outer rotor. Gerotors have been used in oil field liquid applications with temperature capabilities up to 300 °C[4]. They have also been used in predominantly gaseous applications in thermal cycles of gas compression engines, where temperatures can exceed 350 °C[5].

A simulation study has also been performed to ascertain gerotors as alternatives to handle gas-liquid multiphase flows[6]. Literature related to physical tests of multiphase gas-liquid behavior of gerotors in oil field applications are not common. A closer comparison can be previous physical test results related to the PCPs with a metallic stator and rotor.

Experimental tests on a three-stage PCP with a metallic stator and rotor was conducted[7] using oil and air as the operating media for pump speeds of 100 to 400 revolutions per minute (rpm), and GVFs from 0% to 80%. They found that for the pure liquid tests (GVF = 0%), the liquid volume flow rate decreased linearly with the increasing differential pressure. A similar trend was cited[8] for PCPs with a metallic stator and rotor, as well as in the catalogue curve for the gerotor pump[4].

Olivet et al. (2002)[7] also observed that the volumetric efficiency increased with an increasing rotational speed for GVF = 0%. In their gas-liquid tests, increasing the GVF increased the volumetric efficiency, for certain differential pressures and rotational speeds. The volumetric efficiency increased with increasing rotational speed, but decreased at 80% GVF.

This work involves the testing of a one-stage, equal-walled prototype gerotor pump using oil and air as the operating fluids. The tests were a first step toward understanding the behavior of the pump under gas-liquid conditions to enable further optimization of the system for eventual field installation. The successful optimization of the gerotor pump and subsequent field installation will create multiphase gas-liquid handling options for field production operations. This will be beneficial to operators as these pumps can serve as alternative or substitute multiphase pumping systems to improve the economic bottom line from the field asset.

Pump Performance Test Terminologies

Some pump terminologies such as displacement, slip, and volumetric efficiency are associated with positive displacement pumps. These are defined here per the rotary pump test standard ANSI/HI (2016)[9].

Displacement (D): The maximum theoretical flow rate that can be delivered by the pump. This may be obtained from either pump geometry or tests. Pump displacement may be expressed as in^3 per revolution.

Slip (S): The amount of fluid that leaks through internal clearances per unit of time. The equation for the slip, expressed in barrels per day (bpd) is:

$$S = \frac{DN}{6.7375} - Q \quad (1)$$

In Eqn. 1, Q is the volume flow rate delivered by the pump (in bpd), and N is the rotational speed of the pump's driving rotor (in rpm). The first term in the equation is the maximum theoretical volume flow rate from the pump (in bpd).

Volumetric Efficiency (η_v): This is the ratio of the volume flow rate delivered by the pump to the maximum theoretical volume flow rate from the pump, expressed as a percentage. This can be calculated from Eqn. 2:

$$\eta_V = \frac{6.7375\,Q}{DN} \times 100\% \quad (2)$$

GVF: This is the ratio of the gas volume flow rate to total volume flow rate at a given pressure and temperature for a given location. This can be calculated from Eqn. 3, in which Q_G and Q_L are the volume flow rates of the gas (air) and liquid (oil), respectively, at the measurement location.

$$GVF = \frac{Q_G}{Q_G + Q_L} \times 100\% \quad (3)$$

Overview of the Gerotor Pump Tested

Figure 1 shows the machined and assembled prototype equal-walled gerotor pump tested in this study. The pump has an intake, pumping, and discharge section,

Fig. 1 *The assembled prototype of the equal-walled gerotor pump showing the main components.*

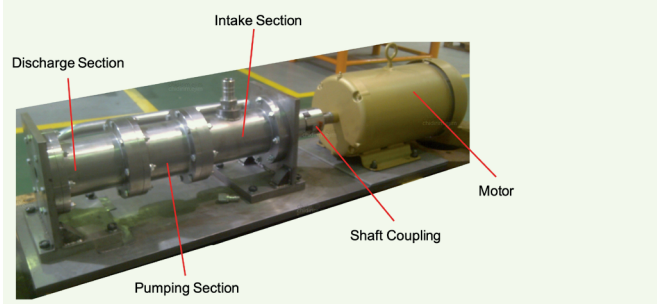

with a motor coupled to the pumping section. The pumping section consists of an inner and outer rotor with six and seven teeth, respectively.

The gerotor is said to be equal walled because the outer rotor has a nearly equal thickness throughout, unlike conventional gerotors. The prime mover, was an electric motor, which provides the mechanical power to rotate the pump shaft and drive the inner rotor, which is keyed to the shaft. The inner rotor, which is enveloped by the outer rotor, drives the outer rotor. The pumping section is designed to fit into a housing with a 4" outside diameter, which is typical of the 400 series pumps in oil field artificial lift applications.

The displacement volume of the pumping section, formed from the cavities between the inner and outer rotors, is 6.41"^{3}. This is equal to a maximum theoretical volume flow rate of approximately 0.95 bpd of fluid per revolution of the cavities. Figure 2 shows the cross-section of the pumping section of the prototype equal-walled gerotor as adopted and described in detail[6].

Test Methodology

The schematic layout of the facility used to test the gerotor pump is shown in Fig. 3, whereas Fig. 4 shows the pump installed on its mounting foundation within its test rig. Mineral oil and air were used as the operating fluids, with the mineral oil fed by gravity from the liquid tank to flood the pump inlet line. In Fig. 3, the gate valve, *G*, just downstream of the pump, was set to a given position and the pump was ramped up to the required rotational speed using the variable frequency drive (VFD), Fig. 4.

In the liquid-only pump test, oil flows through the flow meter, check (or one-way) valve and static mixer into the gerotor pump. The gerotor pumps the fluid against the pressure/resistance posed by the downstream gate valve, and through a return line and back into the liquid tank. The liquid flow rates and the differential pressures across the pump are measured by the liquid flow meter and differential pressure gauge, respectively.

As an alternative, the differential pressure across the pump can also be measured by subtracting the pressure readings of the discharge pressure gauge from those of the intake pressure gauge. A temperature gauge was installed at the inlet to the pump for measuring the pump intake temperature.

In the tests involving gas, pressurized air was supplied by the air compressor, and fed into an air storage tank, or accumulator, to mitigate, or prevent, any fluctuations and provide a steady flow of gas supply. For air delivery, the air outlet pressure is adjusted using the pressure regulating valve, and an air flow meter measures the volume flow rate of air supplied. The air pressure and temperature just downstream of the air volume flow meter were measured by a pressure gauge and temperature gauge, respectively.

The combination of the air volume flow meter, pressure gauge and temperature gauge was used to determine the mass flow rate of air supplied to the system. A check (or one-way) valve was also installed in the air line to prevent any back flow of the operating fluid.

The differential pressure gauge, although used for the liquid tests, was not capable of measuring the differential pressure across the pump during the oil-air tests. For the oil-air tests involving higher rotational speeds, and therefore higher volume flow rates, it was difficult to measure the inlet pressure due to the restricted height

Fig. 2 *A cross-section of the pumping section of the equal-walled gerotor pump[6].*

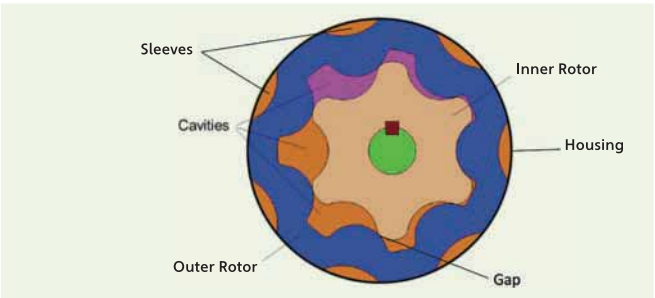

Fig. 3 *A schematic of the test layout.*

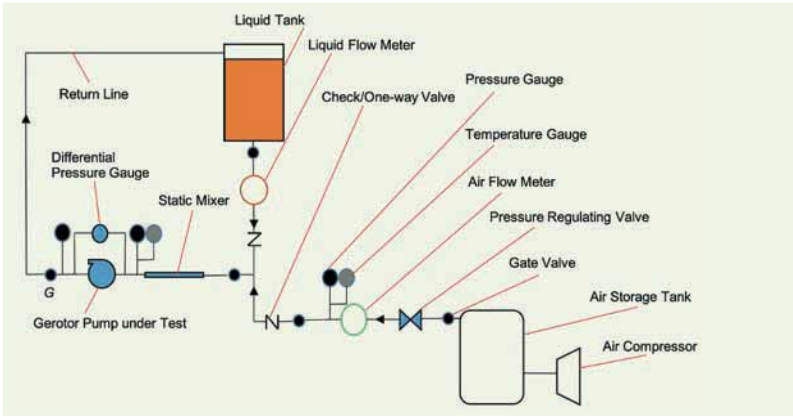

Fig. 4 *The prototype of the gerotor pump installed in the test rig.*

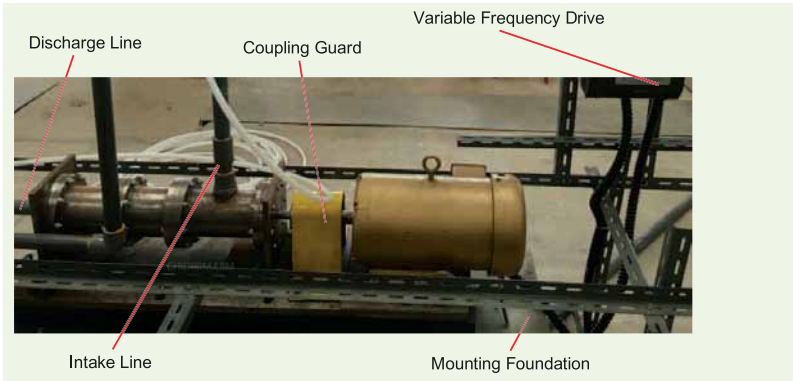

of oil supply in the liquid tank above the pump inlet.

To obtain the pump differential pressures during the oil-air tests, a correlation of mass flow rate as a function of differential pressure and rotational speed was obtained using the liquid test data. For a given rotational speed, and using the total mass flow rate of gas and liquid, measured by the flow meters, the corresponding differential pressures were computed using the correlation previously described. The corresponding pump intake pressures were then computed by subtracting the computed differential pressures from the measured pump discharge pressures.

In running the test for a given operating speed and setting of the gate valve, liquid was first introduced into the system and allowed to circulate for some time. Compressed air was then introduced into the system, which combines with the liquid and flows through the static mixer, where the two fluids are mixed to attain a more homogenized fluid mixture. Based on the instrument readings, the amount of liquid and air were adjusted. Then, based on the pump inlet pressure, the GVF at the pump inlet was computed.

The gas volume flow rate used to calculate the GVF was obtained using the ideal gas equation. The pump inlet GVF was increased until the pump could not deliver any flow at the highest allowable rotational speed of the pump shaft. After flowing through the pump, the oil-air mixture was discharged into the return line and flows back into the liquid tank. The oil is recirculated through the system, whereas the air was vented to the ambient surroundings since the liquid tank was open to the atmosphere.

In both the oil only and oil-air tests, the corresponding voltage, current, and real electrical power input supplied to the VFD were also measured using a power meter/analyzer. The average air and pump inlet temperatures, as well as the average density and absolute viscosity of mineral oil during the test are provided in Table 1. The liquid is considered incompressible and the overall test condition can be considered isothermal based on the relatively large mass flow rate of liquid compared to gas. The list of the test and measurement equipment, as well as the test matrix during this study are presented in Tables 2 and 3, respectively.

Results and Discussion

The test results are divided into two sections, namely oil tests and oil-air tests. The observations are discussed next.

Oil Tests

Flow Rate vs. Differential Pressure

Figure 5 presents the variation of the oil volume flow rate with the differential pressure across the one-stage gerotor pump. For each rotational speed, the liquid flow rate decreases linearly as the differential pressure across the pump increases. This trend is typical of positive displacement pumps[4, 6-8]. For this gerotor design, and at a rotational speed of 200 rpm, the liquid flow rate decreased from 120 bpd to 56 bpd when differential pressures were 2.5 psi and 4 psi, respectively.

As the rotational speed increased up to the maximum test speed of 350 rpm, the same linear relationship between the liquid volume flow rate and the differential pressure was maintained. At 350 rpm, the flow rate

Table 1 *The average fluid properties during the tests.*

Average Air Temperature	Average Oil and Air Temperature at Pump Inlet	Oil Density	Oil Absolute (or Dynamic) Viscosity
22 °C (71 °F)	22 °C (71 °F)	829.1 kg/m^3	6.73 cP

Table 2 *A list of the test and measurement equipment used.*

Equipment	Capacity
Oil Flow Meter	2 – 150 U.S. gallon per minute
Air Flow Meter	4 – 60 actual ft^3 per minute
Compressor (Screw Type)	8.5 Bar
Differential Pressure Gauge	0 – 1,000" H_2O
Pressure Gauge	0 – 50 psig
Temperature Gauge	0 – 100 °C
Power Meter/Analyzer	1 - 600 Vrms; 0.1 – 6,000 Arms

Table 3 The test matrix for the gerotor pump performance measurements.

Discharge Valve Setting	Pump Shaft Rotational Speed (rpm)	Pump Inlet, GVF (%)
Position 1 (~8% Open)	200	0, 10, 15
	250	
	300	
	350	
Position 2 (~17% Open)	200	0, 10, 15
	250	
	300	
	350	
Position 3 (~26% Open)	200	0, 10, 15
	250	
	300	
	350	
Position 4 (~33% Open)	200	0, 10, 15
	250	
	300	
	350	

is 245 bpd at 6 psi differential pressure, and 140 bpd at 10 psi differential pressure. The pump is therefore able to deliver more flow against a higher differential pressure when the rotational speed is increased.

Further analysis of the plots shows that each slope is less steep as the rotational speed increases. This implies higher pump rotational speeds increase the magnitude of flow per unit increase in differential pressure.

Slip vs. Differential Pressure

Figure 6 shows the variation of the slip with differential pressure. For a given rotational speed, the magnitude of the slip increases with increasing differential pressure. This increase in loss of volume flow rate through the pump clearances with increasing differential pressure implies a lower amount of liquid is delivered by the pump as differential pressure increases. This is in line with the trend of the flow rates discussed previously for Fig. 5.

As the rotational speed increases to 350 rpm, the slip increases with a corresponding increase in the differential pressure. A closer observation in the variation of the slip is that the slope of each line decreases as the rotational speed increases from 200 rpm to 350 rpm. This suggests that as the pump speed increases, the amount of fluid leakage through the pump clearances decreases per unit increase in differential pressure. Again, this is in line with the increase in volume flow rate per unit rise in differential pressure highlighted earlier for Fig. 5.

Volumetric Efficiency vs. Differential Pressure

Figure 7 shows the variation in volumetric efficiency, η_V, with pump differential pressure. For the 200 rpm plot, η_V decreases from approximately 63% to approximately 30% with increasing differential pressure. The decrease in the η_V, with differential pressure, is in line with the discussions presented earlier, where a reduced amount of oil is delivered by the pump as the differential pressure increases, for a given rotational speed.

As the rotational speed increases to 350 rpm, the η_V decreases from 73% to 42% with increasing differential pressure. Similar to the trend for the slip in Fig. 6, the reduction in η_V with increasing differential pressure decreases as the rotational speed is increased.

Electric Power Input vs. Differential Pressure

Figure 8 shows the variation of the electric power input to the VFD, with pump differential pressure. For each rotational speed, the common trend is that the input power decreases with decreasing differential pressure. Given that for a specific rotational speed, the flow rate increases with the decreasing differential pressure, as previously shown in Fig. 5, it implies from Fig. 8 that the reduction in electric power input occurs as the volume flow rate increases.

Comparing across rotational speeds, the 200 rpm

Fig. 5 The variation of the liquid flow rate with differential pressure.

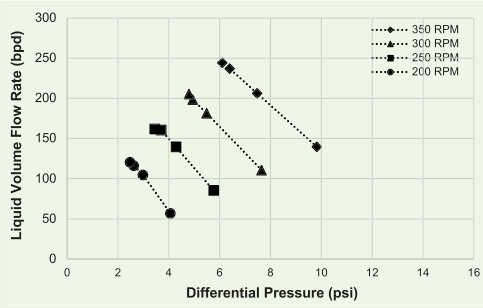

Fig. 6 The variation of the slip with differential pressure.

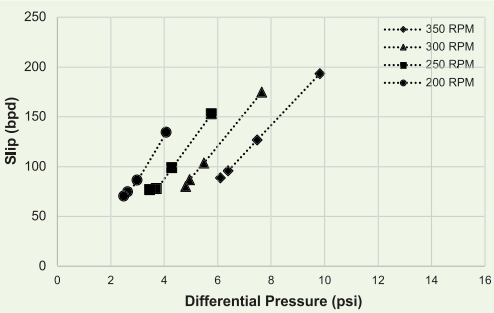

Fig. 7 *The variation of the liquid volumetric efficiency with differential pressure.*

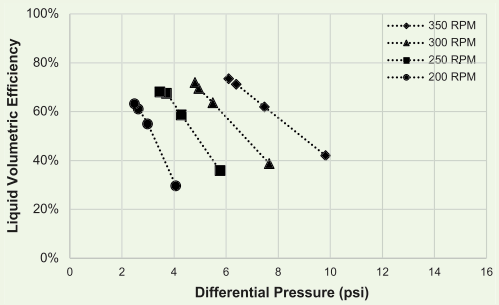

Fig. 8 *The variation of electric power input to VFD with differential pressure.*

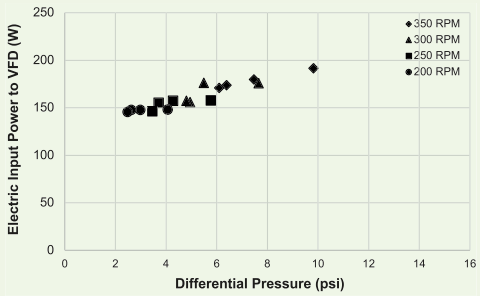

data shows that average input power is approximately 147 watts (W). As the rotational speed increases toward 350 rpm, the input power increases gradually to an average value of approximately 179 W, an increase of approximately 22%. The increase in input power implies an increase in energy demand by the system needed to perform a greater amount of work on the fluid as the rotational speed increases.

Scaling Relationships in Oil Tests

One of the benefits of testing pump prototypes is the capability of obtaining performance information and establishing some similarity relationships to determine pump performance at other operating conditions. Similarity rules are well documented in open literature, e.g., in centrifugal pumps[10]. Given the variation of the parameters in Figs. 5, 6, and 7, the data were scaled to obtain a universal relationship for each pump parameter.

Figures 9, 10, and 11 show the scaled plots for liquid flow rate, slip, and liquid volumetric efficiency, respectively, with scaled differential pressure. The liquid flow rate and the slip is scaled with the rotational speed, whereas the differential pressure is scaled with the square of the rotational speed. Each plot shows that through this scaling, the data points in each plot all collapse or overlap one another. Table 4 is a summary of the parameters for the regression fit line for each of the plots, as well as the scaled differential pressure.

From Table 4, assuming dynamic similarity, one can estimate the potential pump flow rate, slip, and liquid volumetric efficiency at a given field scale differential pressure and rotational speed. For instance, typical operating speeds of some downhole pumps can be up to 3,500 rpm. Differential pressure can vary depending on the back pressure at a given well site.

For a pump differential pressure of 600 psi, the corresponding liquid volume flow rate, slip, and liquid volumetric efficiency for this design of the one-stage gerotor pump is estimated as 2,488 bpd, 842 bpd, and 75%, respectively. The capability of using the scaling plot from the prototype pump oil tests to estimate field

Fig. 9 *The scaling plot between the liquid volume flow rate and differential pressure.*

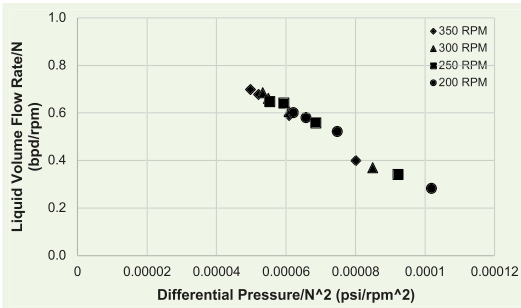

Fig. 10 *The scaling plot between the liquid slip and differential pressure.*

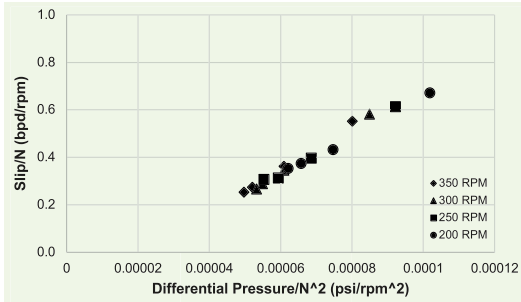

Fig. 11 *The scaling plot between the liquid volumetric efficiency and differential pressure.*

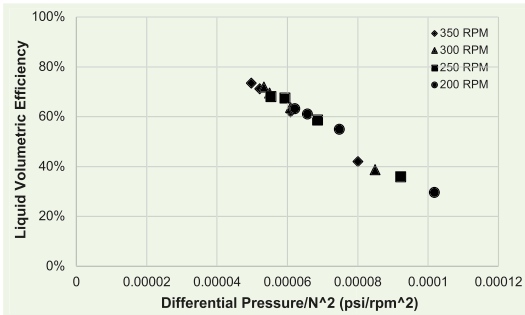

Table 4 *A summary of the regression results from the scaled plots.*

	Y-Intercept	Slope	R^2 Value
Scaled Liquid Flow Rate, Q_L/N (bpd/rpm)	1.1297	-8,554.3	0.9772
Scaled Liquid Slip, S_L/N (bpd/rpm)	-0.1784	8,554.3	0.9772
Liquid Volumetric Efficiency, η_V, (%)	118.75	-899,130	0.9772

operation parameters will aid in the optimization of the current pump design to reduce the amount of slip, and therefore, increase the pump throughput and liquid volumetric efficiency.

Oil-Air Tests

The results discussed next are for each rotational speed studied during the test using mineral oil and air. The plots show a variation of the total fluid volume flow rate, total slip (maximum theoretical volume flow rate less flow rate of gas and liquid), total volumetric efficiency and total electric input power to the VFD with differential pressure at GVFs of 0%, 10%, and 15%, respctively. For the test at 200 rpm, only one reading for the test point at 10% GVF and an almost closed valve setting could be obtained. The pump could not support the flow for the remaining tests at a rotational speed of 200 rpm at 10% and 15% GVF.

Total Volume Flow Rate vs. Differential Pressure

Figures 12, 13, and 14 present the variation of the total volume flow rate with a differential pressure at 250 rpm, 300 rpm, and 350 rpm, respectively. For all speeds and GVF > 0%, the general trend in the plots is a decrease in total flow rate with increasing differential pressure, which is similar to the trend observed for the oil only (single-phase) tests. Furthermore, for GVF > 0% and at a specific differential pressure, the total volume flow rate increases with the increasing rotational speed, similar to observations in the oil only (single-phase) tests. For each rotational speed, and comparing results at a given differential pressure, the total volume flow rate increases with the increasing GVF for the range

Fig. 12 *The total volume flow rate vs. differential pressure at 250 rpm (GVF: 0%, 10%, and 15%).*

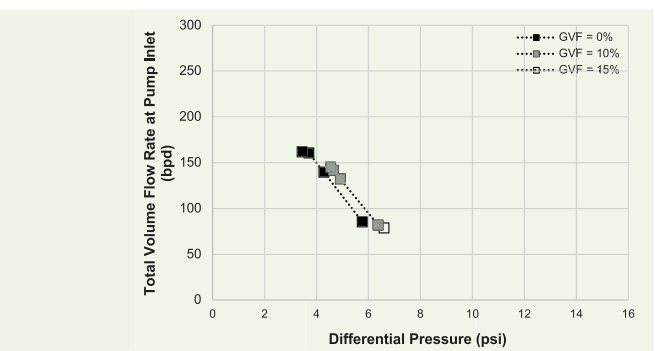

Fig. 13 *The total volume flow rate vs. differential pressure at 300 rpm (GVF: 0%, 10%, and 15%).*

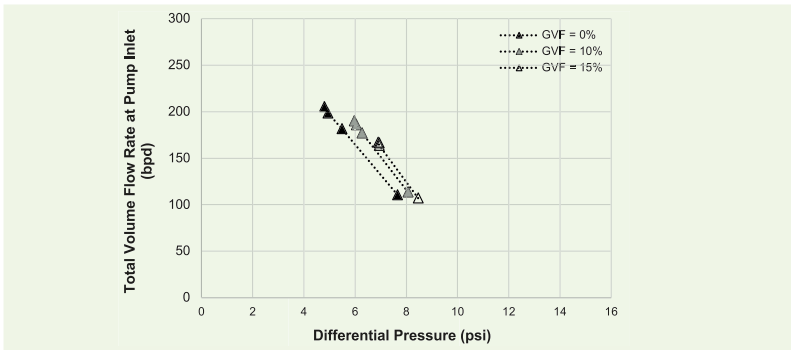

Fig. 14 *The total volume flow rate vs. differential pressure at 350 rpm (GVF: 0%, 10%, and 15%).*

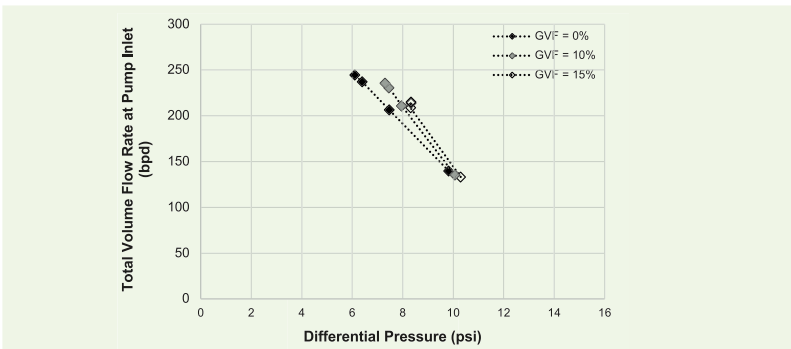

Fig. 15 *The liquid volume flow rate vs. differential pressure at 300 rpm (GVF: 0%, 10%, and 15%).*

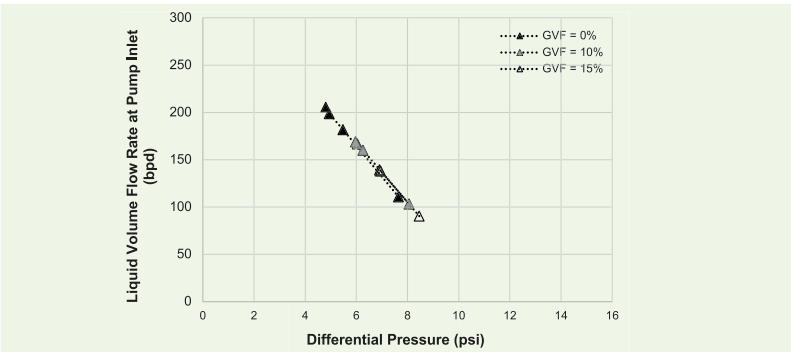

of differential pressures during the test.

This trend was more evident with increasing rotational speeds and also shows that at 350 rpm, the plots for GVF > 0 will tend to fall below that of GVF = 0 beyond a differential pressure of 10 psi. Higher total volume flow rates with increasing GVF over certain ranges of differential pressures have been observed for metal-to-metal PCPs[7, 8]. Such trends persisted for higher rotational speeds and GVFs up to 50%, and was not evident for lower rotational speeds.

In Ejim et al. (2020)[6], a linear decrease in the liquid volume flow rate with differential pressure was observed for the different GVFs studied at a rotational speed of 300 rpm. A similar trend was also observed in this test, Fig. 15. For a given valve setting, the volume flow rate of liquid decreased with an increasing GVF. This is consistent with the flow physics, whereby as the gas occupies more volume in the flow, the volume flow rate of the liquid decreases.

Total Slip vs. Differential Pressure

The variation of total slip with differential pressure is shown in Figs. 16, 17, and 18. The trend in the figures is opposite those observed for the total volume flow rates previously discussed. The figures show that for all the GVFs, the total slip increases with an increasing differential pressure. For the same differential pressure, the total slip decreases with an increasing GVF. In addition, increasing the speed reduces the magnitude of the total slip.

Total Fluid Volumetric Efficiency vs. Differential Pressure

The change in total fluid volumetric efficiency with increasing differential pressure is presented in Figs. 19, 20, and 21. Similar to the plots for the total volume flow rate, the general trend in the plots is a decrease in total volumetric efficiency with an increasing differential pressure. In addition at a given differential pressure, the total fluid volumetric efficiency increases with an increasing rotational speed. At each rotational speed and a given differential pressure, the total volumetric efficiency increases with an increasing GVF for the differential pressures tested. For instance, at 300 rpm and a differential pressure of 7 psi, the total volumetric efficiency varies from approximately 47% at GVF = 0% to approximately 57% at GVF = 15%. The increase in total volumetric efficiency with an increasing GVF over certain ranges of differential pressures has also been observed[7, 8].

For GVF > 0, comparing the liquid volumetric efficiency variation with differential pressure (at 300 rpm) with those obtained[6], also at 300 rpm, a similar negatively sloping trend was observed, Fig. 22. For a fixed valve setting, the liquid volumetric efficiency decreases with an increasing GVF. This is consistent with a decrease in the liquid volume flow rate with an increasing GVF as observed and highlighted in Fig. 15.

Total Power Input vs. Differential Pressure

Figures 23, 24, and 25 show the variation of the electric power input to the VFD, with pump differential pressure. For each rotational speed and GVF > 0%, overall, the input power decreases with a decreasing differential pressure, similar to the oil tests. For a given rotational speed and given differential pressure, the input power decreases with an increasing GVF. For example, at 300 rpm, and approximately 7 psi differential pressure, the input power is approximately 176 W for GVF = 0%, and decreases to approximately 158 W as the GVF increases to 15%.

The lower input power with an increasing GVF implies a decrease in energy requirement of the pumping operation as more gas is introduced into the system.

Fig. 16 *The total slip vs. differential pressure at 250 rpm (GVF: 0%, 10%, and 15%).*

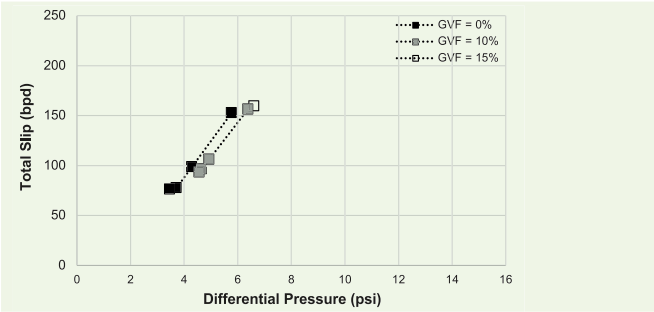

Fig. 17 *The total slip vs. differential pressure at 300 rpm (GVF: 0%, 10%, and 15%).*

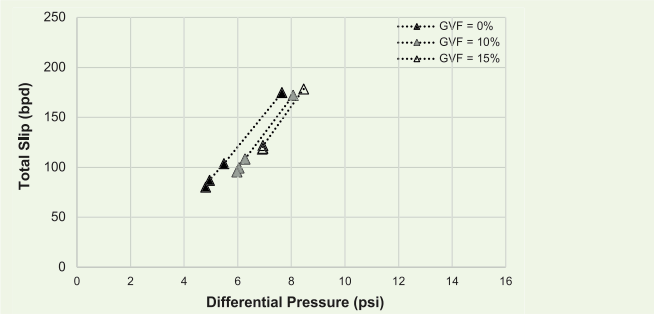

Fig. 18 *The total slip vs. differential pressure at 350 rpm (GVF: 0%, 10%, and 15%).*

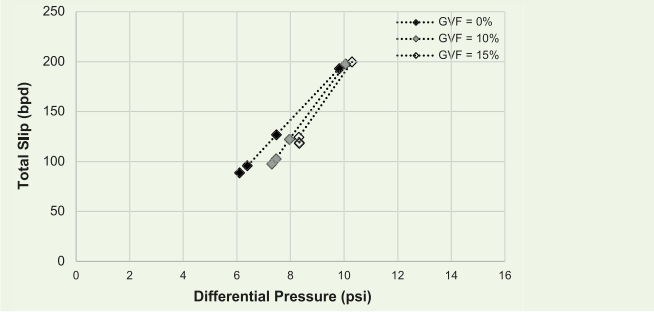

Fig. 19 *The total fluid volumetric efficiency vs. differential pressure at 250 rpm (GVF: 0%, 10%, and 15%).*

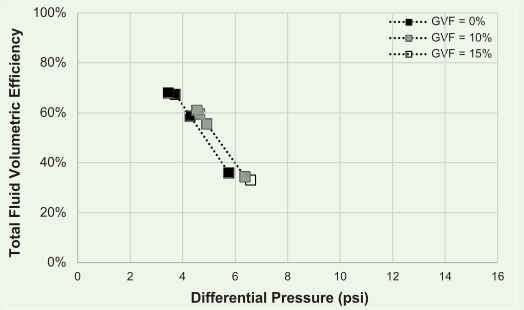

Fig. 20 *The total fluid volumetric efficiency vs. differential pressure at 300 rpm (GVF: 0%, 10%, and 15%).*

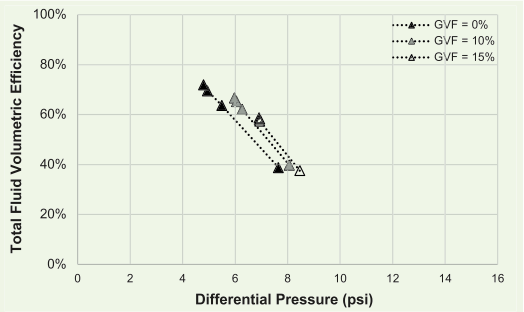

Fig. 21 *The total fluid volumetric efficiency vs. differential pressure at 350 rpm (GVF: 0%, 10%, and 15%).*

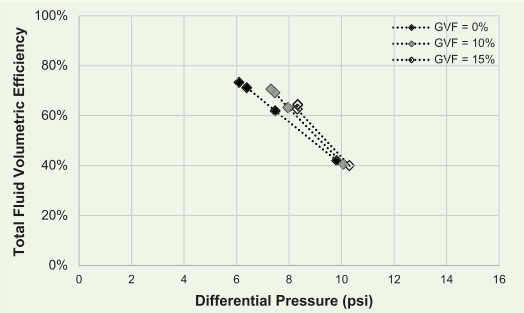

Increasing the rotational speed for each GVF condition shows that the electric power input to the VFD also increases. For the GVF = 15% and approximately 7 psi, the input power varies from approximately 156 W at 250 rpm to approximately 175 W at 350 rpm. Similar to the oil tests, the increase in input power implies higher energy demand by the system to work on the fluid as the rotational speed increases.

Conclusions

This study was about the physical testing of a prototype equal-walled gerotor pump to ascertain its performance characteristics when pumping oil (GVF = 0%) and oil-gas mixtures (GVF = 10% and 15%).

The performance parameters presented were volume flow rate delivery, slip, and volumetric efficiency at rotational speeds of 200 rpm, 250 rpm, 300 rpm, and 350 rpm. The capability of the pump to follow scaling relationships based on some of the operating conditions was also investigated. These tests were part of the process toward determining the physical performance of the pump to ascertain areas of improvement

Fig. 22 *The liquid volumetric efficiency vs. differential pressure at 300 rpm (GVF: 0%, 10%, and 15%).*

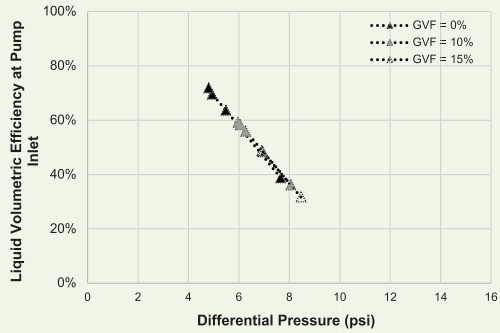

Fig. 23 *The total power input vs. differential pressure at 250 rpm (GVF: 0%, 10%, and 15%).*

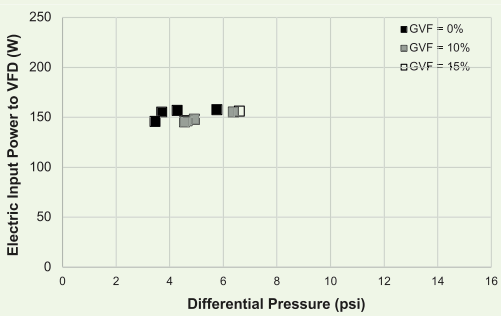

Fig. 24 *The total power input vs. differential pressure at 300 rpm (GVF: 0%, 10%, and 15%).*

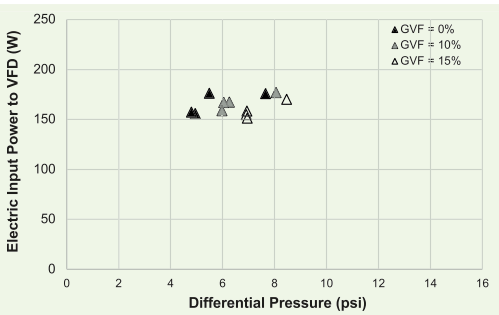

Fig. 25 *The total power input vs. differential pressure at 350 rpm (GVF: 0%, 10%, and 15%).*

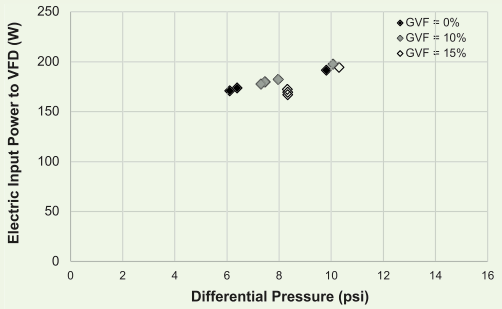

before ultimately a field prototype is designed and manufactured.

Results from the oil tests showed that the volume flow rate and differential pressure had a negatively sloping linear relationship. For GVF > 0, the total volume flow rate increased with an increasing GVF, for certain differential pressures. The total volume flow rate increased with an increasing rotational speed for all GVFs. This trend was also observed for the volumetric efficiencies, and the inverse was the case for the variation of the total slip with an increasing differential pressure. The total electrical input power to the VFD increased with an increasing rotational speed for all GVFs. For a given GVF and differential pressure, the input power decreased with the increasing GVF. This was consistent with a reduction in the energy required by the pumping operation as additional gas enters the system.

Pump performance scaling was observed from the oil tests. The volume flow rate and slip scaled with the rotational speed, whereas the differential pressure scaled with the square of the rotational speed. The data points in the corresponding scaling plots overlapped one another. This indicates that a single universal plot can be used to estimate the pump performance at a higher rotational speed at a given flow rate or volumetric efficiency and differential pressure.

Overall, the performance trend of the prototype equal-walled gerotor pump is similar to those in the cited references. From the results and observations during the test, there are different components of the pump with room for optimization. The plan going forward is to incorporate the optimized features in the next generation of the gerotor pump.

Acknowledgments

This article was prepared for presentation at the Abu Dhabi International Petroleum Exhibition and Conference, Abu Dhabi, UAE, November 9-12, 2020.

Nomenclature

D = displacement, L^3/rev, $inch^3$ per revolution

N = rotational speed of the pump shaft, t^{-1}, rpm

Q = volume flow rate, L^3/t, bpd

S = slip, L^3/t, bpd

η = efficiency, %

Subscripts

G = gas phase

L = liquid phase

V = volumetric

References

1. Hua, G., Falcone, G., Teodoriu, C. and Morrison, G.L.: "Comparison of Multiphase Pumping Technologies for Subsea and Downhole Applications," *Oil and Gas Facilities*, Vol. 1, Issue 1, February 2012, pp. 36-46.

2. Moon, T.: "The Defining Series: Progressing Cavity Pumps (PCPs)," *Oilfield Review*, 2016.

3. Arredondo, M., Caballero, D., Morety, R., Delgado, A., et al.: "All Metal PCP Experiences in Orinoco Belt," SPE paper 171370, presented at the SPE Artificial Lift Conference and Exhibition — North America, Houston, Texas, October 6-8, 2014.

4. REAM-RTI, LLC: "Advanced Pumping Equipment to Fit New Reality," *Oil and Gas Eurasia*, Vol. 6, 2015, pp. 70-71.

5. Holtzapple, M.: "StarRotor Engine for Military Applications," *Journal of Defense Management*, Vol. 6, Issue 1, 2016.

6. Ejim, C.E., Oshinowo, L. and Xiao, J.: "Modeling Gerotor Pump Performance in Artificial Lift for Single-Phase and Multiphase Conditions," *SPE Production & Operations*, Vol. 35, Issue 2, May 2020, pp. 393-405.

7. Olivet, A., Gamboa, J. and Kenyery, F.: "Experimental Study of Two-Phase Pumping in a Progressive Cavity Pump Metal to Metal," SPE paper 77730, presented at the SPE Annual Technical Conference and Exhibition, San Antonio, Texas, September 29-October 2, 2002.

8. Gamboa, J., Aurelio, O. and Sorelys, E.: "New Approach for Modeling Progressive Cavity Pumps Performance," SPE paper 84137, presented at the SPE Annual Technical Conference and Exhibition, Denver, Colorado, October 5-8, 2003.

9. American National Standard: "Rotary Pump Tests," ANSI/HI 3.6-2016, Hydraulic Institute, New Jersey, 2016, 39 p.

10. Timar, P.: "Dimensionless Characteristics of Centrifugal Pump," *Chemical Papers*, Vol. 59, Issue 6b, 2005, pp. 500-503.

About the Authors

Dr. Chidirim E. Ejim

Ph.D. in Mechanical Engineering, University of Alberta

Dr. Chidirim E. Ejim is a Petroleum Engineer working in the artificial lift focus area within the Production Technology Team of Saudi Aramco's Exploration and Petroleum Engineering Center – Advanced Research Center (EXPEC ARC). Prior to joining Saudi Aramco in 2014, Chidirim spent over 7 years with Schlumberger's Artificial Lift Segment, working on surface horizontal pumping systems; downhole pump design, development and testing; multiphase production systems; as well as downhole gas separator/gas handler testing and analysis.

He received his B.Eng. degree (Honors) from the University of Malta, Msida, Malta; his M.S. degree from the University of Waterloo, Ontario, Canada; and his Ph.D. degree from the University of Alberta, Edmonton, Canada, all in Mechanical Engineering.

Dr. Jinjiang Xiao

Ph.D. in Petroleum Engineering, University of Tulsa

Dr. Jinjiang Xiao is a Senior Petroleum Engineering Consultant working in Saudi Aramco's Exploration and Petroleum Engineering Center – Advanced Research Center (EXPEC ARC). His current focus is artificial lift research and development.

Prior to joining Saudi Aramco in 2003, Jinjiang spent 10 years with Amoco and later BP-Amoco, working on multiphase flow, flow assurance and deep-water production engineering.

He received both his M.S. and Ph.D. degrees in Petroleum Engineering from the University of Tulsa, Tulsa, OK.

Dr. Olanrewaju M. Oshinowo

Ph.D. in Chemical Engineering and Applied Chemistry, University of Toronto

Dr. Olanrewaju M. "Lanre" Oshinowo is a Science Specialist working in Saudi Aramco's Research & Development Center, where he focuses on competitive technology development to improve the design and operation of oil and gas process facilities.

Lanre joined Saudi Aramco in 2012, and has over 25 years of experience in the application of computational fluid dynamics, process modeling and simulation in the oil and gas and process industries in research, development, project engineering, and operations.

He previously held leading technical roles at ConocoPhillips, HATCH, ANSYS, and Fluent in the U.S. and Canada. Lanre is the author of more than 75 journal and conference publications, and with multiple inventions to his credit.

Lanre is a member of the Society of Petroleum Engineers (SPE) and the American Institute of Chemical Engineers, and is a licensed professional engineer in the province of Ontario, Canada.

In 1997, he received his Ph.D. degree in Chemical Engineering and Applied Chemistry from the University of Toronto, Toronto, Ontario, Canada.

Have an article you would like to publish? Here are our guidelines.

These guidelines are designed to simplify and help standardize submissions. They need not be followed rigorously. If you have any questions, please call us.

Length

Average of 2,500-4,000 words, plus illustrations/photos and captions. Maximum length should be 5,000 words. Articles in excess will be shortened.

What to send

Send text in Microsoft Word format via email. Illustrations/photos should be clear and sharp. Editable files are requested for graphs, i.e., editable in Excel.

Procedure

Notification of acceptance is usually within three weeks after the submission deadline. The article will be edited for style and clarity and returned to the author for review. All articles are subject to the company's normal review. No paper can be published without a signature at the manager level or above.

Format

No single article need include all of the following parts. The type of article and subject covered will determine which parts to include.

Working Title
Lorem Ipsum here.

Abstract
Usually 150-300 words to summarize the main points.

Introduction
Different from the abstract in that it sets the stage for the content of the article, rather than telling the reader what it is about.

Main body
May incorporate subtitles, artwork, photos, etc.

Conclusion/Summary
Assessment of results or restatement of points in introduction.

Endnotes/References/Bibliography
Use only when essential. Use author/date citation method in the main body. Numbered footnotes or endnotes will be converted. Include complete publication information. Standard is *The Associated Press Stylebook*, 52nd ed. and *Wesbter's New World College Dictionary*, 5th ed.

Acknowledgments
Use to thank those who helped make the article possible.

Illustration/Tables/Photos and explanatory text

If the files are large, these can be submitted separately, due to email size limits. Initial submission may include copies of originals; however, publication will require the originals. When possible, submit original images. Color is preferable.

File Format

Illustration files with .EPS extensions work best. Other acceptable extensions are .TIFF/.JPEG/.PICT.

Permission(s) to reprint, if appropriate

Previously published articles are acceptable but can be published only with written permission from the copyright holder.

Author(s)/Contibutor(s)

Please include a brief biographical statement.

Submission/Acceptance Procedures

Papers are submitted on a competitive basis and are evaluated by an editorial review board comprised of various department managers and subject matter experts. Following initial selection, authors whose papers have been accepted for publication will be notified by email.

Papers submitted for a particular issue but not accepted for that issue may be carried forward as submissions for subsequent issues, unless the author specifically requests in writing that there be no further consideration.

Submit articles to:

Editor
The Saudi Aramco Journal of Technology
C-3D, Room AN-1080
North Admin Building #175
Dhahran 31311, Saudi Arabia
Tel: +966-013-876-0498
Email: *william.bradshaw.1@aramco.com.sa*

Submission deadlines

Issue	Paper submission deadline	Release date
Fall 2021	May 11, 2021	September 30, 2021
Winter 2021	August 12, 2021	December 31, 2021
Spring 2022	November 15, 2021	March 31, 2022
Summer 2022	February 8, 2022	June 30, 2022

There is more.

Modeling Hydraulic Response of Rock Fractures under Effective Normal Stress

Xupeng He, Marwa M. AlSinan, Dr. Hyung T. Kwak and Dr. Hussein Hoteit

Abstract / The permeability of rock fractures and its variation with effective stress is of considerable interest in broad energy and environmental applications, such as enhanced oil and gas from hydrocarbon reservoirs, geothermal energy extraction, and geological carbon storage, among others. The permeability of a rock fracture is a complex function of various static parameters, including mechanical aperture, surface roughness, and fracture contact areas, all of which are the function of effective stress acting on the fracture walls.

Advanced Resistivity Modeling to Enhance Vertical and Horizontal Well Formation Evaluation

Mohamed S. Mahiout, Dr. Chengbing Liu, Ralf Polinski and Moshood Kassim

Abstract / Accurate formation evaluation relies on, among other inputs, the correct true formation resistivity (Rt). The common practice in the industry is to use the deep resistivity log as Rt. A single resistivity curve from a deep resistivity measurement often does not represent Rt, due to the shoulder bed effect, polarization at the boundaries, and many other effects. This is especially true in high angle and horizontal wells.

An Acoustic-Based Method for Measuring Surfactant Concentration in Field Applications

Hala A. AlSadeg, Jesus M. Felix Servin and Dr. Amr I. Abdel-Fattah

Abstract / Numerous enhanced oil recovery (EOR) techniques entail injecting chemical treatments such as surfactants at a predetermined concentration to achieve targeted results. Typically, these formulations are prepared on-site using large mixing tanks, prior to injection into the reservoir. The current quality assurance practice for proper concentration of treatment materials uses indirect methods such as interfacial tension (IFT) and/or viscosity measurements. These measurements can be lengthy or only suitable for a specific range of dispersed phase volumes.

Development of Oriented Fracturing of Chemically Induced Pressure Pulse for Unconventional Gas Reservoirs

Ayman R. Al-Nakhli

Abstract / Commercial production from unconventional reservoirs require new technologies to reduce the breakeven cost. Multistage fracturing was an enabler of gas production from such reservoirs; however, it is responsible for significant cost. Fracturing jobs cancelation, due to high pressure, results in nonproductive wells, which also represent high cost. Unfractured wells results in locked and unproduced potential gas.

أرامكو السعودية
saudi aramco

Aramco
Journal
of Technology

Liked this issue? Sign up. It's free.

To begin receiving the *Aramco Journal of Technology* please complete this form, scan and send by email to ***william.bradshaw.1@aramco.com.***

Got questions?

Just give us a call at +966-013-876-0498 and we'll be happy to help!

Scan the QR code to go straight to your email and attach the form!

Subscription Form

Name
Title
Organization
Address
City
State/Province
Postal code
Country
Email address
Phone number
Number of copies

www.saudiaramco.com/jot